LANDSLIDES AND LANDSCAPE EVOLUTION OVER DECADES TO MILLENNIA—USING TEPHROCHRONOLOGY, AIR PHOTOS, LIDAR, AND GEOPHYSICAL INVESTIGATIONS TO RECONSTRUCT PAST LANDSCAPES

by

CORINA R. CEROVSKI-DARRIAU

A DISSERTATION

Presented to the Department of Geological Sciences
and the Graduate School of the University of Oregon
in partial fulfillment of the requirements
for the degree of
Doctor of Philosophy

March 2016

DISSERTATION APPROVAL PAGE

Student: Corina R. Cerovski-Darriau

Title: Landslides and Landscape Evolution over Decades to Millennia—Using Tephrochronology, Air Photos, Lidar, and Geophysical Investigations to Reconstruct Past Landscapes

This dissertation has been accepted and approved in partial fulfillment of the requirements for the Doctor of Philosophy degree in the Department of Geological Sciences by:

Joshua J. Roering	Chairperson
Ray J. Weldon II	Core Member
Douglas R. Toomey	Core Member
Mark A. Fonstad	Institutional Representative

and

Scott L. Pratt	Dean of the Graduate School

Original approval signatures are on file with the University of Oregon Graduate School.

Degree awarded March 2016

DISSERTATION ABSTRACT

Corina R. Cerovski-Darriau

Doctor of Philosophy

Department of Geological Science

March 2016

Title: Landslides and Landscape Evolution over Decades to Millennia—Using Tephrochronology, Air Photos, Lidar, and Geophysical Investigations to Reconstruct Past Landscapes

Landscapes respond to external perturbations over a variety of timescales, including million-year tectonic forcing, millennial to decadal climate fluctuations, and minutes-long high intensity storms or large magnitude earthquakes. In mountainous regions, understanding the role of landslides in driving the hillslope response to these perturbations is paramount for understanding landscape evolution over geologic timescales and hazards over human timescales. Here I analyze the landslide-driven hillslope response over millennial to decadal timescales using a variety of tools and techniques (e.g. tephrochronology, lidar and air photo analysis, field and subsurface investigations, and seismic refraction) in the Waipaoa Basin (New Zealand) and Oregon Coast Range (USA). For the Waipaoa study catchment, pervasive landslides have been sculpting >99% of the hillslopes in response to >50 m of fluvial incision following the shift to a warmer, wetter climate after the Last Glacial Maximum (LGM) (~18 ka). Then, starting in the late 1800s, European settlement resulted in deforestation and conversion of >90% of the landscape to pastureland—spurring a rapid increase in landslide-driven erosion. To quantify the landscape response, I first reconstruct LGM and younger paleosurfaces using tephrochronology and lidar-derived surface roughness to estimate the

volume, timing, and distribution of hillslope destabilization. From these reconstructions, I calculate the post-LGM catchment-averaged erosion rate (1.6 mm/yr) and determine that the timing of the initial hillslope adjustment was rapid and occurred by ~10 ka. Second, I quantify the rate and volume of historic hillslope degradation using a 1956-2010 sequence of aerial photographs, lidar, and field reconnaissance to map the spatial extent of active landslides, create a 'turf index' based on the extent and style of pastoral ground disruption, correlate that with downslope velocity, and calculate the average annual sediment flux. From the sediment flux, I calculate an erosion rate over the past ~50 years (~20 mm/yr) that is 10x greater than post-LGM. Lastly, in Western Oregon, I confirm that seismic refraction can determine the size (e.g. depth) and failure style of landslides in western Oregon—data needed to incorporate these poorly studied landslides into future landscape evolution or hazard models.

This dissertation includes both previously published and unpublished co-authored material.

CURRICULUM VITAE

NAME OF AUTHOR: Corina R. Cerovski-Darriau

GRADUATE AND UNDERGRADUATE SCHOOLS ATTENDED:

University of Oregon, Eugene
University of California, Berkeley

DEGREES AWARDED:

Doctor of Philosophy, Geological Science, 2016, University of Oregon
Bachelor of Arts, Geology, 2008, University of California, Berkeley

AREAS OF SPECIAL INTEREST:

Hillslope Geomorphology: Landscape Evolution, Landslide Hazards, Coseismic Landslides

PROFESSIONAL EXPERIENCE:

Graduate Teaching & Research Fellow, Department of Geological Sciences, University of Oregon, 2010-2015

Policy Associate, Government Affairs Program, American Geosciences Institute, 2009- 2010

GRANTS, AWARDS, AND HONORS:

Shlemon Scholarship in Engineering Geology, Geological Society of America, 2015

Graduate Student Research Grant, Geological Society of America, 2015

Outstanding Graduate Teaching Fellow Award, Department of Geological Sciences, University of Oregon, 2015

Thayer Scholarship, Department of Geological Sciences, University of Oregon, 2010, 2013, 2014

U.S. Student Representative, International Year of the Planet Earth, UNESCO, 2008

PUBLICATIONS:

Cerovski-Darriau, C. and J. J. Roering (under review), Influence of Anthropogenic Land-Use Change on Hillslope Erosion in the Waipaoa River Basin, New Zealand, Earth Surface Processes and Landforms.

Kuehl, S. A., C. R. Alexander, N. E. Blair, C. K. Harris, K. M. Marsaglia, A. S. Ogston, A. R. Orpin, J. J. Roering, A. J. Bever, E. L. Bilderback, L. Carter, **C. Cerovski-Darriau**, L. B. Childress, D. R. Corbett, R. P. Hale, E. L. Leithold, N. Litchfield, J. M. Moriarty, M. J. Page, L. E. R. Pierce, P. Upton, and J. P. Walsh (2015), A source to sink perspective of the waipaoa river margin, Earth-Science Rev., doi:10.1016/j.earscirev.2015.10.001.

Roering, J. J., B. H. Mackey, A. L. Handwerger, A. M. Booth, D. A. Schmidt, G. L. Bennett, and **C. Cerovski-Darriau** (2015), Beyond the angle of repose: A review and synthesis of landslide processes in response to rapid uplift, Eel River, Northern California, Geomorphology, 236, 109–131, doi:10.1016/j.geomorph.2015.02.013.

Cerovski-Darriau, C., J. J. Roering, M. Marden, A. S. Palmer, and E. L. Bilderback (2014), Quantifying temporal variations in landslide-driven sediment production by reconstructing paleolandscapes using tephrochronology and lidar: Waipaoa River, New Zealand, Geochemistry, Geophys. Geosystems, 15(11), 4117–4136, doi:10.1002/2014GC005467.

Roering, J. J., B. H. Mackey, J. A. Marshall, K. E. Sweeney, N. I. Deligne, A. M. Booth, A. L. Handwerger, and **C. Cerovski-Darriau** (2013), "You are HERE": Connecting the dots with airborne lidar for geomorphic fieldwork, Geomorphology, 200, 172–183, doi:10.1016/j.geomorph.2013.04.009.

ACKNOWLEDGMENTS

I am thankful for the many mentors, friends, and family members who have supported me through this endeavor. In particular, I would like to thank Joshua Roering for being a tremendous advisor who inspired me with his insightful questions, kind encouragement, and high standards to be a better researcher and scholar. I would also like to thank the rest of my dissertation committee—Ray Weldon, Doug Toomey, and Mark Fonstad—for their guidance and support throughout my PhD. I am also incredibly grateful to all the people at the University of Oregon who I have had the pleasure of interacting with over the years, in particular: my office mates and co-conspirators Alex Handwerger and Rob Skarbek, my lab cohort and cribbage opponent Kristin Sweeney, my labmates Jill Marshall, Georgie Bennett, Adam Booth and the rest of Roering Lab past and present, and of course, the Ladies of Riverview, Ryan Seward, Kelley Rabjohns and Kristina Walowski. In addition, I thank the rest of the faculty and staff in the Department of Geological Sciences for fostering such a collaborative and supportive environment.

My research has benefited greatly from Michael Marden—including his insightful comments in the field and decades of knowledge on the Waipaoa that he was willing to share. I also greatly appreciate Peter Almond for teaching me how to properly dig a soil pit as well as Natalia Deligne and Laurel Childress for their field assistance and Julie Barkman for her EMPA assistance. I am also grateful to the 2012-2013 UO Field Geophysics classes for their help collecting the refraction survey data, Jered Hogansen for processing the data as part of his undergraduate honors thesis, Miles Bodmer for letting me convince him to help with this project and developing the workflow for

processing the passive array data, and Nathan Mathabane, Kristin Sweeney, Jill Marshall, and Joseph Byrnes for their always enthusiastic field assistance. Additionally, I would like to thank the owners of Te Hau and Te Kowhai Stations in New Zealand, and Roseburg Forest Products and ODOT in Oregon for granting field access.

I owe a lifetime of gratitude to my loving parents, who taught me to be an observant and inquisitive participant in the world and instilled my love for the outdoors, travel, and rocks from a young age. I also want to thank my brother and sister for always being there for me. And lastly, I want to thank the rest of my friends and family—near and far—for their everlasting encouragement and support, and in particular: Scott, for keeping me grounded, and Little Jerry, for keeping things in perspective.

Lidar data and aerial photographs were acquired by New Zealand Aerial Mapping (NZAM). Lidar for Vaughn was flown as part of a NCALM Student Seed Grant, and lidar for Cougar Creek was obtained from DOGAMI. Borehole logs and inclinometer data were graciously provided by Cornforth Consultants and ODOT. The Waipaoa research was supported by NSF Grant OCE-841111 to Joshua Roering as part of MARGINS Source-to-Sink (S2S) project.

To understanding the world just a little bit more.

TABLE OF CONTENTS

Chapter Page

Chapter Page

LIST OF FIGURES

Figure Page

Chapter II

LIST OF TABLES

Table Page

CHAPTER I

INTRODUCTION

In mountainous regions, landslides can dominate landscape evolution and sediment production, as well as pose a significant hazard to human lives, property, and infrastructure. Therefore, understanding the role of landslides in driving hillslope adjustment is critical to both long-term geomorphic studies and short-term hazard studies. The sensitivity of the hillslopes to tectonic, climatic, or human perturbations sets the pace of landscape evolution, which is reflected by sediment production and morphologic adjustment [e.g. *Whipple and Tucker*, 1999; *Lavé and Burbank*, 2004]. Over long (>500 ky) time periods, tectonic uplift may be balanced by erosion, but over shorter (<100 ky) periods a multitude of perturbations (e.g. climatic, seismic, or stochastic) can trigger feedbacks that disturb this balance. More recently, humans have become prolific landscape modifiers, displacing large volumes of sediment as a result of agriculture and other land-use changes—arguably making humans the most effective geomorphic perturbation at present [e.g. *Hooke*, 1994]. Deforestation and conversion of land to pasture or agriculture cause loss of soil cover and change hydrology [e.g. *Montgomery*, 2007], necessitating costly erosion and flood control projects—a pragmatic reason for understanding the magnitude of landscape response.

Quantifying the role of landslides in landscape evolution as well as hazards requires understanding the volume of sediment produced, the landslide type and failure style, and the frequency—or rate—of movement through time. Therefore, to quantify the role of landslides in landscape response requires temporal constraints on sediment flux that are often lacking in real landscapes [*Korup et al.*, 2010]. Here, though, I am able to uniquely analyze the landslide-driven hillslope response over millennial to decadal timescales and characterize multiple types of landslides (e.g. earthflows, shallow landslides, and deep-seated landslides) by applying a variety of geomorphological, geochemical, and geophysical tools and techniques (e.g. tephrochronology, lidar and air photo analysis, field and subsurface investigations, and seismic refraction) in the Waipaoa Basin (New Zealand) and Oregon Coast Range (USA).

In Chapter II, co-authored with Joshua J. Roering, Michael Marden (Landcare Research), Alan S. Palmer (Massey University), and Eric L. Bilderback (National Park Service) and published in *Geochemistry, Geophysics, Geosystems (G-Cubed)*, I reconstruct the past land surfaces through time for a sub-catchment of the Waipaoa Basin. The well-resolved tephra record in the Waipaoa allows me to fingerprint the plentiful tephra deposits in order to: date the rapidly eroding ridgelines, establish the timing of hillslope adjustment, and reconstruct the paleosurfaces from ~18 ka to present day. I can use these paleosurfaces to determine the catchment-averaged erosion rate through time.

In Chapter III, co-authored with Joshua J. Roering and under review in *Earth Surface Processes and Landforms (ESPL)*, I compare the post-18 ka erosion rates I determined in Chapter II to the historic erosion rates from the same study area. European settlement in the Waipaoa Basin in the late 1800s resulted in rapid deforestation and conversion of >90% of the landscape to pastureland, which triggered a prompt increase in hillslope erosion as widespread landslide complexes developed or reactivated in the weak underlying lithology. To quantify the rate and volume of historic hillslope degradation, I 1) use a 1956-2010 sequence of aerial photographs, lidar, and field reconnaissance to map the active landslides, 2) create a 'turf index' by classifying the digitized air photos based on extent and style of pastoral ground disruption, and 3) correlate the 'turf index' with downslope velocity in order to calculate the average annual sediment flux since the 1950s.

In Chapter IV, co-authored with Jered L. Hogansen, Douglas R. Toomey, Joshua J. Roering, and Miles A. Bodmer and in preparation for submission to *Engineering Geology*, I determine the depth and failure style of two deep-seated landslides. This style of landslide is a ubiquitous, yet poorly-studied, feature in the otherwise geomorphologically well-studied Oregon Coast Range (OCR). The role of large landslides has been largely ignored in previous studies [*Roering et al.*, 2005]—thus quantifying the volume and frequency of these larger features could challenge the notion that tectonic uplift balanced by seasonal shallow landslides and debris flows in the OCR [*Dietrich et al.*, 2003]. Furthermore, the paucity of historic failures results in a poor understanding of the triggering mechanism or failure style. Therefore, in Chapter IV, I test the utility of a well-established geophysical technique (i.e. seismic refraction) to

image the subsurface of these landslide deposits by comparing borehole logs and slope inclinometer data to the geophysical results.

In this dissertation, by coupling geochemistry, tephrochronology, air photos, lidar, geophysics, and field reconnaissance, I am able to quantify the role of landslides in landscape evolution as well as verify a technique for characterizing the subsurface of landslides with temporal and spatial resolution that is rarely achievable outside the lab.

CHAPTER II

QUANTIFYING TEMPORAL VARIATIONS IN LANDSLIDE-DRIVEN SEDIMENT PRODUCTION BY RECONSTRUCTING PALEOLANDSCAPES USING TEPHROCHRONOLOGY AND LIDAR: WAIPAOA RIVER, NEW ZEALAND

From Cerovski-Darriau, C., J. J. Roering, M. Marden, A. S. Palmer, and E. L. Bilderback (2014), Quantifying temporal variations in landslide-driven sediment production by reconstructing paleolandscapes using tephrochronology and lidar: Waipaoa River, New Zealand, Geochemistry, Geophysics, Geosystems, 15(11), 4117–4136, doi:10.1002/2014GC005467.

1. Introduction

Base level lowering driven by tectonic or climatic processes can cause differential incision in fluvial networks that drives transient hillslope response as slopes adjust to new channel elevations. Base level is controlled regionally by tectonic uplift and sea level fluctuations, and locally by changes in stream power or sediment supply that can promote valley incision or aggradation [e.g. *Merritts and Vincent*, 1989; *Bull*, 1991; *Schumm*, 1993]. The magnitude of base level lowering and the sensitivity of the hillslopes to these changes set the pace of landscape evolution, which is reflected by sediment production and morphologic adjustment [e.g. *Whipple and Tucker*, 1999; *Lavé and Burbank*, 2004]. Over long (>500 ky) time periods, tectonic uplift may be balanced by erosion, but over shorter (<100 ky) periods a multitude of perturbations (e.g. climatic, anthropogenic, seismic, or stochastic) can trigger feedbacks that disturb this balance. For example, over a glacial-interglacial cycle, climatic fluctuations often cause fluvial incision rates that far surpass tectonic rates [e.g. *Bull*, 1991; *Berryman et al.*, 2000; *Pazzaglia and Brandon*, 2001; *Wegmann and Pazzaglia*, 2002; *Litchfield and Berryman*, 2006; *Finnegan et al.*, 2014] , as well as periods of increased sediment production that promote valley aggradation and relief decline [e.g. *Whipple et al.*, 1999]. How landscapes respond to a transient pulse of river incision, especially in regions of active uplift, is key to

understanding regional and global sediment budgets [*Milliman and Syvitski*, 1992; *Warrick et al.*, 2013; *Larsen et al.*, 2014]. In mountainous regions, landsliding is the primary hillslope response to base level change, driving hillslope adjustment by modifying hillslope gradients and conveying sediment to channels and gullies for transport to continental margins [*Schmidt and Montgomery*, 1995; *Hovius et al.*, 1997; *Montgomery and Brandon*, 2002; *Ouimet et al.*, 2007; *Booth et al.*, 2013]. However, most landslide studies focus on historic occurrences, using event inventories associated with a single trigger (e.g. storm or earthquake) or regional inventories, which often lack temporal constraints [*Guzzetti et al.*, 2012, and references therein; *Larsen and Montgomery*, 2012]. More specifically, the progression of landslide-driven hillslope response over glacial-interglacial timescales has not been documented in a real landscape [*Korup et al.*, 2010]. In this study, we estimate the extent and timing of hillslope relaxation and landscape lowering via landsliding in response to >50 m of post-LGM river incision for an entire tributary catchment of the Waipaoa River, New Zealand (referred to hereafter as the Waipaoa).

In the Waipaoa, the fluvial response was almost immediate, seemingly synchronous with the post-LGM climate shift, however perched low-relief hillslopes are still adjusting to that base level fall [*Crosby and Whipple*, 2006; *Gomez and Livingston*, 2012; *Bilderback et al.*, 2014; *Marden et al.*, 2014]. The fact that some relict hillslopes are blissfully unaware of the fluvial incision supports the idea of a lag period before incision is translated to the hillslopes. This raises the question: What is the progression of hillslope adjustment? In other words, how rapidly do hillslopes respond to incision and what is the magnitude of the response? The lag time between fluvial and hillslope response is a well-known geomorphic concept [e.g. *Gasparini et al.*, 2007; *Hurst et al.*, 2013], however, it is poorly quantified in the field. Once hillslopes start to adjust, the time it takes to reach a new equilibrium, or even what that equilibrium form will be, is not well known. Therefore, it is difficult to ascertain from a modern landscape the status of hillslope adjustment, despite efforts by previous studies. At our study site, we can begin to address all of these questions by tracking temporal changes in hillslope adjustment following climate-driven fluvial incision using a sequence of four paleosurfaces defined by tephrochronology.

Previously, the lack of temporal control on erosion rates associated with post-LGM hillslope adjustment precluded us from definitively linking sedimentary records to landscape change. Here, reconstructing the evolution of a sub-catchment through time gives us the novel opportunity to: 1) measure how rapidly hillslopes respond to base level change, 2) quantify the progressive volume of sediment removed as the slopes re-grade over a post-glacial time interval, and 3) characterize how the continental margin records upland sediment production.

In this study, we use tephrochronology to date landslide activity and calibrate a surface roughness-age relationship derived from airborne lidar topography for an entire tributary catchment of the Waipaoa, referred to as the 'sub-catchment' or 'Mangataikapua catchment'. Using our roughness-age relationship, we can estimate the age of land-surface stability across the entire sub-catchment. We then use a sequence of reconstructed paleosurfaces to: 1) demonstrate how this catchment evolved, predominantly via landsliding, since the LGM in response to a climatically-driven base-level fall, 2) estimate the volume of sediment eroded, and 3) quantify how that erosion varies with time. Our results provide critical data needed to quantify how climate perturbs a real landscape on millennial timescales and thus imparts predictive capabilities in landscape evolution modeling. Most importantly, using our reconstructed paleosurfaces, we can show that the hillslope erosion rate is not constant through time. Our findings are reinforced by previously studied fluvial and offshore records that broadly corroborate our observed erosion rate trend, despite our study site being a small, anomalously landslide-prone sub-catchment in the Waipaoa Basin.

2. Study Area

The Waipaoa River, located on the East Coast of the North Island (New Zealand), is a rapidly eroding river that is highly sensitive to system-wide perturbations—from long-term tectonic uplift, to millennial scale climate fluctuations, to decadal land-use change, to periodic high magnitude storms. The copious amounts of eroded terrestrial sediments are well-preserved in sediment cores dispersed offshore in Poverty Bay, which makes the area an ideal system for tracking the 'source-to-sink' system over various timescales.

The 2,150 km^2 Waipaoa Basin extends from the Raukumara Ranges to Poverty Bay (Figure 1a). The Waipaoa is rapidly eroding through Cretaceous-Early Miocene marine sedimentary rocks that have been uplifted and deformed as part of the active forearc of the Hikurangi Margin (Figure 1b). Our study site, the 16.5 km^2 Mangataikapua catchment, is located 45 km upstream of Poverty Bay just below the confluence between the Waipaoa and Mangatu Rivers (see Figures A1-A3 for photos of the study area; see Appendix A for all "A" figures). The study site is mostly confined to a narrow band of weak Early Cretaceous mélange—a highly sheared mudstone in a smectitic matrix associated with the East Coast Allochthon. The mélange in the Mangataikapua catchment, and other similarly weak lithological units throughout the Waipaoa, are collectively referred to as 'landslide-terrain', or areas with pervasive earthflows, slumps, and gullies. The exception in this sub-catchment is the steep, boundary ridgelines that are medium-grained Miocene sandstone of Tolaga Group with locally glauconitic sandstone [*Mazengarb and Speden*, 2000] (Figure 1b).

Subduction of the Hikurangi Plateau—a thick section of the Pacific Plate obliquely subducting beneath the continental Australian Plate at ~45 mm yr^{-1} [*DeMets et al.*, 1994; *Wallace*, 2004]—caused broad scale deformation and rock uplift averaging 0.5-1 mm yr^{-1} over the past 1-2 My [*Litchfield and Berryman*, 2006]. Since the late Pleistocene, the Raukumara Ranges (mean elevation 1300 m) have been rapidly uplifting (3-4 mm yr^{-1}) due to anticlinal folding along the range crest where the Waipaoa headwaters is located [*Litchfield and Berryman*, 2006; *Gomez and Livingston*, 2012]. Uplift rates, determined from pairs of Quaternary fluvial terraces and analysis of sediment exhumation, decrease sharply by the central Waipaoa catchment (0.5-0.9 mm yr^{-1}) and at the Mangataikapua catchment approximate the long-term average (~0.7 mm yr^{-1}) determined from Late Tertiary mudstone burial depths [*Berryman et al.*, 2000; *Litchfield and Berryman*, 2006]. However, since the end of the Last Glacial Maximum (LGM) ~18 ka, river incision has far outpaced tectonically driven uplift such that climate appears to dictate the pace of transient periods of incision and erosion over glacial-interglacial cycles [*Berryman et al.*, 2000; *Litchfield and Berryman*, 2006; *Marden et al.*, 2014].

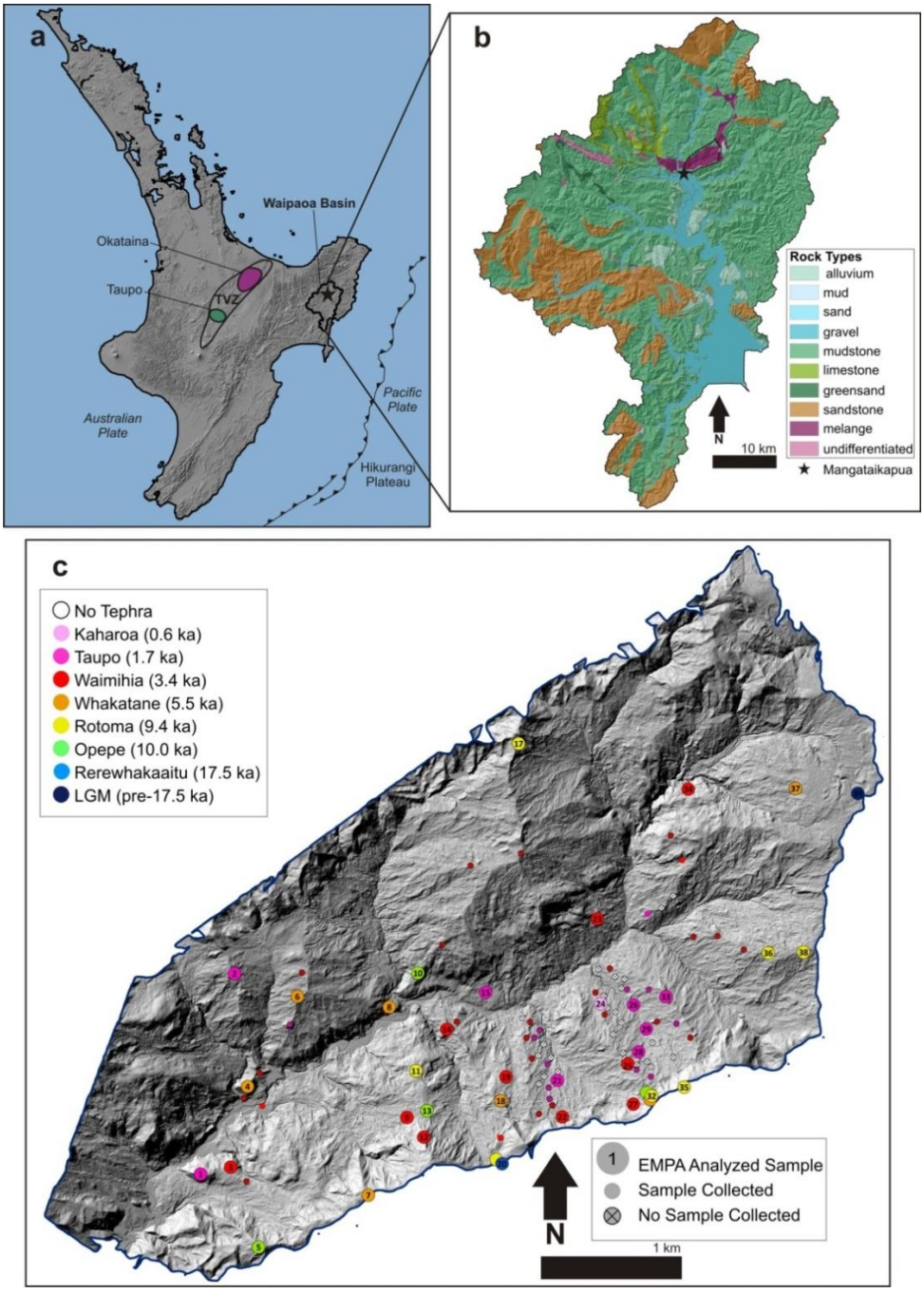

Figure 1. (a) The Waipaoa Basin is located on the East Coast of the North Island, New Zealand. The Mangataikapua study area is marked with the star. The Taupo Volcanic Zone is outlined on the 30 m hillshade, and the Taupo and Okataina Volcanic Centers (TVC and OVC) are highlighted in green and purple respectively. (b) Geologic map of the Waipaoa Basin with the mélange band in purple. The Mangataikapua catchment, located at the star, is 45 km upstream of Poverty Bay. (c) Mangataikapua hillshade (1 m lidar) with tephra sample locations colored by identified tephra. Numbers correspond to sample numbers. Larger circles indicate electron microprobe samples, circles with an "x" indicate tephra identified in the field.

Tectonically-driven and climatically exacerbated base level change, following the shift to a warmer, wetter climate after the Last Glacial Maximum (LGM) (~18 ka), caused the Waipaoa River to rapidly incise and re-grade [*Gage and Black*, 1979; *Berryman et al.*, 2000; *Marden et al.*, 2008; *Gomez and Livingston*, 2012]. Well-preserved fluvial cut and strath terraces throughout the Waipaoa Basin record the history of degradation (Figure A4). A thick (2-30 m) LGM gravel fill terrace (W1) is capped by 17.5 ka Rerewhakaaitu tephra, indicating the terrace was abandoned around the end of the last glacial cycle [*Eden et al.*, 2001; *Litchfield and Berryman*, 2005; *Marden et al.*, 2008, 2014]. Therefore, fluvial downcutting began within 1 ky of the climate shift, but the most rapid incision occurred through valley fill between 9.4-14.0 ka [*Marden et al.*, 2014]—which closely correlates with the accumulation of gravel in Poverty Bay 9-11 ka [*Brown*, 1995; *Berryman et al.*, 2000]. Following the removal of the valley fill, the river began to incise into bedrock. Terraces in the headwater reaches of the Waipaoa River record up to 120 m of post-LGM incision, and approximately 55 m of incision at the junction with the Mangataikapua. In the late Holocene, the Waipaoa was likely a boulder-armored bedrock river, until the arrival of the European settlers [*Berryman et al.*, 2000]. Now the modern Waipaoa is a braided alluvial river system at the junction with the Mangataikapua, transitioning to a meandering gravel-bedded river downstream with an average suspended sediment load of 15 Mt yr^{-1}, or a sediment yield of 6800 t km^{-2} yr^{-1} [*Hicks et al.*, 2000].

The Waipaoa is 100-200 km downwind of the Taupo and Okataina Volcanic Centers in the Taupo Volcanic Zone (TVZ) (Figure 1a). The TVZ is one of the most active rhyolitic eruption centers since the late Pleistocene [*Smith et al.*, 2005]. Tephra frequently mantles the landscape immediately following eruption with 5-20 cm deposits, and a multitude of studies have analyzed and characterized these deposits [e.g. *Froggatt and Lowe*, 1990; *Eden et al.*, 2001; *Shane et al.*, 2003; *Smith et al.*, 2005; *Lowe et al.*, 2013]. In the Waipaoa, there are 15-20 eruptions spanning from 55 ka to 0.636 ka with an average recurrence interval of approximately 2 kys (Table 1), which have been used to date terraces and landslides throughout the region [e.g. *Berryman et al.*, 2000; *Litchfield and Berryman*, 2005; *Marden et al.*, 2014; *Bilderback et al.*, 2014.].

During the LGM, the Waipaoa was a sub-alpine environment with sparse vegetation and sediment supplied mainly by periglacial processes [*Gage and Black*, 1979; *McGlone*, 2001]. Periglacial sediment supply far outpaced sediment transport capacity in the channels, causing fill terraces to form [*Berryman et al.*, 2000; *Litchfield and Berryman*, 2005].

Table 1. Major TVZ eruptions present in the Waipaoa Basin

Tephra Name[a]	**^{14}C Age** (±2 s.d) (cal. yr BP)	**TVZ Volcanic Center**
Kaharoa	**636±12**[b]	**Okataina**
Taupo	**1718±10**[b]	**Taupo**
Waimihia	**3401±108**[b]	**Taupo**
Whakatane	**5526±145**[b]	**Okataina**
Mamaku	7940±257[b]	Okataina
Rotoma	**9423±120**[b]	**Okataina**
Opepe	**9991±160**[b]	**Okataina**
Poronui	11170±115[b]	Taupo
Karapiti	11460±172[b]	Taupo
Waiohau	14009±155[b]	Okataina
Rotorua	15635±412[b]	Okataina
Rerewhakaaitu	**17496±462**[b]	**Okataina**
Okareka	21858±290[b]	Okataina
Kawakawa/Oruanui	25358±162[b]	Taupo
Omataroa	**32755±1415**[c]	**Okataina**

[a]Bold type indicates tephra sampled in the Mangataikapua catchment [e.g. *Gage and Black*,1979; *Berryman et al.*,2000; *Eden et al.*, 2001; *Smith et al.*, 2005; *Lowe et al.*, 2008; *Marden et al.*, 2008]
[b]Age model reported in *Lowe et al*. [2013]
[c]Age model reported in *Smith et al*. [2005]

The interglacial climate is marked by increased precipitation and mean annual temperature, and decreased seasonality [*Gomez et al.*, 2004]. The current Waipaoa climate is highly dependent on the El Nino-Southern Oscillation cycle (established ~4 ka [*Gomez et al.*, 2004]), with mean annual rainfall of ~1500 mm. The shift to warmer, wetter conditions promoted the establishment of a podocarp forest and increased river discharge thereby reducing sediment transport from the hillslopes and increasing fluvial transport capacity enough to mobilize accumulated gravels [*McGlone*, 2001; *Litchfield and Berryman*, 2005, 2006]. This combination of feedbacks accelerated river incision, which in turn steepened lower slopes while leaving many 'relict' upper slopes perched above the river.

Europeans began settling in the Poverty Bay region approximately 200 years ago, preceded by the Maori people 600-800 years ago [*Wilmshurst et al.*, 1999]. The Maori populated mostly coastal areas, whereas the Europeans quickly migrated to the uplands and converted ~90% of the native podocarp forests to pastureland using repeated slash-and-burn techniques [*Gage and Black*, 1979; *Wilmshurst et al.*, 1999] (Figure A5). This land-use change increased hillslope erosion, leading to modern aggradation in the channel. The Mangataikapua is currently ~80% pastureland and ~20% *pinus radiata*; the latter planted in a NZ government-led effort during the mid-20th century to reforest parts of the Waipaoa. Additionally, local areas of poplar and willow are planted in the Mangataikapua in attempt to slow the most egregious erosion.

The effects of post-LGM fluvial incision and vegetation change, as well as recent deforestation, promoted hillslope adjustment via landsliding that continues today. In the Waipaoa today, we observe a spectrum of landslide styles as follows: 1) shallow, soil-dominated landslips that fail catastrophically in response to high intensity rainfall, 2) slow moving, shallow to deep, earthflows that activate seasonally due to wetting and drying of clay-rich material, but persist for decades to millennia, and 3) deep translational or rotational slumps that fail incrementally to catastrophically due to de-buttressing at the toe. Collectively these three landslide styles, and the extensive gully systems developed on them, are the dominant hillslope sediment production and transport mechanisms active since the post-LGM climate shift [*Gage and Black*, 1979; *Marden et al.*, 2005, 2008, 2014; *Page and Lukovic*, 2011; *Bilderback et al.*, 2014]. We assume all three styles were

present in some combination in the past, and we use the generalized term ‘landslide’ to refer to all three collectively when we cannot definitively differentiate between the mass movement styles.

3. Tephrochronology

In order to quantify how landslide activity varies over time, and therefore the rate and volume of hillslope erosion, we first need a way to determine the age of relict surfaces. To do so, we collect tephra samples from various ridges throughout the Mangataikapua, analyze the glass chemistry, and compare the signature to previously published geochemical and geochronological datasets. From these datasets, we identify the volcanic event and, therefore, age of the sample. Given that surface roughness tends to decrease with age due to diffusive processes (e.g. soil creep), we can relate those ages to a lidar-derived topographic roughness index, which enables us to define an empirical relationship between the surface roughness and age. Using this relationship, we classify the entire landscape by tephra age in order to reconstruct a sequence of paleosurfaces and thus calculate erosion rates through time.

3.1. Methods

The Mangataikapua catchment is blanketed with a distinctive tephra layer from the well-characterized Taupo Volcanic Zone (TVZ) every ≤2 ky since the LGM (Table 1). In the absence of sufficient in-situ quartz or carbon for radiometric dating (e.g. cosmogenic, luminescence, or radiocarbon), this plentiful tephra record makes tephrochronology an accessible and inexpensive means to constrain landscape age at a range of spatial scales. For each TVZ eruption that reached the Mangataikapua, we assume that the tephra: 1) is deposited across the landscape, 2) can be uniquely identified, 3) is sequentially deposited, and 4) accumulates with time until removed by slope failure [*Preston and Crozier*, 1999]. Thus, the age assigned to the basal tephra will correspond to the timing of the first eruption since that location was last disturbed by landsliding, or duration since stabilization [*Lang et al.*, 1999], as was successfully demonstrated in neighboring sub-catchments [*Bilderback et al.*, 2014]. Therefore, using the techniques outlined in *Bilderback et al.* [2014], we can constrain the date of ridgeline stabilization to

within ~2 kys. To do this, we excavated 128 soil pits along ridges with various length scales from the Mangataikapua outlet to the headwaters (Figure 1c) and collected tephra samples in 5-10 cm increments from different soil horizons, focusing on the basal tephra in contact with bedrock.

To identify each tephra sample, we used the major-element glass chemistry determined from electron microprobe analysis (EMPA). Tephra from the TVZ have distinctive chemical signatures [*Lowe et al.*, 2008 and references therein], but are difficult to differentiate in the field (with a few exceptions discussed below), therefore we relied on the glass composition to correlate our samples with known tephra. Tephra samples were separated from the surrounding soil material, cleaned in an 11% solution of sodium hexametaphosphate, and rinsed through a 63 μm sieve with the coarse fraction retained for analysis. The tephra was embedded in epoxy resin and polished for EMPA. We analyzed 39 basal tephra samples on the University of Oregon CAMECA SX-100 microprobe using 15 kV accelerating voltage, 10 nA beam current (Na, Si, K, Al, and Fe), 50 nA beam current (Mg, Ca, Mn, and Ti), and variable count times to maximize detection limits and minimize analytical errors. For each sample, 12 unique glass shards were analyzed (n=12). Detection limits at a 99% confidence interval are <0.008 wt % for all elements except Ti (<0.02%), giving average % analytical errors (±1 s.d.) of Si ±0.04%, K ±0.1%, Al ±0.4%, Na ±0.5%, Ca ±1%, Mg ±3%, Fe ±3%, Mn ±10%, Ti ±20%. Results were run with glass standards and known TVZ tephra as controls. Analytical totals for individual shard compositions were typically 96-98% with remaining mass attributed to secondary hydration; therefore all analyses are normalized to 100% to aid comparison with published data (Table B1; see Appendix B for all "B" tables).

The most common way to differentiate tephra units is to compare the abundance of major oxides between glass samples. For the TVZ, bulk glass chemistry allows easy identification of the source volcanic center for tephra <30 ky old [*Smith et al.*, 2005]. Individual eruptions can be further differentiated using binary plots of diagnostic oxide pairs [*Smith et al.*, 2005; *Lowe et al.*, 2008] (Figure 2a). Most frequently K_2O vs. CaO is used, but we found that FeO, MgO, MnO, and TiO_2 also help distinguish between compositionally similar eruptions (Figure B1; see Appendix B for all "B" figures). The spread of the data can also be diagnostic, as some eruptions had multiple phases (e.g.

Whakatane) or bimodal compositions (e.g. Rerewhakaaitu), although this can also result in overlapping compositions (e.g. Whakatane/Rotoma, Kawakawa/Omataroa, Taupo/Opepe) (Figure 2a). To distinguish between two compositionally similar tephra, we used sample depth. We found age to increase linearly with depth (slope=0.048)—similar to the trend (slope=0.056) found by *Bilderback et al.* [2014] (Figure 2b)—allowing for differentiation between overlapping compositions with disparate ages.

We initially identified unique tephra samples by grouping similar compositions using a combination of oxide bi-plots (Figure 2a) and cluster analysis. Then, we compared similar compositions to a compilation of known TVZ tephra compositions (435 total samples) using discriminant function analysis (DFA). DFA is a widely used statistical method for grouping collections of unknown and known data, including tephra, however it is highly dependent on the quality of the reference data used to develop the comparison model [e.g. *Lowe*, 2011, and references therein]. To improve the comparison model and to simplify our analysis, we first separated the tephra by source volcano, and then determined the most likely eruption based on source (Table 1). Using DFA, the TVZ volcanic source—Taupo Volcanic Center (TVC) or Okataina Volcanic Center (OVC) (Figure 1a)—can be determined with 97% accuracy based on the accuracy of the reference dataset (n_{total}=435, n_{miss}=13) (Table B3). After separating our data according to source, TVC eruptions can be predicted with 94% accuracy (n_{total}=128, n_{miss}=8) and OVC eruptions with 60% accuracy (n_{total}=307, n_{miss}=122) (Table B3). Errors likely arise due to variation in the EMPA analytical precision, heterogeneity within OVC-sourced samples (e.g. OVC more often produces multi-phase and bimodal eruptions), and possibly even misidentified control samples [*Lowe et al.*, 2008]. The tephra identification accuracy, particularly for OVC tephra, was improved by using the depth-age relationship and checking the composition against OVC glass oxide bi-plots. If we could not confidently identify the oldest tephra, we analyzed the overlaying tephra or re-probed the initial sample.

Due to the wide sampling interval (5-10 cm), as well as in-situ mixing, many samples contain shards of younger tephra. In six cases, only a single shard of an older tephra was identified, and was thus discarded in favor of the next oldest tephra (see Appendix B; Table B1). For an additional 69 unanalyzed soil pits, we were able to assign

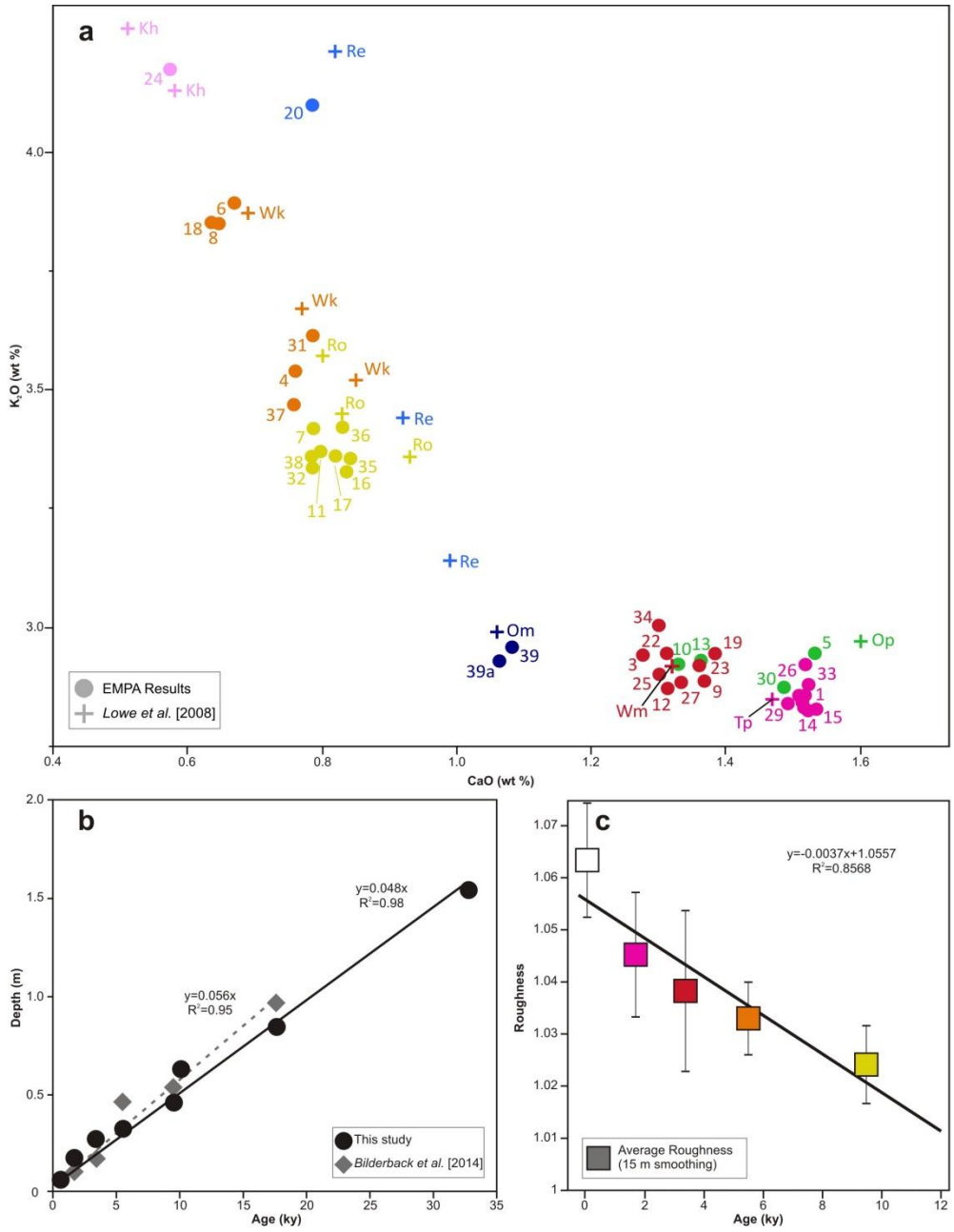

Figure 2. (a) Example binary plot of tephra composition comparing K_2O vs. CaO for all probed samples. Circles represent resulting compositions from microprobe analysis, and crosses represent control sample composition from Lowe et al. [2008] (Kh=Kaharoa, Op=Opepe, Om=Omataroa, Ro=Rotoma, Re=Rerewhakaaitu, Tp=Taupo, Wm=Waimihia, Wk=Whakatane). Sample numbers correspond to sample locations (Figure 1c). Full major oxide composition of all probed samples is included in the Table B1. (b) Depth-age relationship for Mangataikapua samples (black circles) binned by tephra age compared to approximate depth-age relationship determined by Bilderback et al. [2014] (grey diamonds). (c) Linear fit of mean roughness for binned samples of Rotoma, Whakatane, Waimihia, Taupo, and no tephra (with 15 m smoothing). Characteristic roughness for each timestep was determined from the linear fit.

ages of Waimihia (3.4 ka), Taupo (1.7 ka), or Modern (<0.6 ka) based on field observations alone (Table B2). Waimihia tephra deposits as a distinctive thick lapilli layer resembling coarse sugar dominating the soil matrix below 10 cm, and Taupo has obvious pumice clasts (2-7 mm) that make up ~10-20% of the A horizon. If no pumice was visible in the A horizon, the pit was assumed to have no tephra.

3.2. Results

Recent (Kaharoa, 0.6 ka) to very old (pre-Rerewhakaaitu, >17.5 ka) tephra is preserved in the Mangataikapua (Figure 1c, Figure 2a, Table 1), but 80% of the probed samples are from 4 tephra units: Taupo (1.7 ka), Waimihia (3.4 ka), Whakatane (5.5 ka), and Rotoma (9.4 ka) (Table B1). We used these four most sampled tephra units to define our landscape reconstruction intervals: LGM-Rotoma, Rotoma-Whakatane, Whakatane-Waimihia, and Waimihia-Modern. Conveniently, these breaks are similar to those used by other Waipaoa studies [e.g. *Bilderback,* 2012; *Bilderback et al.*, 2014; *Leithold et al., 2013; Marden et al., 2014]*, allowing for comparison of processes and events. Lastly, we could not confidently distinguish between the oldest two tephras, Omataroa (32.8 ka) and Kawakawa (25.4 ka), due to ambiguity in the glass chemistry and control tephra. The oldest tephra in the study area was likely Omataroa, but because pre-Rerewhakaaitu ages are less relevant for our landscape reconstructions, we grouped all tephra older than Rerewhakaaitu into one group referred to as "LGM".

Using the combination of methods discussed above, the possibility of misidentifying recent tephra is low. Regardless, there are four samples identified as Opepe (10.0 ka) that are likely younger (Figure 2a) and six samples identified as a younger tephra (i.e. with n=1) that are likely older. However, even if all questionable samples are misidentified, the probability of falsely identifying samples as older is only 10% (n_{total}=39, $n_{younger}$=4) and falsely identifying samples as younger is 15% (n_{total}=39, n_{older}=6). Therefore, the potential misidentification of these few samples does not significantly affect our sub-catchment analysis.

4. Roughness Calculations

Surface roughness is a measure of surface texture variability, and can be used to infer age of active processes, e.g. fault scarps [*Avouac*, 1993], landslides [*McKean and Roering*, 2004], and alluvial fans [*Frankel and Dolan*, 2007]. Sharp features in the landscape tend to become more diffuse with time such that recent surface disturbances will produce more variability in surface texture. For example, our lidar data reveals a clear distinction between the smooth, relatively undisturbed morphology in the headwaters that is being progressively smoothed with each tephra fall and the rough, rumpled texture of the actively eroding, landslide-dominated terrain further downstream (Figure 1). By quantifying the roughness from a DEM, and using it as a proxy for surface age, we can then extrapolate our tephra-derived surface ages across the entire Mangataikapua catchment.

4.1. Methods

We calibrated a surface roughness model using the ages determined from our sampled basal tephra. Surface roughness was calculated by applying Jenness DEM Surface Tools (www.jennessent.com) to the 1 m lidar DEM. The Jenness model computes the ratio of a fitted surface area to a plane over a 3x3 pixel window. The resulting surface roughness values approach 1 for smooth areas and increase with increasing roughness, often not exceeding 2-3 [*Jenness*, 2004]. To account for local variations due to roads, ponds, recent failures, etc., we calculated the roughness value at each node as the average roughness over a 15 m radius (see Appendix B; Table B1). We binned pits by age and fit a line to the average roughness for each post-LGM bin, excluding the Opepe points due to the ambiguity discussed above (Figure 2c).

4.2. Results

The final smoothed roughness map shows that over 70% of the landscape is younger than Kaharoa (0.6 ka), whereas less than 1% is older than LGM (Table 2); confirming that our study area is a very actively eroding landscape. The smoothed roughness map (Figure 3) captures the distinction between the older headwaters (mainly blue and yellow), main ridgelines (mainly yellow), and recently active earthflows (pink to

no color), and can be used to create tie-points for paleosurface reconstruction through time.

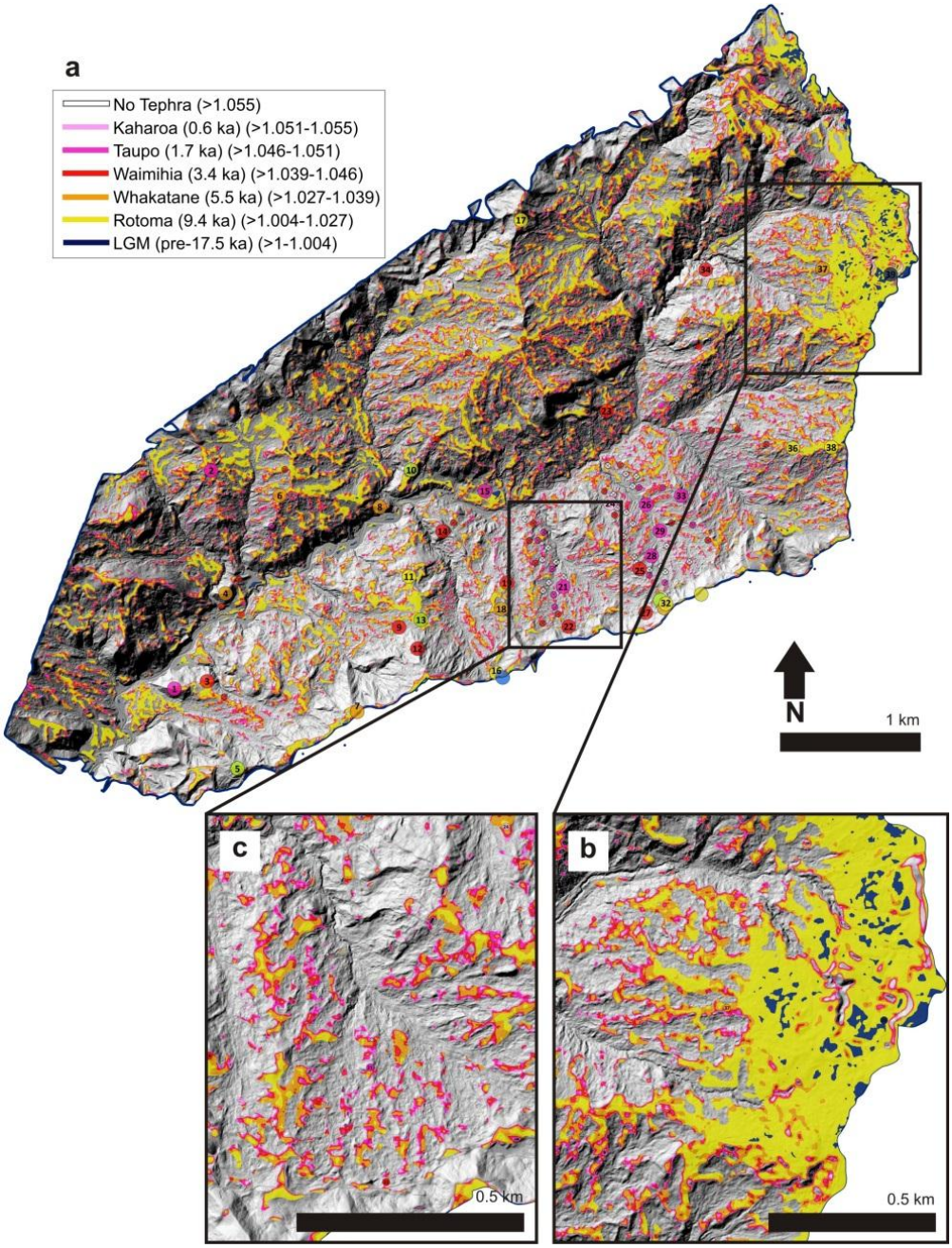

Figure 3. (a) Final roughness map for the Mangataikapua catchment overlain on 1m lidar hillshade. Roughness ratio values are colored by bins established using the linear fit found in Figure 2c. Original sample locations from Figure 1c are included for verification of roughness-age approximation. (b) Inset of the relict Mangataikapua headwaters where the land surface is predicted to be Rotoma or older (yellow-blue). (c) Inset of a tributary in the upper watershed where much of the land surface is active earthflows (no color) separated by young interfluves (red-pink).

We tested various roughness-age fit functions by iteratively comparing to our tephra data to the predicted ages using different scales of spatial averaging. We smoothed the original roughness data over 3, 10, 15, 20 m windows to estimate average roughness, filtered by high curvature values to eliminate active earthflows (Figure 3a), and then compared the predicted roughness age for each pit to the actual tephra age. We found that a 15 m smoothing window and a linear fit was the best predictor of the roughness-age relationship (local success rate=85%), despite the linear regression having a lower r^2 value than when we used a power law (see Appendix B; Figure B3). Thus we used the linear fit with the smoothed roughness data to generate the roughness distribution for the four timesteps. If we included the potentially misidentified Opepe points, our results were unaffected; therefore it is reasonable to assume that a 10-15% tephra misidentification rate does not significantly affect the roughness-age relationship. For the 15% of pits incorrectly predicted by the linear fit, 67% of those ages are underestimates. Therefore, overall there is only a 10% probability of inflating the volume due to underestimating the age.

5. Reconstruction of Paleosurfaces

Paleosurfaces serve as a reference datum from which subsequent elevation change can be calculated [e.g. *Clark et al.*, 2006], which is useful for quantifying rates of landscape evolution and volume of sediment eroded through time. In order to reconstruct the post-LGM progression of the Mangataikapua landscape, we first approximated the paleochannel profile for each of the four timesteps, and then combined the paleochannels with the corresponding paleoridge network and the modern catchment boundary derived from lidar analysis to generate a sequence of interpolated paleosurfaces.

5.1. Methods

Given the absence of preserved terraces along the Mangataikapua stream, likely owing to intense landslide activity, paleochannel profiles were calculated by fitting a theoretical longitudinal profile from the headwaters to the corresponding terrace elevation along the mainstem Waipaoa at the Mangataikapua outlet. The paleochannel profile for

each of the four timesteps was calculated using the equations [*Whipple and Tucker*, 1999]:

$$z_*(x_*) = z_{0_i} + C_i \left(1 - \frac{hm}{n}\right)^{-1} (1 - x_*^{1-\frac{hm}{n}}) \quad (1)$$

$$z_* = z/H \quad (2)$$

$$x_* = x/L \quad (3)$$

where z_* is the elevation normalized for channel relief (H), x_* is the position downstream normalized for channel length (L), z_0 is the elevation of the Waipaoa terrace at each timestep, h is a modified Hack's constant, $\frac{m}{n}$ is concavity, and C is the uplift/erosion rate coefficient for each timestep. A simplified valley axis profile, to eliminate sinuosity in the plan-view channel form, was used for L. For h, we used Hack's relationship to calculate a specific value for the Mangataikapua (see Appendix B), and found h=1.4-1.6. The best fit model for the channel profiles requires h=1.6 and $\frac{m}{n}$=0.4, similar to previously established values of 1.55 and 0.55 respectively for the entire Waipaoa Basin [*Whipple and Tucker*, 2002; *Crosby and Whipple*, 2006], and a linearly decreasing constant for each timestep (C_{LGM}=1.07, C_{Ro}=1.04, C_{Wk}=1.02, C_{Wm}=1.01) (Figure 4a) (Table 2). In all Waipaoa tributaries, the concavity of the LGM terrace is similar to Holocene-aged terraces [*Marden et al*., 2014], thus we assume a constant $\frac{m}{n}$ for each paleochannels.

The LGM terrace elevation was taken from the GPS surveyed W1 terrace, the last aggradational terrace before post-LGM downcutting, located at Whatatutu township near the confluence of the Mangataikapua and the Waipaoa Rivers. In the absence of lower Holocene-aged terrace remnants preserved here, subsequent elevations for the Rotoma, Whakatane, and Waimihia terraces (Table 2) were calculated using the fluvial incision rates reported in *Marden et al.* [2014] and are within 5 m of terrace heights at Whatatutu [*Marden et al.*, 2014]. The Mangataikapua headwater elevation was allowed to vary slightly (<20 m) to account for incision of ~1 mm yr^{-1}, which equals the estimated background uplift rate.

We created a network of the major paleoridges by delineating adjacent areas with no drainage area from the modern lidar, then we overlaid this network on the surface roughness map, and assigned ages to each ridgeline segment based on the modal surface roughness within a 15 m buffer—average ridge crest width—for each segment (Figure 4c). The surface roughness of each ridge segment corresponds to an age based on the roughness-age relationship (Figure 2c). Using the modal value eliminates the meter-scale variations in topography, captures the distribution of ridge ages, and creates linear segments of the same age that represent ridgelines of a given age. We used only the

Table 2. Paleochannel reconstruction parameters

Timestep Name	**Age** (ky)	**Percent of Catchment Area**[a]	**Terrace Elevation,** z_0 (m)[b]	**Paleochannel Constant,** C[b]
LGM	>17.5	0.4	135	1.07
Rotoma (Ro)	9.4	10.1	105	1.04
Whakatane (Wk)	5.5	7.7	90	1.02
Waimihia (Wm)	3.4	4.2	85	1.01
Taupo (Tp)	1.7	2.7	n/a	n/a
Kaharoa (Kh)	0.6	1.9	n/a	n/a
Modern (Mod)	0	73	0	n/a

[a]Determined from final roughness raster
[b]Parameters used for paleochannel profiles

corresponding ridges for each timestep to define the four paleosurfaces. However, because there were insufficient ridgelines of LGM age to constrain the surface for that interval, we used outlines of the LGM roughness surfaces (dark blue in Figure 3b) to define the LGM paleosurface and added "ghost" points 8 m above the modern surface in 5 poorly fit locations downstream, which is equivalent to a conservative ~0.4 mm yr^{-1} of erosion, in order to minimize erroneously predicted areas of aggradation between paleosurfaces.

The modern catchment boundary was used for all paleosurface reconstructions. This is a valid assumption because this divide is predominantly Rotoma (9.4 ka) or older, and we have no constraints on the elevation or position pre-Rotoma stabilization. Therefore, we assume the paleosurface boundary was at least as high as the modern elevation, and our volume calculations are a minimum for the oldest (LGM-Rotoma) time

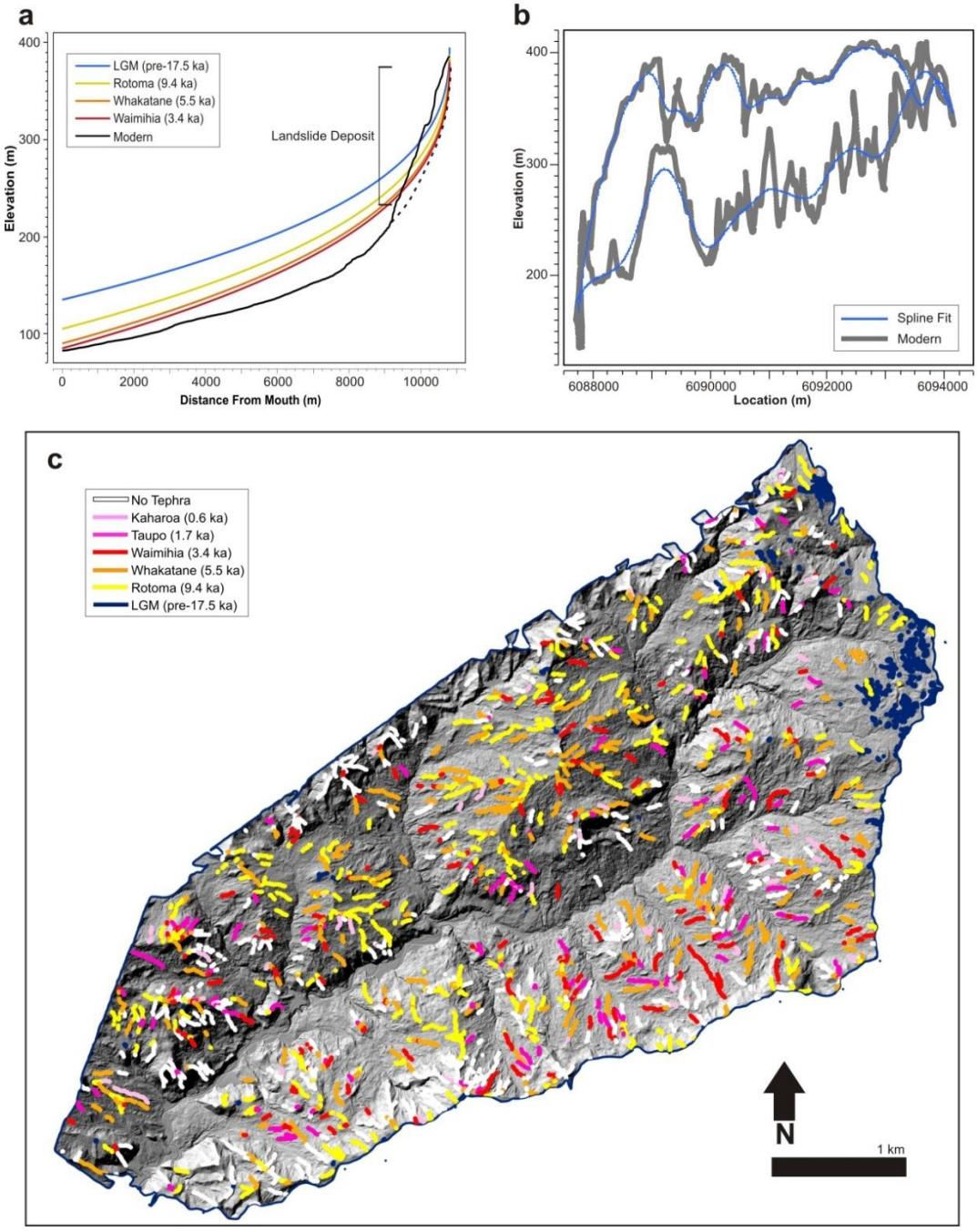

Figure 4. Inputs used for surface reconstruction. (a) Four paleochannel longitudinal profiles, calculated using a concavity, $\frac{m}{n}$, of 0.4 and a fixed output based on surveyed or calculated past terrace elevations. The modern channel profile (black) is dashed where the channel bed is buried by a recent landslide deposit. (b) Boundary elevation for the Mangataikapua watershed (thick grey line) fitted with a stiff, 1D spline (thin blue line). Spline fit elevations are used as an approximate boundary elevation for each paleosurface. (c) The ridgeline network for the Mangataikapua colored by age as determined by the roughness-age relationship established in Figure 2c. Relict LGM surfaces in the headwaters are represented by points.

interval. We used a stiff, 1D spline curve to smooth the modern catchment boundary to minimize introduction of spurious ridges and valleys to the paleosurfaces (Figure 4b).

The smoothed catchment boundary, ridge segments, and paleochannel were combined for each of the four timesteps and used as tie points for interpolation. We fit a paleosurface to the points using MATLAB's cubic spline interpolation (Figure B5). The modern 1 m lidar DEM (flown in 2010) was then subtracted from each fitted paleosurface to get a total elevation change—which is equal to volume change—for each time interval (Table 3). The elevation difference between each subsequent paleosurface (i.e. LGM and Rotoma) was calculated to estimate relative volume change and compared to the volume difference calculated by cumulatively subtracting each interval's elevation change from the modern surface to test for internal consistency (Table 3).

5.2. Results

We found the volume difference between the LGM-reconstructed surface and modern DEM to be approximately 0.5 ± 0.06 (s.d.) km^3 (Figure 5; Table 3). Of that total volume, 60% of the erosion occurred between LGM (>17.5 ka) and Rotoma (9.4 ka) (0.3 ± 0.05 (s.d.) km^3) (Figure 5a; Table 3). The residual topography highlights localized areas of rapid erosion between the LGM and Rotoma paleosurfaces (green area in Figure 5a). This result confirms a phase of widespread slumping or deep-seated earthflows that we observe in the field and is described elsewhere in the Waipaoa [e.g. *Gage and Black*, 1979; *Marden et al.*, 2014; *Bilderback et al.*, 2014]; and although the modelled surface does not likely correspond with the exact location of slumps, it does reflect the representative volume change. The subsequent intervals show small volume changes, corresponding to only 0.08 ± 0.02 (s.d.) km^3 and 0.02 ± 0.01 (s.d.) km^3 for the Rotoma-Whakatane and Whakatane-Waimihia intervals respectively (Figure 5b-c). For the most recent interval, Waimihia-Modern, volume change increased to 0.12 ± 0.03 (s.d.) km^3 and is more evenly distributed across the landscape. In the residual topography map for each time interval, some locales are misrepresented as aggradational (purple areas in Figure 5). For example, a recent large earthflow that traverses the upper Mangataikapua stream (Figure 4a) accounts for much of the aggradational bias in the headwaters. However, the total aggradational area only represents 5-10% of the terrain, thus the influence on

volume differences is negligible, and we calculated the aggradational nodes as null values. For each interval, we converted volume to erosion rates and found the rates decrease from 2.3 ± 0.4 (s.d.) mm yr^{-1} (LGM-Rotoma), to 1.2 ± 0.4 (s.d.) mm yr^{-1} (Rotoma-Whakatane), to 0.7 ± 0.3 (s.d.) mm yr^{-1} (Whakatane-Waimihia), and then increase to 2.2 ± 0.6 (s.d.) mm yr^{-1} (Waimihia-Modern) (Figure 6; Table 3).

Table 3. Volume change and erosion rates

PALEOSURFACE to MODERN[a]	**Volume** (km^3)	***s.d.***	***s.e.***	**Erosion Rate** (mm/yr)
LGM	0.46	*0.06*	*0.02*	1.6
Rotoma	0.20	*0.09*	*0.03*	1.3
Whakatane	0.13	*0.04*	*0.02*	1.5
Waimihia	0.12	*0.03*	*0.01*	2.2

RECONSTRUCTION DIFFERENCES[b]	**Volume** (km^3)	***s.d.***	***s.e.***	**Erosion Rate** (mm/yr)
LGM-Ro	0.31	*0.05*	*0.02*	2.3
Ro-Wk	0.08	*0.02*	*0.01*	1.2
Wk-Wm	0.02	*0.01*	*0.00*	0.7
Wm-Mod	0.12	*0.03*	*0.01*	2.2
Total	0.53	*0.06*	*0.02*	

CUMULATIVE SUBTRACTION[c]	**Volume** (km^3)	***s.d.***	***s.e.***	**Erosion Rate** (mm/yr)
LGM-Ro	0.26	*0.11*	*0.04*	1.9
Ro-Wk	0.06	*0.09*	*0.04*	1.0
Wk-Wm	0.01	*0.05*	*0.03*	0.4
Wm-Mod	0.12	*0.03*	*0.01*	2.2
Total	0.46	*0.15*	*0.06*	

INTERVAL[d]	**Erosion Rate** (mm/yr)	*s.d.*	*% error*
LGM-Ro	2.3	*0.4*	*16.2*
Ro-Wk	1.2	*0.4*	*31.9*
Wk-Wm	0.7	*0.3*	*39.7*
Wm-Mod	2.2	*0.6*	*25.5*

[a]Difference in eroded volume between reconstructed paleosurface and 2010 lidar DEM
[b]Difference between subsequent paleosurfaces
[c]Cumulative subtraction to verify calculated differences
[d]Erosion rates for each subsequent timestep

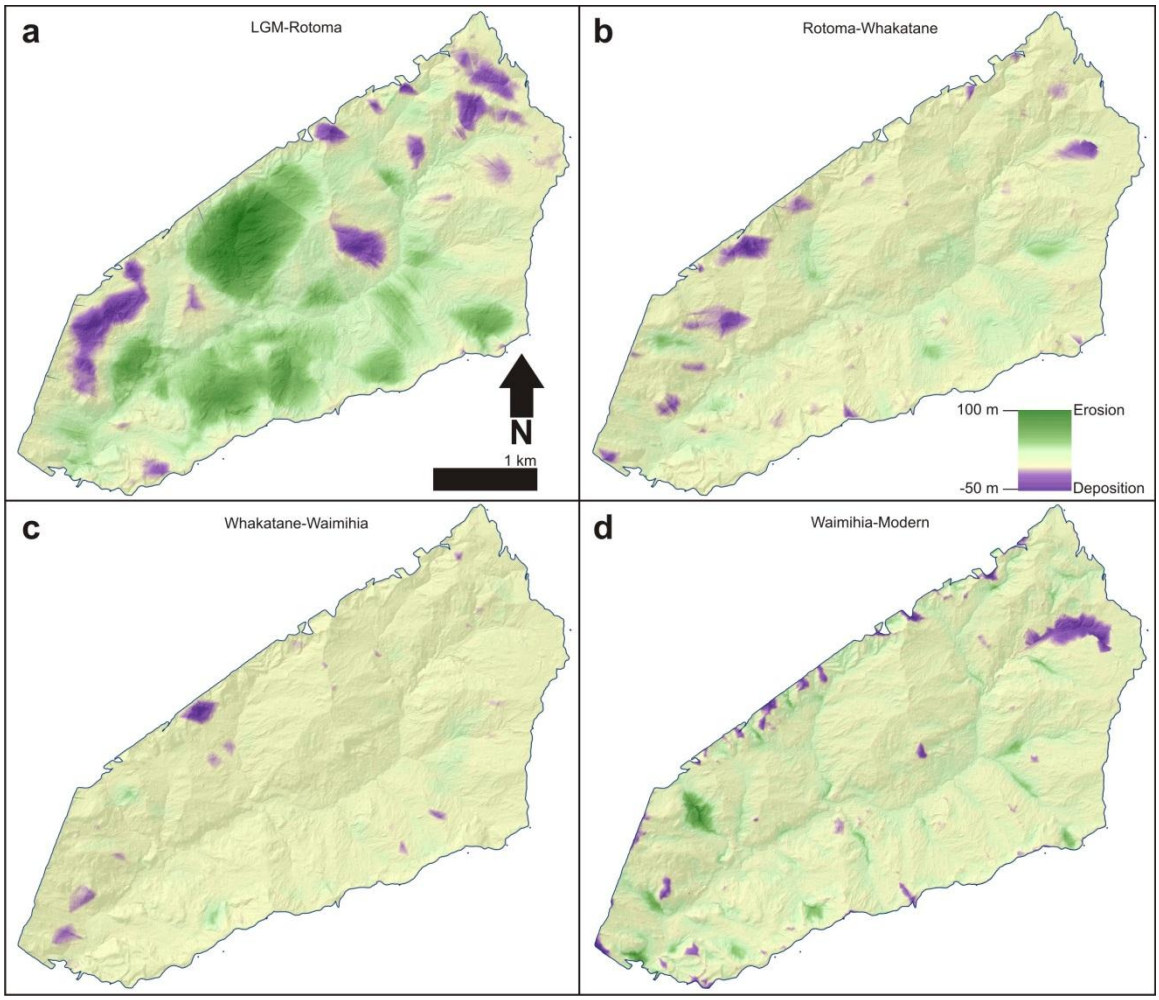

Figure 5. Elevation difference between: (a) LGM (>17.5 ka) and Rotoma (9.5 ka) paleosurfaces, (b) Rotoma (9.5 ka) and Whakatane (5.5 ka) paleosurfaces, (c) Whakatane (5.5 ka) and Waimihia (3.4 ka) paleosurfaces, and (d) Waimihia (3.4 ka) paleosurface and 2010 lidar DEM. Green is the greatest net positive change, yellow is minimal change, and purple is net negative change. Negative change occurs in areas of surface misfit that are falsely represented as aggradation. See text for discussion. The elevation difference corresponds to the volume change for this 1 m DEM.

To confirm the robustness of our results, we tested various combinations of relict tie points and fitting surfaces, and used the variation between reasonable combinations to calculate the standard deviation and error for the volumes and erosion rates. This variability is based on the difference between combinations that cover the maximum, minimum, and most likely paleolandscape elevations, and therefore span all possible end members for each paleolandscape reconstruction (see Appendix B for more details). The

standard deviation for each estimated volume change is 10-40% (Table 3). We found a similar magnitude error exists for the volume difference calculated for each time interval (20-40%)—again based on the variability between trials (Appendix B; Table B4)—with the greatest uncertainties for the two slowest eroding time intervals (Table 3). Most importantly, we found much of the error derives from the topographic subtraction (up to 40%), which overshadows the smaller errors in tephra misidentification (10-15%) and the roughness-age relationship (10%).

6. Discussion

6.1. Volume of Terrestrial Sediment Eroded Post-LGM

Previous studies in the Waipaoa have focused on post-LGM fluvial incision, which is a significant sediment source along the mainstem of the Waipaoa and major tributaries characterized by wide valleys with substantial sediment storage [*Marden et al.*, 2008, 2014]. However, we demonstrate that hillslopes are also significant contributors of sediment, especially in sub-catchments like the Mangataikapua, with narrow valleys and thus minimal valley storage. Previously, landslide volume-area scaling relationships developed for the upper Waipaoa and extrapolated for the entire basin—based on lidar, air photo, and field investigations [*Page and Lukovic*, 2011; *Bilderback*, 2012]—found the total volume of sediment generated by just by landslides above the LGM (W1) terrace is roughly comparable to that of fluvial incision below the W1[*Marden et al.*, 2008, 2014]; indicating that including solely landslides will roughly double the terrestrial contribution. At our study site, we found nearly 30 m of post-LGM catchment-averaged lowering. To put our results into context, *Marden et al.* [2014] estimated that fluvial incision and valley excavation accounts for 14.1 km^3 of the post-LGM terrestrial sediment [*Marden et al.*, 2014], equating to an average post-LGM lowering of 6 m for the entire Waipaoa Basin. So, by comparison, we found a 400% increase in the terrestrial sediment production volume normalized by study area, quantitatively demonstrating that hillslopes are indeed a significant terrestrial sediment source in the overall post-LGM sediment budget.

Although the Mangataikapua is a single small sub-catchment in an area of anomalously weak landslide-dominated terrain, it is a relevant contributor to the overall

Waipaoa sediment budget. The average post-LGM erosion rate for the Mangataikapua (1.6 mm yr^{-1}) (Table 3) is double the previous catchment-averaged denudation rate for the entire Waipaoa (0.8 mm yr^{-1}) [*Bilderback*, 2012], implying these small areas of weaker rock are particularly prolific sources of sediment. Assuming all the mélange areas (Figure 1b) erode at similar rates to the Mangataikapua, then the 1.4% of the Waipaoa Basin composed of this weak lithology contributes nearly 1 km^3, or ~10%, of the terrestrial sediment transferred to the offshore depocenter.

6.2. Timing of Hillslope Response

Hillslope response to the glacial-interglacial climate shift can be conceptualized, based on our analysis, as four main phases: 1) hillslope indifference, 2) initial destabilization, 3) slope stabilization, and 4) reinvigorated landsliding.

The initial, fluvial-only, phase lasted a couple thousand years and occurred contemporaneously throughout most of the Waipaoa Basin [*Crosby and Whipple*, 2006; *Gomez and Livingston*, 2012; *Bilderback et al.*, 2014; *Marden et al.*, 2014]. Speleothem, marine, and pollen records [*Wright et al.*, 1995; *McGlone*, 2001; *Williams et al.*, 2005, 2010] indicate the transition to a warmer, wetter climate occurred by 18.2 ka. Soon after, the Waipaoa River switched from aggradation to degradation, marked by the abandonment of the W1 terrace capped by Rerewhakaaitu tephra (17.5 ka). During this phase most hillslopes remained insulated from this climate shift until the post-LGM podocarp forest was established 11.5-15.5 ka [*McGlone*, 2001], accounting for the lag time between the fluvial-only and hillslope-coupled response to base level fall. The vegetation likely slowed diffusive hillslope transport and allowed channels to significantly undercut and debuttress hillslopes [*Bilderback et al.*, 2014], which corresponds with the end of phase one. The second phase is marked by widespread hillslope adjustment via landsliding. The timing of slope destabilization is constrained by the absence of Waiohau (14.0 ka) and preservation of Rotoma (9.4 ka) tephra in the Mangataikapua, which is contemporaneous with other Waipaoa sub-catchments [*Bilderback et al.*, 2014]. *Bilderback et al.* [2014] found no tephra older than Rotoma in any augered landslides, and we found no evidence of Waiohau tephra in the study area, while Rotoma tephra capped most main ridgelines in the sub-catchment (Figure 3);

evidence of a prolific initial phase of hillslope destabilization beginning after 14.0 ka and ending by 9.4 ka. During this phase, increased fluvial incision debuttressed slopes and caused widespread destabilization [*Black*, 1980; *Marden et al.*, 2005; *Gomez and Livingston*, 2012; *Bilderback et al.*, 2014]. By contrast, elsewhere in the Waipaoa hillslopes grade to the uneroded terraces buttressing their base, indicating the importance of fluvial incision in modulating slope response [*Black*, 1980; *Marden et al.*, 2008; *Bilderback et al.*, 2014]. In the Mangataikapua, large arcuate headscarps along the catchment boundaries (e.g. scarps ~1 km due north of tephra sample 8 and between samples 16 & 22 in Figures 1c and 3a) and down-dropped benches from Rotoma-covered ridgelines (e.g. tephra sample 32 (and underlying) in Figures 1c and 3a) are evidence of deep-seated slumps and rotational slides during this phase. Following the second phase, erosion rates slowed dramatically (Figure 6). We argue that slower erosion rates during this third phase reflect earthflows that slowed or stopped prior to the Waimihia eruption, as evident from minimal erosion during the Whakatane-Waimihia interval (3.4-5.5 ka) and preservation of abundant Waimihia tephra on interfluves of older earthflow material between active, modern earthflows in the Mangataikapua, and inactive earthflows (≥100s of years old) below indigenous forest in the Waipaoa headwaters [*Gage and Black*, 1979]. In the fourth and final phase, reinvigorated landsliding throughout the sub-catchment likely reflects anthropogenic activity following European settlement. Erosion rates over the Whakatane-Modern time interval (2.2 mm yr^{-1}) are rapid and similar to those for the LGM-Rotoma interval (2.3 mm yr^{-1}). The elevated erosion rate is unlikely to be influenced by time-dependent averaging (i.e. 'Sadler' effect) because any potential recording bias is minimized, or even underestimated, by using the spatially averaged total sediment volume [*Kirchner et al.*, 2001; *Finnegan et al.*, 2014; *Sadler and Jerolmack*, 2014]. Instead, the rapid erosion rate is likely skewed heavily by the widespread deforestation and subsequent land-use change over the past ~200 years, meaning that most of the erosion during the Waimihia-Modern time interval was accomplished over the latter ~5% of that timestep; consistent with widespread historic aggradation downstream.

The timing of hillslope evolution within the Mangataikapua catchment closely matches the sequence of hillslope destabilization and adjustment described by *Bilderback*

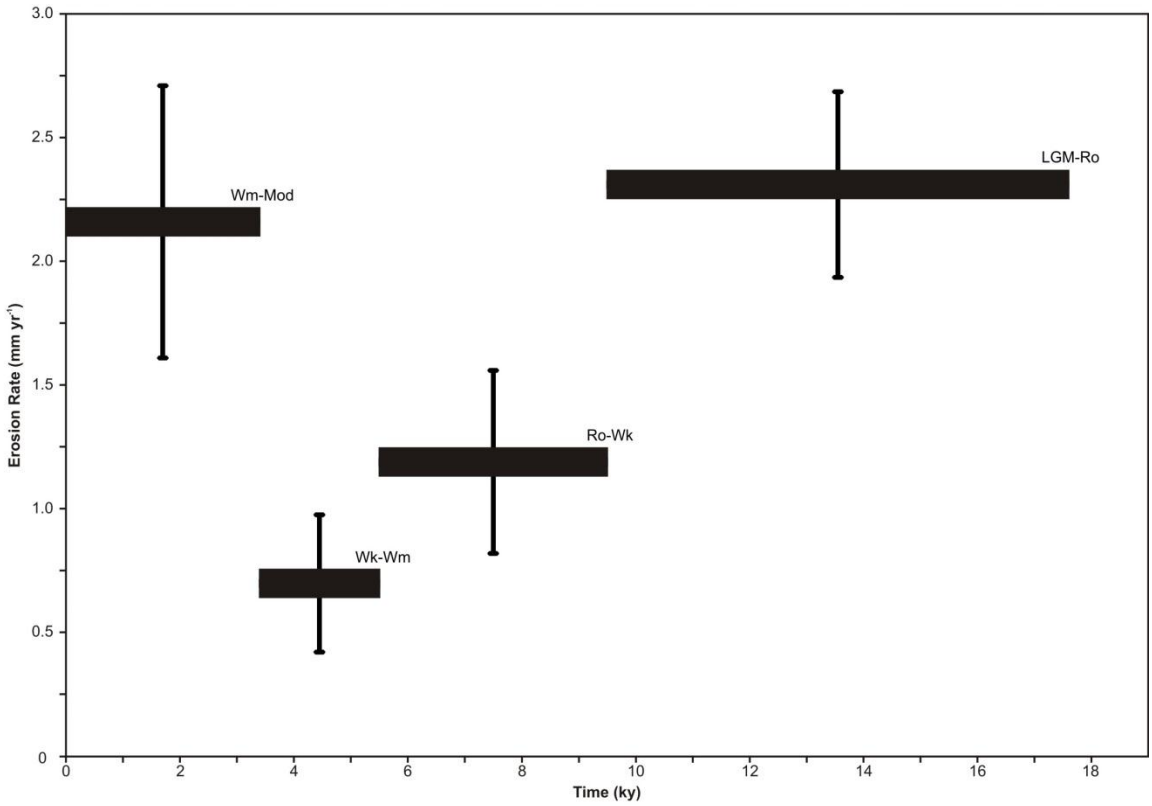

Figure 6. Average erosion rates (± 1 s.d.) calculated for each time interval (Mod=Modern, Wm=Waimihia, Wk=Whakatane, Ro=Rotoma, LGM=Last Glacial Maximum).

et al. [2014] for the upper Waipaoa, which reflects the downcutting history for much of the Waipaoa [*Marden et al.*, 2008, 2014]. Additionally, the pattern of upland erosion fluctuations is also seen in offshore sedimentation fluctuations. Offshore sediment accumulation has remained approximately constant through most of the Holocene [*Foster and Carter*, 1997; *Gomez et al.*, 2004; *Orpin et al.*, 2006; *Leithold et al.*, 2013], but was higher immediately following the LGM transition [*Foster and Carter*, 1997] and increased dramatically in the past century due to deforestation [*Foster and Carter*, 1997; *Wilmshurst et al.*, 1999; *Gomez et al.*, 2004; *Orpin et al.*, 2006; *Leithold et al.*, 2013]; as reflected, broadly, by our sub-catchment erosion rates (Figure 6; Table 3).

More precise correlation between upland, or onshore, and offshore records is complicated by sediment dispersal on the continental shelf, post-LGM marine transgression, and inputs from other smaller coastal rivers (e.g. Waimata). Additionally, most cores have insufficient dateable material older than ~10 ka to constrain the ages of deep offshore sediments. However, from the available offshore data, we note: 1) periods

of coarse sedimentation or increased deposition that correspond to the initial fluvial incision and hillslope destabilization phases trending from gravel (9-11 ka) to deep-sourced, finer sediments [*Berryman et al.*, 2000; *Gomez et al.*, 2004; *Leithold et al.*, 2013], 2) a near constant Holocene (post-10 ka) accumulation rate that corresponds to equilibrating hillslopes and decreasing erosion rates, and 3) a 2-5 times increase in offshore sedimentation over the past few centuries [e.g. *Foster and Carter*, 1997; *Gomez et al.*, 2004; *Orpin et al.*, 2006; *Wilmshurst et al.*, 2011] that corresponds to historic land-use change and increased erosion that we observe in this study. Also, recent deposition of deep-sourced carbon [*Leithold et al.*, 2013] and fluvial sediment indicative of increased gully activity [*Marsaglia et al.*, 2010] corroborate accelerated historic erosion via earthflows and shallow landslides throughout the Waipaoa [*Gage and Black*, 1979; *Marden et al*., 2014].

An onshore/offshore correlation is not surprising since the Waipaoa sedimentary system is thought to be tightly coupled between source and sink, meaning there is minimal evidence of significant delays due to sediment storage between terrestrial sediment production and offshore sediment deposition [*Hicks et al.*, 2000; *Phillips et al.*, 2007; *Gerber et al.*, 2010]. However, one major divergence between our study and offshore records is a sharp pulse of coarse material and terrestrial carbon preserved in sediment cores between 3.6-5 ka, attributed to landslides during a period of increased storminess [*Gomez et al.*, 2004; *Leithold et al.*, 2013]. A similar pulse of activity is not reflected in our hillslope erosion rates over the same interval (Whakatane-Waimihia). This does not necessarily imply that our hillslope record is inconsistent with the offshore record. Perhaps this signal originates from increased storm precipitation and/or intensity driving sediment transfer from onshore sediment sinks (e.g. floodplains) or other areas of easily eroded bedrock, rather than changing the pace of sediment production in the Mangataikapua.

6.3. Pattern of Response and Hillslope Transience

Currently less than 1% of the Mangataikapua remains as pre-LGM terrain and only ~5% consists of ridgelines identified as Rotoma-age—indicating they remain unaltered by historic earthflows. Despite the fact that most of the Mangataikapua has

been altered by landslides, the landscape is still in disequilibrium and adjustment is on-going as evident from various estimates of landscape transience. Most of the relict (≥18 ka) landforms are confined to the upper watershed, upholding the proposed temporal and spatial upstream progression of hillslope adjustment. From morphologic evidence, present day earthflows appear to follow this pattern of younging upstream (Figure B4a). For example, earthflows in the upper watershed are smaller in area and generally deposit in axial gullies (Figure B4b), whereas downstream single earthflows are more developed and often encompass entire sub-catchments with toes intersecting the main Mangataikapua channel (Figure B4c).

In addition to morphologic evidence, we can use surface roughness to test for a signature of transient adjustment. To characterize which areas of the Mangataikapua have adjusted to the post-LGM base level fall, we correlated surface roughness with distance from the headwaters. To do this, we binned the landscape into 2.5 km^2 increments by downstream drainage area—with an initial 0.5 km^2 bin for the relict headwaters—and calculated the median roughness as the age proxy for each bin. The median roughness in the relict, unaltered headwaters is half that of the rest of the sub-catchment; indicating an older average age as expected (Figure 7). The subsequent downstream bins have similar median roughness, although the landscape roughens slightly near the outlet (Figure 7). This analysis suggests that hillslope response has translated through much of the Mangataikapua but is not yet complete. If fluvial incision rates have slowed or ceased, we might expect to see a hillslope response with: 1) the oldest, smoothest areas of unadjusted terrain in the headwaters, 2) the roughest, youngest terrain in the middle reaches, and 3) an older terrain again near the outlet that has equilibrated with the new base level [e.g. *Gallen et al.*, 2011]. However, other than the relict smooth terrain in the headwaters, the rest of the sub-catchment has a relatively uniform younger roughness-age. Therefore, slope adjustment has initiated through most of the sub-catchment, but the ultimate morphologic adjustment is incomplete; indicating the timescale needed to reach equilibrium, or completely adjust to the new base level, is longer than the post-LGM (~18 ky) time period.

The prevalent common age (Rotoma, 9.4 ka) for much of the sub-catchment likely reflects the rapid initial phase of hillslope adjustment between LGM and Rotoma. Given

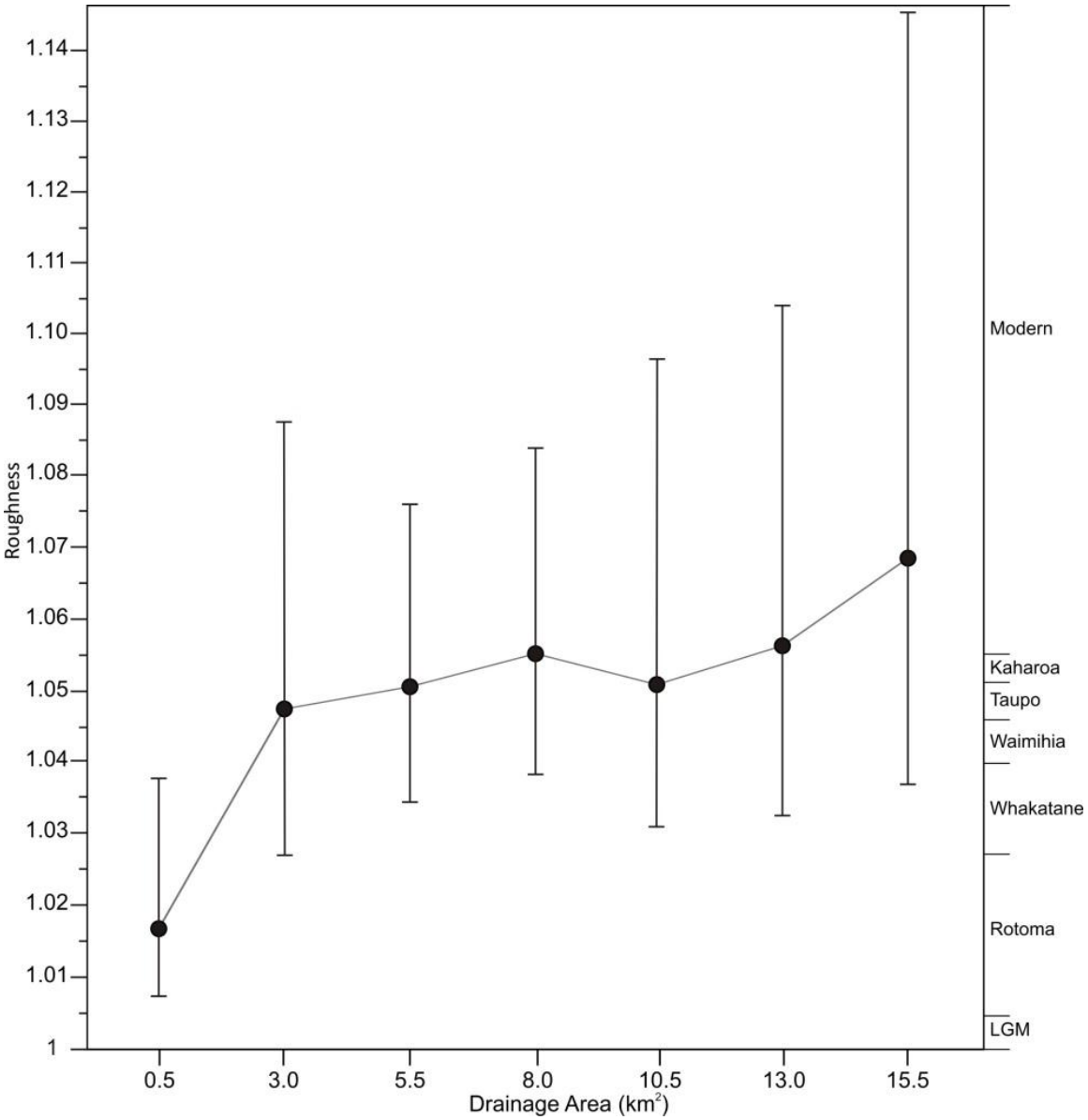

Figure 7. Trend in average catchment roughness by drainage area, using median roughness to minimize the influence of outliers, calculated from the final roughness map (Figure 3). Roughness is a proxy for surface age and shows the decreasing age of the landscape from the headwaters to the outlet, and the distinct difference between the unadjusted, relict hillslopes in the headwaters and the adjusting hillslopes downstream. Error bars span the interquartile range for each roughness bin.

sufficient fluvial incision to debuttress the slopes throughout the catchment, the signal of widespread failure dominates and still persists in the landscape today. More recent earthflows and smaller landslides may not have affected a large enough areal extent to change the overall mean roughness, or more likely, are acting similarly everywhere to

maintain a nearly uniform median roughness as evident from the field, lidar, and, possibly, reconstruction data (Figure 5d). However, the paleosurface reconstructions likely do not have the spatial resolution to resolve a transgressive wave of erosion characteristic of a transient landscape, and the relatively uniform distribution of volume change (Figure 5d) may reflect the differing resolution between the paleosurface and the lidar rather than a process shift. Regardless, the lack of age discrepancies between the downstream, middle, and upstream reaches of the Mangataikapua indicate the hillslopes continue to adjust. Therefore, despite the weak lithology facilitating a more rapid response than elsewhere in the Waipaoa, the hillslopes are still in a transient state. With time, most relict surfaces will be re-graded by landslides. However, the pace of adjustment is influenced by the decreasing drainage area upstream and potentially the presence of knickpoints [*Crosby et al.*, 2007]—now obscured by landslide deposits or diffused due to the weak substrate—which aids the preservation of relict surfaces in the headwaters.

The basic pattern of hillslope erosion in our study area can be explained by changing base level. Hillslope-channel coupling has long been understood to drive relief adjustment. The fundamental idea being that hillslopes grade to a base level, and the gradient is set by the strength of hillslope material while the rate of adjustment is set by the rate of base level change and celerity of knickpoints [*Crosby and Whipple*, 2006]. The weak mélange that underlies our sub-catchment was unable to support over-steepened slopes, therefore massive and rapid base level fall locally induced widespread slope failure and hillslope adjustment in the Mangataikapua. Slope failures were likely fast-moving and deep-seated in response to elevated incision rates at the outlet of the Mangataikapua between 9.4-14 ka [*Marden et al.*, 2014]. As incision rates decreased through the Holocene [*Berryman et al.*, 2010; *Gomez and Livingston*, 2012; *Marden et al.*, 2014], and knickpoints either stalled or diffused out, we would expect landsliding to slow in concert as inferred by decreasing post-Rotoma erosion rates. In addition, vegetation change can concurrently affect hillslope adjustment. For example, tree growth—like during the transition from shrubland to forest cover in the Waipaoa—can stabilize hillslopes by decreasing infiltration and anchoring soil and bedrock to the slopes. We suggest that a more pronounced vegetation-hillslope-channel feedback

manifested during periods of slower fluvial incision and/or aggradation post-Rotoma, which allowed forest cover to establish and further retard landsliding until historic deforestation reinvigorated erosion. Thus, hillslope-channel interactions are dominantly controlled by base level when base level change is rapid; but additional factors—such as vegetation—become increasingly important as the pace of base level changes slows or the landscape approaches its new equilibrium form. Based on the distribution of surface roughness, we propose that the Mangataikapua is a transient landscape that was nearing equilibrium with the current climate and lithology. However, widespread earthflows reactivated following deforestation have caused increased erosion, leading to significant aggradation, which has slowed fluvial incision—again perturbing the hillslope-channel response.

7. Conclusion

By reconstructing the paleolandscape, we calculate that the total post-LGM hillslope sediment contribution from the Mangataikapua catchment is 0.5 km^3 (or a catchment-averaged erosion rate of 1.6 mm yr^{-1}), which is double the previous hillslope erosion estimate when normalized by study area. Although the Mangataikapua is a small area of exceptionally weak lithology, our study shows that landslide-dominated areas of the landscape contribute a disproportionate amount of sediment and hillslopes are a significant terrestrial component of the Waipaoa sedimentary system. The main phase of slope destabilization and hillslope adjustment occurred between the deposition of Waiohau (14.0 ka) and Rotoma (9.4 ka), driven by rapid fluvial incision that steepened hillslopes temporarily stabilized by the newly established podocarp forest. This major phase of landsliding was followed by pervasive landslide activity, likely predominantly earthflows, that continues to shape the landscape. Despite the Mangataikapua being a unique sub-catchment that is responding more rapidly to the post-LGM climate shift than the rest of the Waipaoa, the overall processes, timing, and patterns of response are similar—and, notably, still on-going. The initial lag in hillslope adjustment, coupled with slowed incision in the upstream reaches of tributaries, is likely why relict terrain remains in the headwaters, unaltered, as of yet, by landslides. Therefore, after ~18 ky, hillslopes in the Mangataikapua are still actively adjusting to a climate-driven base level fall,

showing the disparate timescales over which fluvial and hillslope processes are active despite relatively close coupling between the two process regimes.

8. Bridge

In this chapter (Chapter II), I used tephrochronology to establish the timing of ridgeline lowering. From this timing, I was able to reconstruct the post-LGM paleolandscape and calculate the catchment-averaged erosion rate through time. Therefore, in this chapter, I was able to determine the long-term (~18 kys) erosion rate for the Mangataikapua. In the following chapter (Chapter III), for comparison, I will determine the short-term (decadal) historic erosion rates for the Mangataikapua.

In this chapter, I determined that erosion rate had returned to the background uplift rate of 0.7 mm/yr by the Waimihia eruption (3.4 ka), indicating that the hillslopes had likely stabilized by then. However, I found a sharp increase in erosion rates over my last time interval (Waimihia-Modern), which I hypothesize is due to recent human disturbance of the landscape. In the following chapter, I will determine whether this increase could be entirely due to an order of magnitude greater erosion rate caused by anthropogenic land-use change since the beginning of the 20th century.

CHAPTER III

INFLUENCE OF ANTHROPOGENIC LAND-USE CHANGE ON HILLSLOPE EROSION IN THE WAIPAOA RIVER BASIN, NEW ZEALAND

In review at *Earth Surface Processes and Landforms (ESPL)* as co-authored material with Joshua J. Roering. I developed the workflow, completed all the mapping and analyses, created the figures, and wrote all the text with feedback and editorial assistance from J. J. Roering.

1. Introduction

Landscapes respond to external perturbations over a variety of timescales, including million-year tectonic forcing, millennial to decadal climate fluctuations, and minutes-long high intensity storms or large magnitude earthquakes. While Earth's landforms primarily reflect the interaction of climatic and tectonic forces over long timescales (e.g. Molnar and England, 1990; Montgomery and Brandon, 2002; Whipple, 2009), more recently, humans have become prolific landscape modifiers. In relatively short amounts of time, human activities can displace massive quantities of sediment during mining and construction, and even larger volumes as a result of agriculture and land-use change (Hooke, 1994, 2000; Montgomery, 2007; Wilkinson and McElroy, 2007)—making humans arguably the most effective geomorphic agent at present.

Globally, denudation over geological time averages 10s of meters per million years while the present rate from agriculture averages 100s of meters per million years (Wilkinson and McElroy, 2007). This acceleration has implications for soil sustainability from the local to the global scale. Deforestation and conversion of land to pasture or agriculture causes loss of soil cover and changes hydrology (e.g. Montgomery, 2007), necessitating costly erosion and flood control projects (e.g. Allsop, 1973)—a pragmatic and immediate reason for understanding the magnitude of landscape response. Furthermore, soil conservation and reforestation is important to protect and restore arable/pastoral land to support a growing population (e.g. Montgomery, 2007) and to reestablish native vegetation to improve habitats and carbon cycling (e.g. Schlesinger and

Andrews, 2000). Thus, by quantifying anthropogenic erosion rates, we can begin to predict the pattern and pace with which humans perturb geomorphic processes in order to inform future soil conservation or erosion mitigation projects (Montgomery, 2007; Pelletier et al., 2015).

Previous studies have shown that anthropogenic erosion rates surpass natural erosion rates, even by orders of magnitude (e.g. Hewawasam et al., 2003; Hooke, 2000; Marden et al., 2014; Massa et al., 2012; Reusser et al., 2015). These large increases in erosion are likely to produce a geomorphic legacy that persists beyond the anthropogenic perturbation by changing the morphology of hillslopes and channels—either directly (e.g. Walter and Merritts, 2008) or indirectly (e.g. Glade, 2003). Here, we calculate the anthropogenic erosion rate and track the landscape response more than a century after land-use change.

In the Waipaoa Basin (North Island, New Zealand), humans have had a profound influence on soil erosion and landscape evolution. The Waipaoa River has one of the highest sediment yields in the world, and this has been largely attributed to human modification of the landscape (Fuller et al., 2015; Gage and Black, 1979; Hicks et al., 2011, 2000; Kettner et al., 2007; Marden et al., 2014; Wilmshurst et al., 1999). Overall, the total annual suspended sediment load is estimated to have increased >6 times since the arrival of European settlers in the late 1800s (Kettner et al., 2007). The weak lithologic units that comprise much of the Waipaoa are easily erodible and predisposed to mass wasting events (e.g. slumps, earthflows, deep-seated and shallow landslides), which—in conjunction with the gullies developed on these landslide complexes—contribute as much as 20% of the modern suspended sediment in the river system (Gage and Black, 1979; Marden et al., 2008, 2014; Page and Lukovic, 2011).

Europeans began settling in the Poverty Bay region approximately 200 years ago, preceded by the Maori people 600-800 years ago (Wilmshurst et al., 1999). The Maori populated mostly coastal areas, whereas the Europeans quickly migrated to the uplands and converted ~90% of the native podocarp forests to pasture using repeated slash-and-burn techniques (Gage and Black, 1979; Wilmshurst et al., 1999). By the 1920s most of the forest clearance and conversion was complete (Figure A5). The loss of vegetation caused a loss of soil reinforcement and an increase in soil moisture (Henderson and

Ongley, 1920; Marden, 2012; Pearce et al., 1987; Zhang et al., 1993), both of which promote mass wasting and gully erosion that continues today (Gage and Black, 1979; Marden et al., 2005). This increase in hillslope erosion led to detrimental channel aggradation and loss of floodplains, which decreased fertile agricultural land and increased destructive floods (Allsop, 1973; Henderson and Ongley, 1920). By the early 1900-1920s the settlers noted the prevalence of new landslides and increased river turbidity (Allsop, 1973; Howard, 1976). In the 1960s concerted reforestation efforts commenced to stabilize hillslopes and slow erosion in the Waipaoa (Allsop, 1973; Marden et al., 2005), and recent studies show that the reforestation has been successful in some regions of the Waipaoa (Marden, 2012 and references therein).

In this paper, to quantify the impact of a human-driven land-use change on the Earth's surface, we determined the sediment flux from a Waipaoa River tributary catchment over the past 50 years and compared the value to previously determined erosion rates for the past thousands to millions of years from the same catchment. This study area is well-suited for determining the anthropogenic influence on erosion because we are measuring the legacy effects from a short, but widespread, period of intense land conversion from native forest to pasture by European settlers. Other regions like the Oregon Coast Range (USA) or the Appalachian Mountains (USA), which are also heavily influenced by anthropogenic land-use change, have undergone stochastic and repeated regional disturbances due to intensive logging and agriculture (Benda and Dunne, 1997; Beschta, 1978; Reusser et al., 2015; Walter and Merritts, 2008). Therefore, because our study area has had comparatively minor changes to land-cover and grazing in recent decades, we could document the residual effects from the initial land-use change and track the landscape response through time. In particular, we: 1) used a combination of field studies and historic aerial photographs to calculate erosion rates from 1956-2010, 2) compared the erosion rates to vegetation cover and stream discharge, proxies for land-use and rainfall respectively, to determine the relative influence of land cover and climate, and 3) compared the historic erosion rates to previously determined long-term erosion—both since the Last Glacial Maximum (LGM) (~18 ka) and over the past few million years. This unique combination of tools and previously published data allowed us

to determine how much influence post-settlement land-use change exerts on long-term erosion rates and sedimentation records.

2. Study Area

The 2,150 km^2 Waipaoa Basin—located on the East Coast of the North Island, New Zealand (NZ)—extends from the Raukumara Ranges to Poverty Bay (Figure 1a). The Waipaoa River is rapidly eroding through Cretaceous-Early Miocene marine sedimentary rocks that have been uplifted and deformed as part of the Hikurangi subduction zone (Figure 1b). The river was a boulder-armored bedrock river until the arrival of European settlers (Berryman et al., 2000; Gage and Black, 1979). Now, the modern Waipaoa River has aggraded ~10 m at the study site outlet (Campbell, 1946), and boasts an average suspended sediment load of 15 Mt yr^{-1}, or a sediment yield of 6800 t km^{-2} yr^{-1} (Hicks et al., 2000). The Waipaoa Basin is located 100-200 km downwind of the Taupo Volcanic Zone (TVZ) (Figure 1a), which last had a major eruption 636 years ago with smaller historic eruptions in 1886 (Tarawera), 1945 (Ruapehu), and 1995-1996 (Ruapehu) (e.g. Gage and Black, 1979; Johnston et al., 2000).

Our study site, the ~16 km^2 Mangataikapua catchment, is located 45 km upstream of Poverty Bay at Whatatutu, just below the confluence between the Waipaoa and Mangatu Rivers (Figure 1b) (see Appendix A for photos). Mangataikapua Stream flows from 377 m above sea level at the headwaters to 83 m at the outlet. The study site is mostly confined to a narrow band of weak Early Cretaceous mélange—a highly sheared mudstone in a smectitic matrix associated with the East Coast Allochthon—with the exception of the steep, boundary ridgelines that are composed of a more resistant medium-grained Miocene sandstone (Mazengarb and Speden, 2000) (Figure 1b). The mélange lithology is particularly prone to persistent earthflows, slumps, and gullies, which we will collectively refer to as undifferentiated 'hillslope disturbances' or 'landslides'. Following rapid river incision spurred by the warmer, wetter post-LGM climate, the hillslopes have been responding to down-cutting along the mainstem that oversteepened the lower slopes (Cerovski-Darriau et al., 2014 and referenses therein). Mangataikapua hillslopes near the junction with the Waipaoa River are riddled with active and inactive landslides—evidence of on-going hillslope adjustment to the new

base level—while only ~5% of the 'relict' hillslopes near the headwaters remains unaffected (Figure 1c)**.**

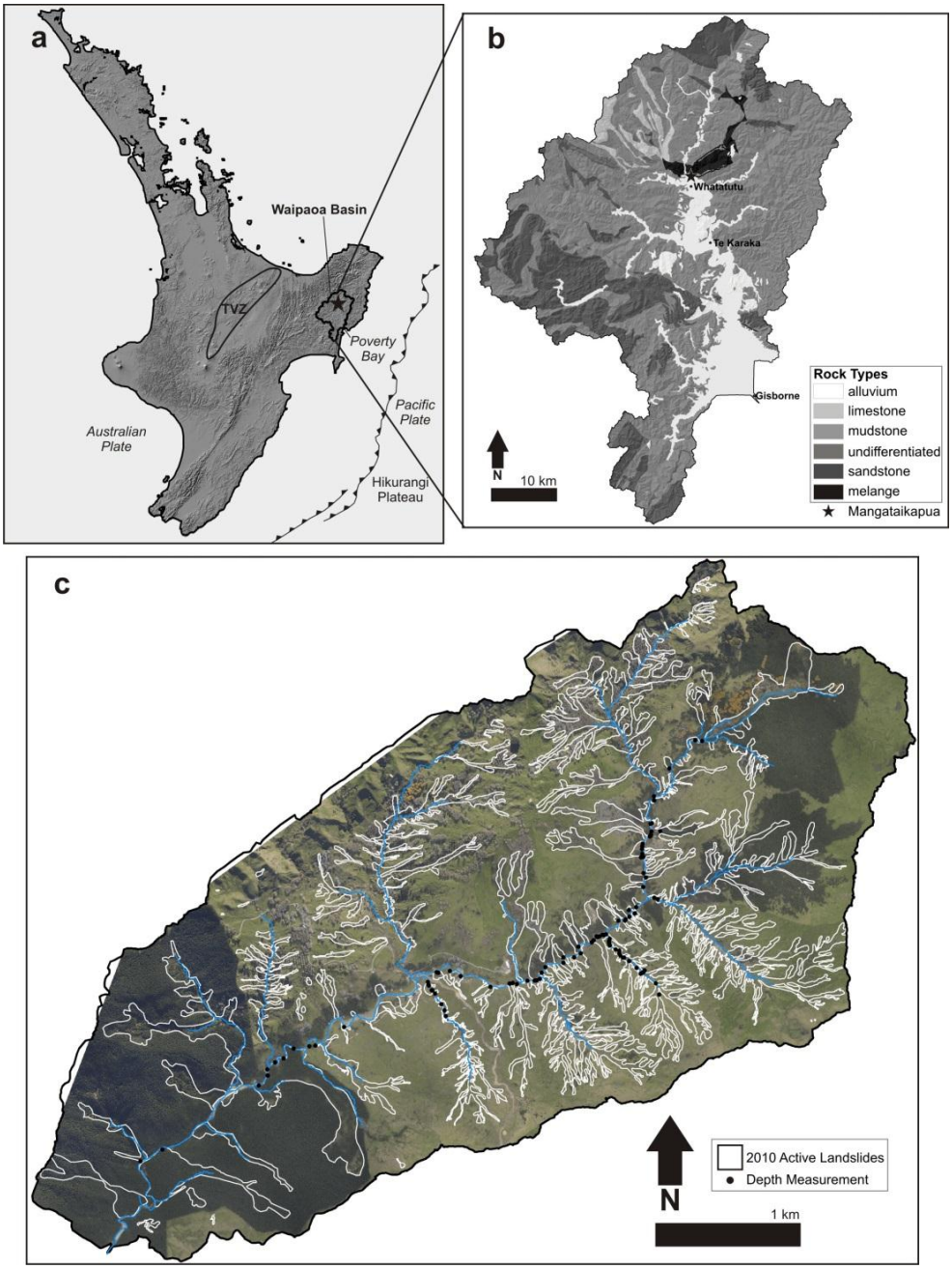

Figure 1. (a) The Waipaoa Basin is located on the East Coast of the North Island, New Zealand. The Mangataikapua study site is marked with the star. The Taupo Volcanic Zone (TVZ) is outlined on the 30 m hillshade. (b) Geologic map of the Waipaoa basin with the mélange band in black. The Mangataikapua catchment, located at the star, is 45 km upstream of Poverty Bay. (c) Mangataikapua catchment (2010 orthophoto) with active landslides outlined in white, and field measurement locations marked as black points.

The mean annual rainfall in the Waipaoa Basin is ~1500 mm, increasing from 1200 mm/yr at the coast to 2500 mm/yr at the headwaters (e.g. Pearce et al., 1987). However, the current climate is highly dependent on the El Niño-Southern Oscillation (ENSO) cycle (established ~4 ka) (Gomez et al., 2004). ENSO cycles follow an irregular 3-7 year cycle of two phases. The El Niño phase tends to cause drought conditions along the eastern coast of New Zealand, while the La Niña phase tends to cause more rainfall and warmer annual temperatures. In addition, the climate is affected by the Interdecadal Pacific Oscillation (IPO), which leads to an increased number of ENSO events in a 15-30 year cycle. Large storms and cyclones occur every ~3 years (Kelliher et al., 1995). Several major flooding events with >200 mm of rain in 72 hrs have taken place since European settlement (Gage and Black, 1979), and have been recorded at the Kanakanaia Bridge gauging station (~15 km downstream of the Mangataikapua) since 1876. Storms are highly variable in the Waipaoa, so discharge rates from Kanakanaia provide a reliable proxy of rainfall (Kelliher et al., 1995).

The Mangataikapua is currently pastureland grazed by sheep with recently planted *pinus radiata* at the outlet from the mid-20th century government-led effort to reforest parts of the Waipaoa. Local areas of poplar and willow are planted in the Mangataikapua as an attempt to slow sediment export from zones with the most egregious erosion. Additionally, native cabbage trees and manuka have regrown sporadically throughout the catchment.

Pre-European settlement, the Mangataikapua was a dense forest of native bush—comprised of ferns, totara, matai, tawa, kowhai, kahikatea, and beech among other species of podocarps and hardwoods (Campbell, 1946; Henderson and Ongley, 1920). Large blocks of land were purchased in the 1870s to 1880s as Europeans began settling the area (Allsop, 1973; Anderson, 2010; Campbell, 1946). These were often cleared by repeated rounds of widespread timber felling, followed by burning for weeks at a time, before they could be split into smaller blocks for sale (Campbell, 1946; Howard, 1976). The recently burned land was seeded with ryegrass, clover, and cocksfoot to feed livestock (Allsop, 1973). Initially, the blocks were heavily overgrazed by a prescribed ratio of cattle to sheep (1:11) to trample any regrowth of native vegetation (Campbell, 1946). Most of the densest forest had been cleared in the neighboring Kanakanaia Valley

by the 1890s (Anderson, 2010), and most of the areas near Whatatutu were cleared by the 1910s (Howard, 1976). Initially the land was quite prosperous—supporting 10-12 sheep/hectare (Allsop, 1973)—but by 1910 settlers noted an increase in erosion, decrease in fertility, and conversion of the Waipaoa River to a soft, boggy bed (Allsop, 1973; Campbell, 1946). In 1920 the immense soil erosion problems were acknowledged in a NZ Geological Survey Bulletin, which warned of the impending landslide danger as the roots of the felled trees decayed in the Poverty Bay area (Henderson and Ongley, 1920).

The Mangataikapua is a useful proxy for the Waipaoa River basin because the geomorphic processes and land-use history are characteristic, but largely confined to a single, particularly weak rock type. This allows us to calculate erosion rates while minimizing effects due to lithologic variation. Additionally, the weak mélange facilitates rapid erosion, enabling change detection over decadal timescales. Therefore our findings have application to the rest of the Waipaoa, even though the rates may not be representative.

3. Methods

3.1. Photo Rectification

New Zealand Air Mapping (NZAM) scanned negatives of aerial photographs from flights surveys spanning the study area in 1956 (1:18000), 1969 (1:24000), 1979 (1:47000), and 1988 (1:25000). We orthorectified and resampled the imagery in ENVI 4.5 using a 2010 airborne lidar hillshade and DEM as a reference, and ground control points selected from stable ridges, fences, buildings and trees. Color orthophotos taken concurrently with the 2010 lidar flight were orthrectified by NZAM.

3.2. Landslide Inventory

Active landslide outlines were digitized using the rectified air photos for 1956, 1969, 1979, 1988, and 2010. We identified landslides as ‘active’ if we observed evidence of movement between the previous or following photos—including translated trees, disrupted ground, clear flowlines, or displaced channels. Active landslides have sharp boundaries and headscarps, which delineated the extent of the outline. We made no distinction between types of landslides (e.g. slumps, deep-seated slides, shallow slides, or

earthflows) or gullies. We mapped all active, large-scale (>4-8 m^2) hillslope disturbances as 'active landslides'.

Initially we classified the images based on the spectral signatures of landslide headscarps, bodies, and toes—assigned using the ArcGIS 10 Image Classification toolbar—for each orthorectified photo set. We used the resulting classified rasters to automatically generate a rough landslide inventory for each photo year. Then, we reviewed each automated outline to verify the landslide was active and, as necessary, manually modified the outline to more accurately delineate the extent of each feature (Figure 1c (2010); Figure 2 (1956-1988 outlines); Figure C1-C4 (1956-1988 photos); see Appendix C for all "C" figures).

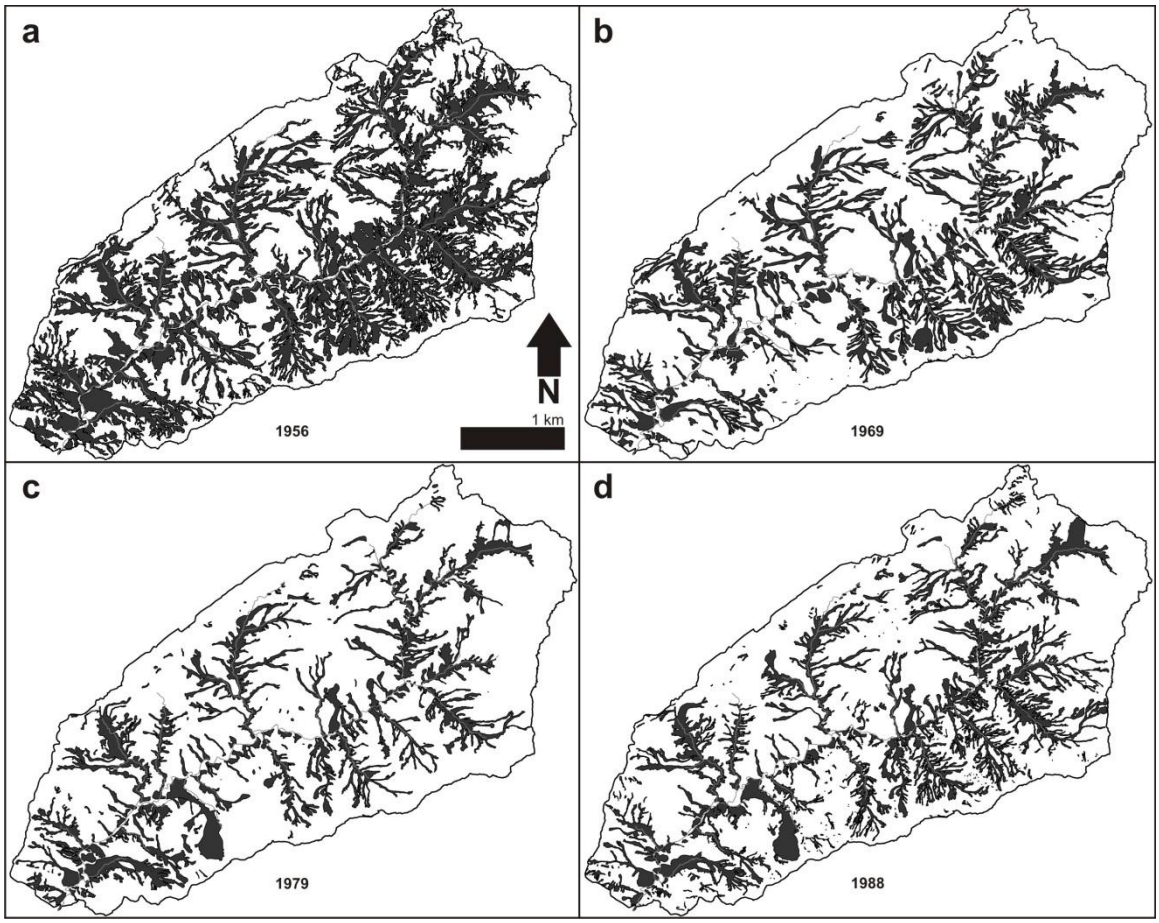

Figure 2. Location of active landslides for each photo year showing the decreasing spatial coverage from (a) 1956 to (c) 1979, and the slight increase in (d) 1988. The corresponding photos used to map these landslides are available in Appendix C (Figure C1-C4).

3.3. 'Turf Index'

In order to determine the sediment flux from each landslide feature, we needed estimates of downslope landslide velocities. Due to the paucity of persistent features (e.g. trees), we were unable to consistently determine the downslope displacement by tracking features between sequential images (e.g. Mackey et al., 2009). Due to the sporadic deforestation and reforestation efforts between photos and the lack of widespread stable features, automated pixel tracking software such as CosiCorr was unable to reliably determine displacements. Instead, we created a 'turf index' to relate downslope velocity to amount of ground disruption.

We identified a small number of trackable features that allowed us to determine that the active landslides could be grouped into three velocity classes, which correspond to the amount of visible ground disruption (Figure 3). Class 1 is the slowest velocity category and consists of landslides with no visible broken ground, but evidence of movement (e.g. translation or expansion between photos, flow lines, levees, etc.). Class 2 consists of a mix of broken ground—or areas of exposed bedrock that appear bright (i.e. higher albedo) compared to the darker ground cover/vegetation—and intact blocks. Class 3 is the fastest velocity category and is associated with disrupted ground supporting little to no vegetation or remaining turf. For each class we measured the displacement of 3 to 6 features, and from those values estimated average velocities to each category (Figure 3; Table C1; see Appendix C for all "C" tables).

For each photo set, we created a spectral signature file by selecting areas from the orthophoto that typify each of the three classes (Figure 3). We then used a maximum likelihood classification in the ArcGIS 10 Image Classification toolbar with equal weighting to assign pixels to the class with the highest probability of being a member. We used a 50% rejection rate to only classify the half of the pixels with the highest probability of similarity.

Then we analyzed the class distribution within each landslide polygon, and selected the most frequent (modal) class as the overall landslide class. We only used pixels within 50 m of the mainstem and tributary channels in order to assign a velocity that was appropriate for the portion of the landslide that is directly contributing sediment to a channel. We chose a 50 m threshold because it was greater than the maximum annual

displacement we found, but still a reasonable distance over which to assume material could contribute to the annual sediment flux.

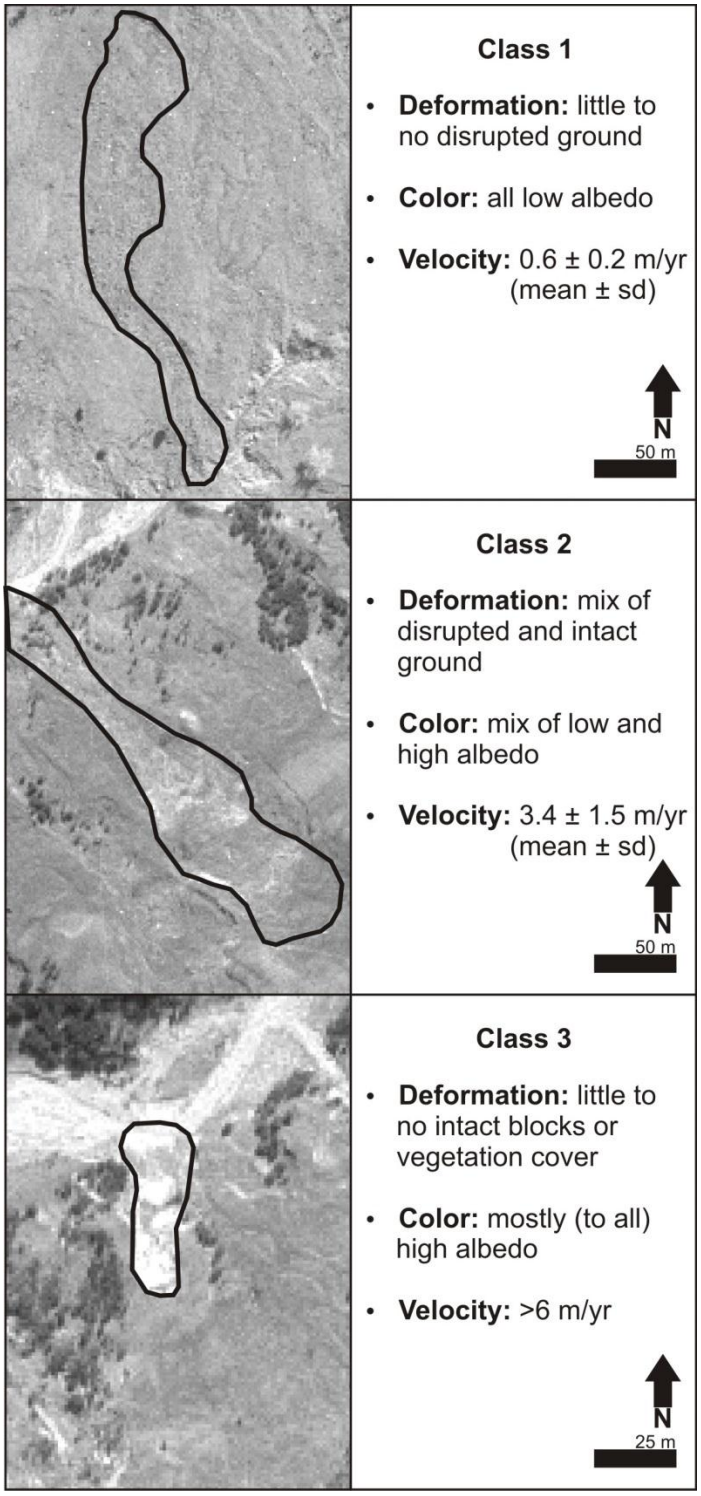

Figure 3. Type examples and criteria for each of the three 'turf index' classifications.

3.4. Landslide Toe Depth

In lieu of measuring the toe thickness of each individual landslide, we determined the average toe depth for the study area based on field measurements of 37 landslide toes that spanned the main channel and two tributaries (Figure 1c). The active landslides tend to have a similar geometry with the exception of a few large landslides near the outlet or the headwaters (e.g. Figure 1c); thus we assume relatively small variability in the proportions and apply an average toe depth catchment-wide. Toe depth was measured from the landslide-channel bank interface to the initial break in slope above the channel using a surveying rod and level. For toes wider than a couple meters, we took multiple depth measurements and used the mean. Additionally, we used a curvature map to determine the toe depths along the main channel to verify our field measurements and validate applying an average depth catchment-wide.

3.5. Vegetation Coverage

We used tree coverage as a proxy for land-use. To compare the temporal variation in sediment flux to land-use changes, we determined the percentage of the study area that was vegetated for each photo set. Following a workflow similar to the landslide inventory, we semi-automated the process by using the ArcGIS Image Classification toolbar to identify the trees in each image. We then modified the automated tree outlines by hand as needed. We determined the total forested area (in % land cover) for each photo year by summing the total area outlined as trees and dividing by the catchment area.

4. Results

4.1. Landslide Velocity and Depth

Using the measured displacements and the corresponding time interval between photos, we determined the velocity for Class 1 (v_1) to be 0.6 ± 0.2 m/yr (mean ± sd), Class 2 (v_2) to be 3.4 ± 1.5 m/yr, and Class 3 (v_2) to be >6 m/yr (Table C1). Class 3 was difficult to estimate due to the nearly complete destruction of turf; therefore, we were only able to determine a minimum amount of downslope movement. The greatest

velocity measured for Class 2 was 5.5 m/yr, thus we assumed that Class 3 velocities will at least be greater than 5.5 m/yr. We measured three Class 3 features, which had velocities of 7 m/yr, 11 m/yr, and 30 m/yr, further supporting this assumption. For the flux calculations, we assigned a 50% standard deviation (± 3 m/yr)—the greatest of all the classes while ensuring $v_3 > v_2$. However, this error is only appropriate for calculating the lower bounds because we have few constraints on the upper bound. From the 37 landslide toes measured in the field, we determined a catchment-averaged depth (d) of 4.4 ± 1.3 m/yr (mean ± sd). The relatively small variance (~30%) validates our assumption that a single average toe depth can be applied catchment-wide. We also obtained a similar average depth from remotely mapping the change in curvature of 59 landslide toes (5.0 ± 2.1 m/yr (mean ± sd)) (Table C2), further validating our field measurements.

4.2. Flux Calculations

To calculate the sediment flux from each landslide to the channel, we used the turf-derived downslope velocity estimates assigned to each polygon combined with the width and average depth of the landslide-channel intersection. Assuming minimal changes in bulk density, the total sediment flux (Q_{sed}) for each photo set was determined as follows:

$$Q_{sed} = \sum_{i=1}^{n} v_{ci} d L_i \quad (1)$$

where v_{ci} is the annual velocity for the class of a given landslide, d is the average landslide toe depth, and L_i is the length of the landslide-channel interface for a given landslide. We assigned a 20% error to L_i to account for potential mapping inaccuracy. From this, we calculated the corresponding catchment-averaged erosion rate (E):

$$E = \frac{Q_{sed}}{A} \quad (2)$$

where A is the catchment area (A=15.9 km^2). Our results demonstrate that the erosion rate decreased through time, with erosion rates of 29.9 ± 12.9 mm/yr (mean ± sd) in 1956,

28.8 ± 13.7 mm/yr in 1969, and 13.4 ± 4.9 mm/yr in 1979. In 1988 there was a slight increase to 17.0 ± 6.2 mm/yr, but the rate decreased to the lowest calculated rate, 9.9 ± 3.6 mm/yr, by 2010 (Table 1; Figure 4a).

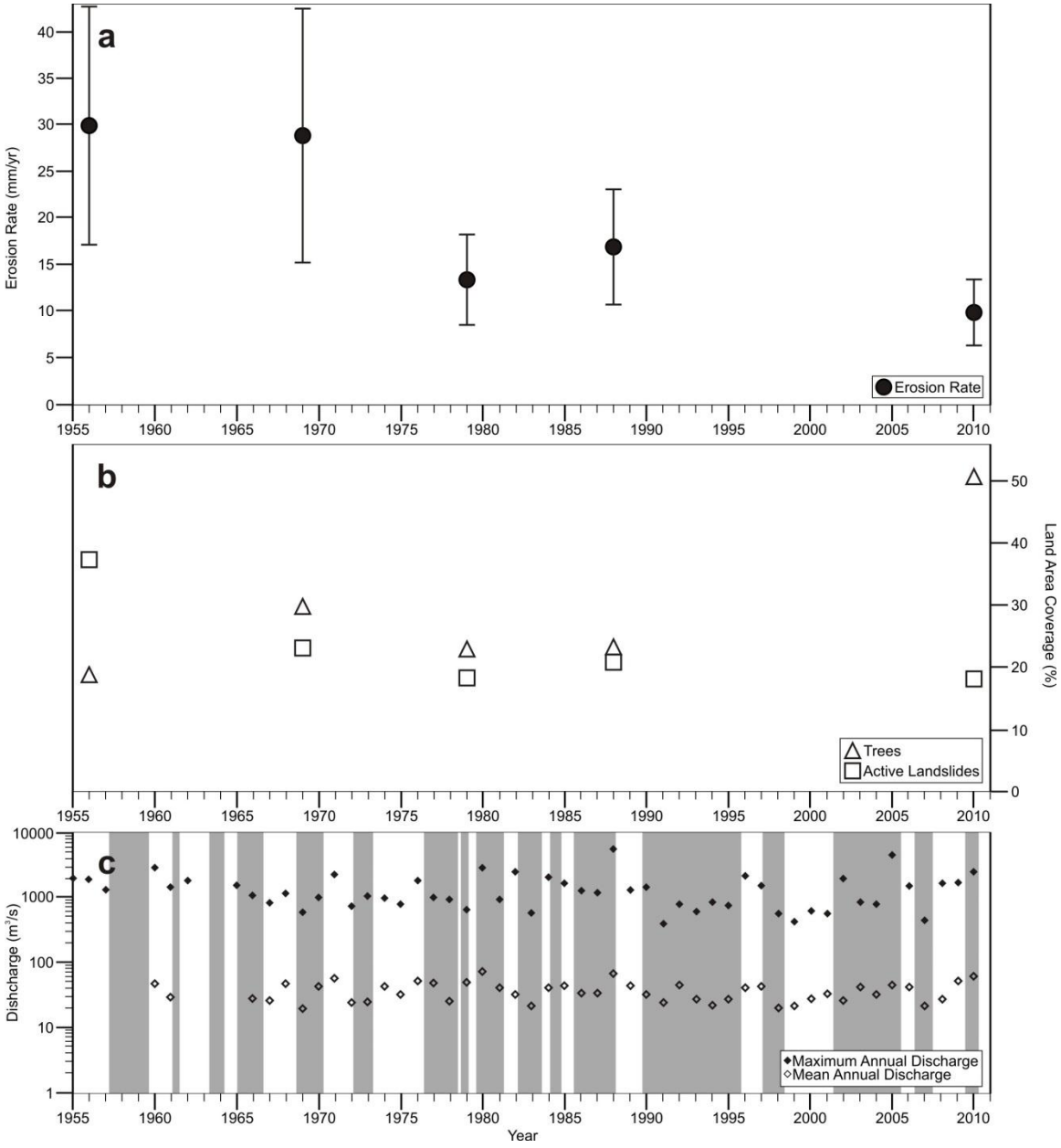

Figure 4. (a) Erosion rates determined from the calculated annual sediment flux for each photo year. Error bars span 1 standard deviation. (b) Total spatial coverage (in % catchment area) of trees (triangles) and active landslides (squares) for each photo year. (c) Maximum (solid diamonds) and mean (clear diamonds) annual discharge from the Kanakanaia gauging station at Te Karaka (~15 km downstream from the Mangataikapua). Grey bars highlight the El Niño, or 'dry', El Niño-Southern Oscillation (ENSO) cycles.

4.3. Spatial Coverage

Based on the areal extent of landslides, we determined the proportion of the landscape undergoing active sliding at any one time. Specifically, we found landslide activity decreased with time from 37.3% to 18.1% over the 1956 to 2010 period, with the exception of 1988, where there was a slight increase to 20.9% (Table 1; Figure 4b). The inverse was generally true for vegetation coverage. We found the forested proportion of the catchment increased with time from 18.6% to 50.4% with one exception, 1969 (Table 1; Figure 4b).

Table 1. Erosion rates, landslide area, and vegetation area

Year	**Erosion** (mm/yr)	**Std Dev** (mm/yr)	**Landslide Area** (%)	**Vegetation Area** (%)
1956	29.9	12.9	37.3	18.6
1969	28.8	13.7	23.1	29.5
1979	13.4	4.9	18.3	22.6
1988	17.0	6.2	20.9	23.0
2010	9.9	3.6	18.1	50.4

5. Discussion

Most generally, we observed that erosion rates are inversely correlated to vegetation cover and roughly proportional to the percentage of active landslides (Figure 4). As expected, interdecadal variability is superimposed on those trends, likely due to changing vegetation, climatic variations, large storms, or other external factors such as grazing practices. However, regardless of any interdecadal variability, our calculated erosion rates decrease to a minimum (~10 mm/yr) by 2010. Notably, this value is an order of magnitude greater than the long-term (post-LGM or longer) erosion rates, implying that the landscape response to intense anthropogenic land-use modification continues at an elevated pace for more than a century.

The Mangataikapua has been a rapidly eroding tributary catchment of the Waipaoa for at least the past 18 kys. Previously, Cerovski-Darriau et al. (2014) determined the post-LGM catchment-averaged erosion rates for the Mangataikapua to be 1.6 mm/yr—double the Waipaoa average of 0.8 mm/yr (Bilderback et al., 2015). Initially

erosion rates were as high as 2.3 mm/yr, but decreased to 0.7 mm/yr by 3.4 ka (Cerovski-Darriau et al., 2014), equivalent to the long-term uplift rate determined from pairs of Quaternary fluvial terraces in the central Waipaoa (0.5-0.9 mm/yr) and Late Tertiary mudstone burial depths at the Mangataikapua outlet (0.7 mm/yr) (Berryman et al., 2000; Litchfield and Berryman, 2006). However, between 0-3.4 ka, Cerovski-Darriau et al. (2014) showed that erosion rates increased to 2.2 mm/yr and hypothesized that the increase reflected anthropogenic land-use change over the past 100-200 years. To test this we assume that before widespread human intervention the erosion rate was 0.7 mm/yr, then apply our new average erosion rate since Europeans settlement began in 1870 (~20 mm/yr), and arrive at an updated catchment-averaged erosion rate of 1.5 mm/yr for the past 3.4 kys. This updated 'anthropogenic' erosion rate should likely be even higher because our post-European erosion rate is only averaged over the past ~50 years, when reforestation and soil conservation efforts likely slowed erosion rates compared to preceding ~50 years. By comparison, the anthropogenic erosion rate—averaged over just the past ~50 years—is an order of magnitude greater than the post-LGM rate in both the Mangataikapua and the overall Waipaoa. An even higher anthropogenic average would further support that, in just over a century, humans have had a profound influence on the long-term records.

Our observed decrease in catchment-averaged erosion rates since the 1950s is consistent with what previous studies found for gullies and shallow landslides in the Waipaoa (DeRose and Gomez, 1998; Gomez et al., 2003; Marden et al., 2005; Reid and Page, 2002). For the entire Waipaoa, Marden et al., (2014) determined that hillslope erosion rates decreased by 50% between 1960 and 1988. Similarly, we found a 40% decrease between those same time periods. However Marden et al.'s (2014) peak basin-averaged erosion rate was only ~14 mm/yr—half that of the Mangataikapua (~30 mm/yr)—further evidence that the weak mélange lithology makes our study site a fast-paced microcosm of the Waipaoa Basin.

With our dataset, we are able to capture interdecadal trends, but remain unable to determine causal factors for specific annual variability without additional photos and data (e.g. rainfall, land-used, etc.) from the intervening years. For example, in 1969, despite a nearly 60% increase in vegetation cover since 1958, the erosion rate only decreased by

~4%. This was likely due to more fast-moving landslides (i.e. Class 3) (Figure C5), but we have insufficient intradecadal data to determine the cause of increased landslide velocity during a specific year. Despite the interdecadal variability in the point measurements, we find the overall decrease in erosion to be >90% significant (P=0.06)—and we posit this reflects anthropogenic vegetation change. Although we determined that erosion is slowing, we also show that the rate remains an order of magnitude greater than the background erosion rate emphasizing the century-long legacy effect of humans on the landscape.

But why did humans have such an impact? We argue that a combination of the existing geology, loss of vegetation, and manner of land clearance caused these massive scale erosion problems that continue to impact the Poverty Bay region.

Lithologically, the weak marine mudstones and sandstones that make up the Waipaoa bedrock have long been prone to landslides (e.g. Bilderback et al., 2014; Gage and Black, 1979; Page and Lukovic, 2011), and the highly sheared argillite mélange in the Mangataikapua promotes accelerated hillslope erosion and increased landslide density compared to the rest of Waipaoa (Cerovski-Darriau et al., 2014). However, the number and frequency have markedly increased since European arrival (Crozier and Pillans, 1991; Gage and Black, 1979; Henderson and Ongley, 1920), which suggests a strong correlation with land-use change.

From a mechanistic standpoint, the loss of vegetation can affect both soil cohesion and hillslope hydrology. Mechanical cohesion, and thus resistance to erosion, is increased by root reinforcement (e.g. Pearce et al., 1987; Preston and Crozier, 1999; Roering et al., 2003; Sidle, 1991; Zhang et al., 1993). Roots stabilize the hillslopes by mechanically adding shear strength to the soil and physically restraining soil particles (Gray and Sotir, 1996; Greenway, 1987; Schmidt et al., 2001). After timber harvest or burning, the mechanical cohesion remained unchanged for several years until the roots decayed (Campbell, 1946; Henderson and Ongley, 1920; Schmidt et al., 2001; Shakesby and Doerr, 2006). Once the roots were absent, soil consolidation decreased infiltration, thus increasing surface runoff. A study in similar soil south of Poverty Bay found infiltration rates reduced by an order of magnitude from ~100 mm/hr to ~10 mm/hr in the decades after clearance (Campbell, 1946). With decreased infiltration capacity, soil

erosion—particularly processes driven by overland flow and surface wash—tend to increase (Dietrich et al., 2003; Horton, 1945; Howard, 1994). In the Waipaoa, historic accounts report an increase in gullies and surface wash starting in the early 1900s—approximately two decades after the initial period of felling (Campbell, 1946; Henderson and Ongley, 1920).

Hillslope hydrology was also impacted by the loss of vegetation as the pathways and storage capacity of the soil depend on vegetation type (e.g. Istanbulluoglu and Bras, 2006; Zhang et al., 2001). Under forested conditions, evapotranspiration is higher (e.g. Zhang et al., 1993)—decreasing the likelihood of surface erosion—and soil moisture is less variable (Henderson and Ongley, 1920; Pearce et al., 1987). Additionally, in a forested environment, canopy cover decreases the number of raindrops impacting the soil (i.e. decreasing rainsplash erosion) and the volume of precipitation reaching the soil. In pasturelands, the lack of canopy cover promotes drying of the soil, which is particularly dramatic in the clay-rich soils of the Mangataikapua. The high activity bentonite clays have a large shrink-swell capacity, which results in deep cracks and macropores that provide direct pathways to the bedrock-soil interface (Allsop, 1973; Beven and Germann, 1982; Iverson and Major, 1987; Zhang et al., 1993).

While deforestation and promotion of grazing were clearly detrimental to soil stability in our study area, the method of land clearance affected erosion rates as well. The European settlers employed rapid, wholesale felling of native bush followed by repeated large burns (Allsop, 1973; Campbell, 1946). This resulted in large swaths of land synchronously deforested, allowing any localized instabilities to propagate unchecked (Allsop, 1973). Additionally, burns often change soil properties—especially in the cases of large, hot fires (Shakesby and Doerr, 2006). Post-fire soils can be hydrophobic, further promoting surface runoff, creation of rills, etc. (e.g. Shakesby and Doerr, 2006). The slash-and-burn clearance was followed by overgrazing to quell the return of native vegetation (Allsop, 1973). Overgrazing likely accelerated soil compaction, thus accelerating the loss of infiltration capacity, as is the case in other areas of overgrazing (e.g. Hamza and Anderson, 2005; Willatt and Pullar, 1985). Initially the land was productive enough to support 10-12 sheep per hectare, but by 1917, shee density was already reduced to 5 sheep per hectare (Allsop, 1973; Henderson and Ongley, 1920).

Comparing our observed erosion rates to mean annual discharge for the Waipaoa, which is largely driven by ENSO cycles, we see no obvious decadal trends that coincide with our data (Figure 4c)—implying that climatic fluctuations and storms are unlikely to be the primary driver of increased erosion. While our sampling interval is too coarse to resolve any intradecadal fluctuations, the linear decrease in erosion is contrary to a cyclical climatic driver. Additionally, we find little correlation when comparing erosion to maximum annual discharge (Figure 4c)—our proxy for large storms. The one possible exception is Cyclone Bola in March 1988. There is a slight increase in our erosion rates and active landslide area in 1988, which we attribute to the storm. However, it was not a significant change compared to the overall decrease.

Interestingly, the 1988 Cyclone Bola triggered numerous shallow landslides that devastated neighboring catchments, while only marginally affecting the Mangataikapua. We speculate that this is due mainly to the style of landsliding favored by the mélange lithology. Many of the landslide complexes in the Mangataikapua are dominated by earthflows—deep, slow-moving, long-lasting features that form in clay-rich soils in Mediterranean climates (e.g. Kelsey, 1978). These features are less sensitive to individual storms and instead respond to seasonal changes in rainfall (Handwerger et al., 2013 and references therein). Therefore, a single large event (e.g. Bola) may slightly accelerate the features, but otherwise have little effect. While we do see more shallow landslides in the 1988 imagery that are not apparent in the 2010 imagery—and thus attributed to Cyclone Bola—these shallow landslides account for <1% of the total landslide area in the Mangataikapua that year.

Our earliest photo coverage coincides with the beginning of soil conservation efforts in the Poverty Bay region, and our results conclusively show a three-fold decrease in erosion over the following decades. Therefore, despite continued elevated erosion rates a century after the European settlement, we show that erosion is slowing and provide evidence that soil conservation efforts seem to ameliorate the problem. In the 1950s, the newly created Poverty Bay Catchment Board developed a major flood control and soil conservation scheme that led to dedicated reforestation studies in the Te Weraroa catchment—approximately 10 km upstream from the Mangataikapua—and ultimately a government-led concentrated reforestation effort in the Waipaoa headwaters (Allsop,

1973). The Mangatu Forest was planted in the headwaters from the 1960-1970s, and the outlet of the Mangataikapua was reforested in the 1980-1990s. However, while reforestation has promising results (e.g. Gomez et al., 2003; Marden, 2012; Marden et al., 2014), the efforts are only successful where the trees have sufficient time to take root (Allsop, 1973; Marden et al., 2005). Even fast growing poplars, willows, and pine are sometimes unable to become established given the extent and vigor of active landslides in our study area (Te Hau Station Manager, pers. comm.). As evident from the Class 3 turf, once the landslides are moving faster than 3-6 m/yr there is little soil left to support the vegetation and the movement will topple or bury any saplings before they have a chance to take hold (Allsop, 1973; Zhang et al., 1993). Therefore, continued replanting of areas, especially the headwaters and Class 2 areas will aid in continuing to slow erosion and preventing existing gullies from becoming persistent erosional hotspots (Marden, 2012; Marden et al., 2005).

In the Mangataikapua, it took ~10 kys for the hillslopes to adjust to post-LGM climatic changes and for erosion rates to re-equilibrate with long-term uplift rates (~0.7 mm/yr) (Berryman et al., 2000; Cerovski-Darriau et al., 2014; Litchfield and Berryman, 2006). However, with an average post-settlement erosion rate ≥20 mm/yr, we expect a faster hillslope response than post-LGM. Based on previous studies that modeled hillslope response to various erosion rates (e.g. Hurst et al., 2012; Roering et al., 2001), increasing the denudation rate by an order of magnitude decreases the timescale of hillslope response by at least an order of magnitude—assuming the parameters related to hillslope adjustment (e.g. climate, rock erodibility, hillslope length, etc.) are similar to those post-LGM. Reforestation and soil conservation efforts are decreasing erosion rates, though, making it hard to better predict the response time. At rates ≥20 mm/yr, soil loss far exceeds average soil production rates (~0.2 mm/yr), meaning the soil is stripped to bedrock in a matter of years coincident with historic accounts (Henderson and Ongley, 1920; Montgomery, 2007). Here we determined that only ≤37% of the hillslopes are actively adjusting via landsliding during any one year (Figure 4c), despite previous evidence that >99% of the terrain is covered by post-LGM landslides (Cerovski-Darriau et al., 2014). This means that our catchment averaged erosion rates are likely sourced from <50% of the landscape, and that these landslide complexes have migrated through

time to erode almost every locale on the landscape with a sufficient pause between activity and dormancy to allow sediment to accumulate. Even across the ~50 year span of this study, we begin to see the spatial variability of landslides as they coalesce downslope and migrate upstream—evidence of hillslopes actively adjusting to the human-induced perturbation.

6. Conclusion

Using a series of historic aerial photographs from 1956-2010, we tracked the decadal response of the Mangataikapua catchment to anthropogenic land-use change. The wholesale deforestation and initiation of grazing by the European settlers from the 1870s to 1910s has had lasting implications for the landscape—causing rapid erosion and hillslope adjustment that is likely to continue for decades to come. The once relatively stable landscape is now riddled with landslide complexes and gullies due to the loss of stabilizing roots and the increase of surface runoff under pasture. To quantify the effect of this anthropogenic-driven perturbation, we determined a method to infer downslope velocities based on the spectral signature of the landslide. We combined those velocities with 1) landslide toe thickness measured in the field, and 2) landslide-channel interface lengths calculated from the photos to determine the sediment flux for each photo year. The maximum erosion rate (29.9 mm/yr) was from 1956, and then the rate decreased three-fold to the minimum rate (9.9 mm/yr) by 2010. The average erosion rate over our ~50 year study period was ~20 mm/yr, which is an order of magnitude greater than the previously determined post-LGM erosion rate. This century-long perturbation has skewed erosion measurements when averaged over the past few thousand years—likely causing overestimates by a factor of 2-3. While this is not enough to skew the longer-term post-LGM rates, the impact of concentrated human disturbance on the catchment is still readily apparent ~100 years after deforestation. Humans are effective geomorphic agents, managing to perturb the entire Waipaoa Basin after only a few decades—a perturbation that continues to drive widespread hillslope adjustment and elevated erosion rates over a century later.

7. Bridge

In this chapter (Chapter III), I used aerial photos from 1956-2010 and lidar to map landslides and infer their downslope velocities. From this information, I was able to calculate historic erosion rates for the Mangataikapua and relate these elevated rates to anthropogenic land-use change that began in the late 1800s. Comparing this information to the previous chapter (Chapter II), I was able to analyze longer-term (post-LGM), climate-driven and shorter-term (historic), human-driven landscape evolution via landslides.

In the following chapter (Chapter IV), I will again analyze landslides that are potentially significant contributors to the regional sediment flux over the longer-term, geologic timescales, but also potentially hazardous to humans over the shorter-term, earthquake cycles. In Chapter IV, however, I will verify a geophysical method for quantifying landslide depth rather than complete a catchment-wide sediment budget study like I did in Chapters II and III. In particular, I will compare geologic and geomorphic data to seismic refraction results from two landslides in the Oregon Coast Range located in western Oregon, USA. Therefore, in the following chapter, I will expand my research to a different field area dominated by different types of landslides and utilize a different tool, but still motivate it by the same theme: the role of landslides in landscape evolution over disparate timescales.

CHAPTER IV

UTILITY OF SEISMIC REFRACTION FOR CHARACTERIZING DEEP-SEATED LANDSLIDES IN WESTERN OREGON, USA

In preparation for submission to *Engineering Geology* as co-authored material with Jered L. Hogansen, Douglas R. Toomey, Joshua J. Roering, and Miles A. Bodmer. The article present results from: 1) geomorphological fieldwork conducted by me, 2) geophysical fieldwork conducted by D. R. Toomey, M. A. Bodmer, J. L. Hogansen, and me, 3) geophysical analyses completed by M. A. Bodmer and J. L. Hogansen (with input from D. R. Toomey), and 4) geomorphological analyses and comparisons with the geophysical data done entirely by me (with input from J. J. Roering). I synthesized the data, created the figures, and wrote the text with feedback and editorial assistance from J. J. Roering and D. R. Toomey.

1. Introduction

Large landslides can affect landscape morphology for thousands to millions of years (e.g. Roering et al., 2005; Korup, 2006; Booth et al., 2013; Haugerud, 2014) as well as cause an immediate direct and indirect hazards to humans by destroying property and infrastructure, damming rivers and causing upstream inundation or downstream outburst floods, or interrupting the flow of goods and services (e.g. Kargel et al., 2015; Olsen et al., 2015). Quantifying the role of large landslides in long-term landscape evolution and the short-term hazard requires understanding the geometry, movement style or frequency, and failure mechanisms of these features. However, because few landslides are monitored during a failure, most of these unknowns require using previously failed landslide to make generalizations about the likelihood and style of future landslides. Moreover, most subsurface information has to be inferred based on the surface morphology. Because of the expense of subsurface investigations, only occasionally are they completed, and typically consist of boreholes or trenches to get only localized subsurface information.

In the past few decades, geophysical techniques (e.g. refraction, reflection, resistivity, or ground penetrating radar) are increasingly being used to get more

comprehensive subsurface landslide information (Jongmans and Garambois, 2007). These methods have the potential to be a relatively quick and easy way to characterize the subsurface and seem to be producing good results (e.g. Jongmans and Garambois, 2007; Schrott and Sass, 2008; Rumpf et al., 2012). Rarely, though, is there an opportunity to validate the results in the field as they are usually chosen in lieu of costly boreholes, or only compared to a few exploratory logs.

In the Oregon Coast Range (OCR), characterizing the deep-seated landslides—or landslides with failure planes several to tens of meters below the surface that include both soil and bedrock—is of utmost importance to understand the potential hazard posed during the next Cascadia Subduction Zone (CSZ) earthquake. The CSZ has generated great earthquakes (M_w 8-9) every ~500 years in the past and potentially will again in the future—the last being a M_w ~9 in 1700 (e.g. Petersen et al., 2002; Goldfinger et al., 2003; Witter et al., 2003). Earthquakes are known to initiate large, deep-seated landslides (e.g. 1994 Northridge (Harp and Jibson, 1996), 2008 Wenchuan (Huang and Fan, 2013), and 2011 Tohoku (Wartman et al., 2013), and 2015 Gorkha (Kargel et al., 2015)), and have been speculated upon for Cascadia (Baldwin, 1958; Lane, 1987; Roering et al., 2005; Morey et al., 2011; Schulz et al., 2012). An examination of lidar data demonstrates that many of these landslides have experienced multiple failure episodes and several show morphological evidence of recent reactivation. These deep-seated landslides likely fail as dip-slope failures along the shallow bedding planes in the Tyee Formation. The OCR is predominantly underlain by the Tyee Formation, which is a minimally deformed Eocene marine sedimentary unit of alternating massively bedded (1-3 m) turbiditic sandstone units with thin interbeds (cm) of siltstone (Snavely et al., 1964; Heller and Dickinson, 1985), with failures concentrated along the weaker siltstone layers (Roering et al., 2005).

Thousands of these large, deep-seated landslide deposits have been identified in the OCR (Figure 1). Yet historic activity of these features is ominously rare, causing them to be often overlooked in decades of OCR geomorphic research, and suggesting that the CSZ earthquakes may regulate their activity. From a public planning perspective, having a better depth constraint on a few of these landslide deposits will lead to improved calculations of slope stability in order to more accurately model what lifelines and urban zones are at risk. From a geomorphic prospective, depth constraints facilitates

constructing an OCR-specific landslide depth-area scaling relationship (e.g. Larsen et al., 2010), which can be extrapolated to determine the total volume of material displaced by deep-seated landslides in the OCR—a pervasive process that has been ignored and could challenge the current understanding of OCR landscape evolution. For either application, geophysical techniques—like refraction surveys—seem like a promising method for characterizing landslides (Jongmans and Garambois, 2007 and references therein; Schrott and Sass, 2008) and tackling some of these unknowns in OCR hazard-planning and geomorphology.

While the seismic refraction methodology is well-established, the application to landslides and other geomorphic problems is still relatively new and accompanying physical data is seldom available—thus comprehensive studies to validate the results with physical data are rarely feasible or completed. Geophysical methods are likely to become even more widespread in geomorphology as their utility and accuracy in answering questions about the subsurface morphology and material properties becomes better understood (e.g. Schrott and Sass, 2008; St. Clair et al., 2015; West et al., 2015). Therefore, here we test the accuracy of a refraction survey for predicting the location of landslide failure planes in a heavily forested and intensely managed landscape.

Here we have the unique opportunity to compare two seismic refraction surveys to subsurface (borehole and auger) data as well as additional geophysical data. We performed a refraction transect across two deep-seated landslide in the OCR to image the loose colluvium of the landslide deposit and the underlying dense bedrock. We tested the accuracy of the first transects by comparing the results to 29 failure plane depths derived from existing borehole and slope inclinometer data. The second transect was compared to a borehole we hand-augered as well as previously collected passive seismic array that can be used to infer the thickness of the landslide at the seismometer location.

2. Study Area

2.1. Oregon Coast Range (OCR)

The OCR is one of the best-studied geomorphic landscapes in the world (e.g. Dietrich et al., 2003). It is a temperate, humid, soil-mantled landscape with dense coniferous forest planted for timber underlain by the rhythmically bedded turbidites of

the Tyee Formation. The Tyee turbidites were deposited offshore in the early Eocene and are generally laterally homogenous, but individual bed thickness and the ratio of sandstone to siltstone varies latiduinally—with thinner beds and a lower sandstone:siltstone ratio farther north (Heller and Dickinson, 1985). The Tyee was gently folded to a dip angle of <20° in the late Eocene and uplifted beginning in the Miocene to form the OCR, and the OCR continues to be uplifted and eroded today (Roering et al., 2005 and references therein). The OCR is thought to be a classic example of a steady-state landscape where erosion by seasonal shallow landslides and debris flows balance rock uplift (e.g. Reneau and Dietrich, 1991; Benda and Dunne, 1997; Roering et al., 2001; Stock and Dietrich, 2003). However, in the OCR, the role of pervasive large bedrock failures in landscape evolution has been ignored, potentially challenging this paradigm. The OCR was thought to be characterized by steep and dissected 'ridge-and-valley' topography dominated by debris flows, but the prevalence of high-resolution topographic data now reveals that low-gradient, planar deep-seated landslides are ubiquitous across the OCR (Roering et al., 2005) (Figure 1). However, there have been few historical failures, which leads to speculation as to what triggers these large landslides and what controls their distribution (e.g. Baldwin, 1958; Lane, 1987; Roering et al., 2005; Schulz et al., 2012). Structure and lithology likely exert at least a primary control on the distribution of these deep-seated landslides, with a higher probability of occurrence: 1) along more inclined bedding planes, and 2) farther north where the weaker, siltstone layers are thicker and more frequent (Roering et al., 2005). However, beyond these first-order controls on the distribution, little is known about these deep-seated landslides.

2.2. Cougar Creek

The Cougar Creek landslide is located along the Yaquina River in the central OCR, near the eastern extent of the Tyee formation, about 20 km east of Newport, OR (44.65, -123.82) (Figure 1; Figure 2a). The landslide is bisected by the proposed US Highway 20 realignment project, and has reactivated during construction. The landslide is approximately 500 m wide and 600-1000 m long. Based on a radiocarbon sample from the toe, the landslide likely failed 38.83 ± 0.38 ka (Hammond et al., 2009). Most of the

landslide was logged and much of the surface re-worked in preparation for the highway construction. Large piles of fill for a bridge span are currently on top of the landslide deposit. Oregon Department of Transportation (ODOT) and the consultants tasked with stabilizing the landslide drilled exploratory boreholes and installed piezometers to measure groundwater and slope inclinometers to measure subsurface displacement across the landslide.

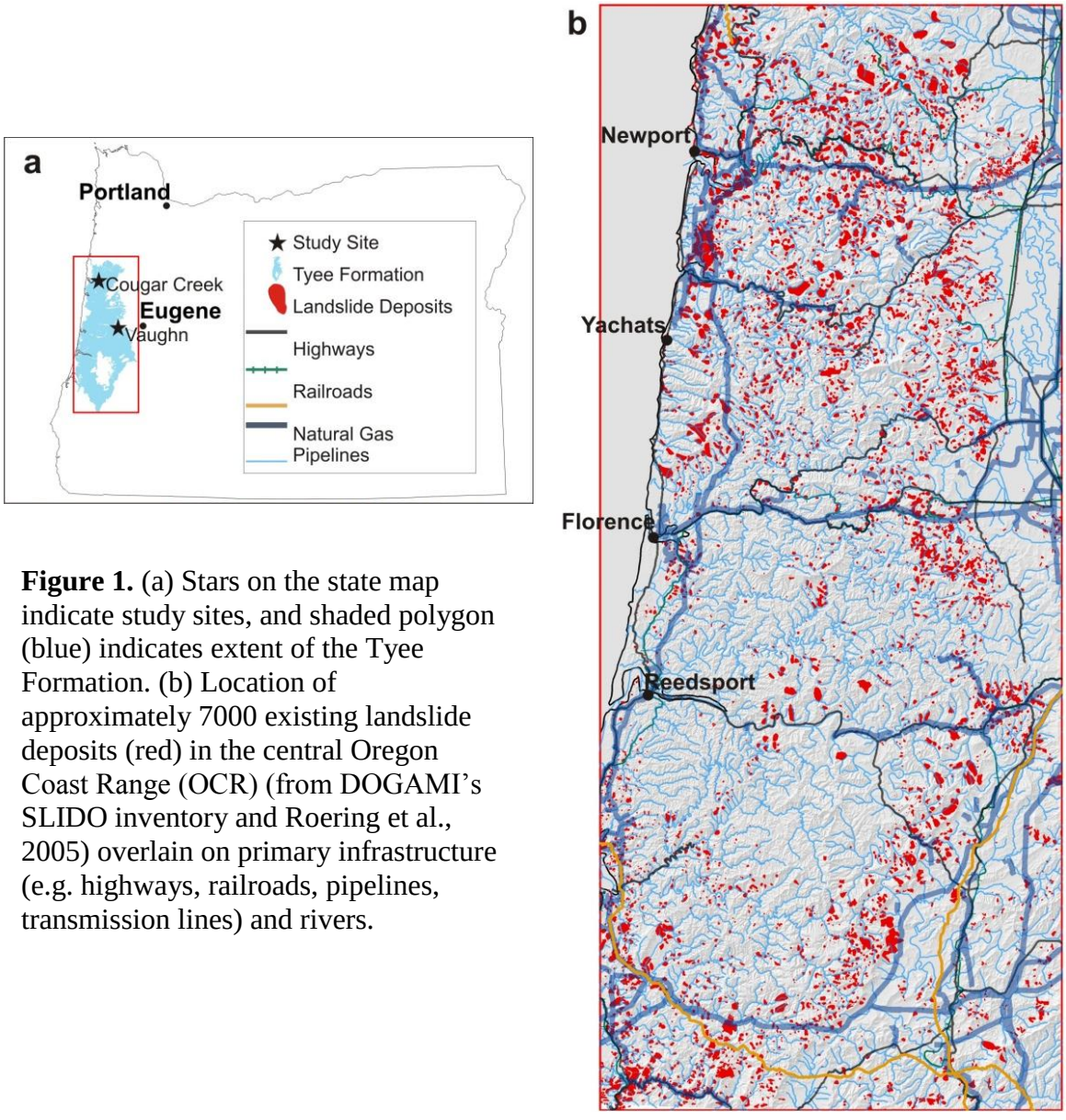

Figure 1. (a) Stars on the state map indicate study sites, and shaded polygon (blue) indicates extent of the Tyee Formation. (b) Location of approximately 7000 existing landslide deposits (red) in the central Oregon Coast Range (OCR) (from DOGAMI's SLIDO inventory and Roering et al., 2005) overlain on primary infrastructure (e.g. highways, railroads, pipelines, transmission lines) and rivers.

2.3. Vaughn

The Vaughn landslide is located in the central OCR, near the eastern extent of the Tyee formation, about 30 km west of Eugene, OR (44.01, -123.49) (Figure 1; Figure 2b).

It does not appear to be currently active, but is a relataively more recent reactivation (approximately 400 m wide and 600 m long) within a larger, older landslide complex. Based on soil spectroscopy of the hematite oxidation, the landslide complex is ~100 kys old (Sweeney et al., 2012; Mathabane et al., 2013). The whole complex is on timber land that was most recently logged and re-planted ~10-20 years ago.

3. Theory

Shallow seismic refraction is used to determine the depth to near-surface layers and the velocity within these layers. By recording the first arrivals of seismic energy as waves are refracted off a higher velocity layer back to the surface, we can determine the refraction angle and thus the velocity of the layer based on Snell's Law (Kearey et al., 2002; Schrott and Sass, 2008). Seismic refraction is widely used in engineering and oil exploration to characterize the shallow subsurface geology and identify depth to bedrock. This technique is appealing for landslide investigations because of the sharp velocity contrast between the looser landslide colluvium and the underlying, denser bedrock should provide a distinct refractor. Therefore, this velocity contrast is captured when the refracted P-waves are recorded by a seismometer, and these first arrivals can be inverted to infer the depth to the velocity contrast—i.e. base of the landslide deposit. There are several inversion techniques to interpret first arrivals depending on the quality of the data and intended use (Jongmans and Garambois, 2007 and references therein). Here we use a simple layer-based time-term inversion to get general velocities and depths instead of a detailed model of the refractor.

4. Methods

4.1. Refraction Survey

4.1.1. Experiment Design and Data Acquisition

We collected refraction data with a Geode: Ultra-Light Exploration Seismograph system by Geometrics from IRIS PASSCAL. The system consisted of a field computer, two 24-channel cables with 5 m takeout, 48 vertical component geophones, and two Geode seismographs. Due to dense vegetation and steep topography, the geophones were deployed along a gravel road that transected the landslide. We used a truck-mounted

Elastic Wave Generator (or a 'slingshot') and a striker plate as the active seismic source. The packed gravel road provided good coupling between the source and the ground. We recorded the GPS location of each geophone and 'shot' with a handheld Trimble GeoXH at Vaughn and a Leica Total Station at Cougar Creek. For Vaughn, we initially chose 5 m geophone spacing and a synthetic aperture design to make a 480 m lateral spread in order to achieve 100 m of vertical penetration. For Cougar Creek, we decreased the spacing to 2.5 m because we anticipated the landslide was <100 m thick. With 2.5 m spacing, we decreased the overall penetration depth, but increased the vertical resolution. For both experiments the active source shot spacing was 30 m, and we stacked 8 shots at each source location to increase the signal to noise ratio. For all surveys we used a sampling interval of 0.25 ms and a Nyquist frequency of 200 Hz.

4.1.2. Data Processing

We processed the refraction data using the two dimensional SeisImager 2/D by Geometrics. We used the PICKWIN module to plot the seismic records and select the P-wave first arrivals. PICKWIN uses those picks to create travel-time curves that are input into the PLOTREFRA module to generate a 2D velocity model. We used time-term inversion method—a linear least-squares and time delay inversion—to generate various two- and three-layer P-wave velocity models for each experiment based on slope changes in the travel-time curves. We verified the precision of the time-term inversions using raytracing to compare synthetic travel-times to our inversion models. These models produce a velocity structure of the shallow subsurface that differentiates the low and high velocity zones that likely correspond to the loose landslide deposit and the denser underlying bedrock.

4.2. Borehole Data

We obtained subsurface geological data from 39 boreholes previously acquired by ODOT and Cornforth Consultants across Cougar Creek. We compiled the borehole logs and photographs obtained from ODOT and Cornforth, and recorded the depth of any lithologic, color, or texture change and landslide features (e.g. slickensides, polished surfaces, etc.) noted in the logs. We used the transition from orange/brown highly

weathered colluvium to gray intact interbedded siltstone/sandstone as the base of the landslide deposit. We used stiff clay and/or prevalent slickensides noted in this transition zone as indication of failure surfaces. In addition, where slope inclinometer data was available, we were able to determine the depth and deformation style of the current failure surface or interface. We eliminated boreholes that did not reach unweathered bedrock or were off the ends of the refraction survey. Ultimately we had basal landslide depths from 18 boreholes and 11 slope inclinometers that span the length of the refraction line—from 21 m upslope to 107 m downslope (Figure 2a) (Table D1; see Appendix D for all "D" tables). We plotted those points in Matlab and fit a plane to those 29 points using a first-order polynomial to approximate the failure interface. The resulting plane is defined as:

$$Z=a+bX+cY \qquad (1)$$

where Z is the failure plane depth, X and Y are easting and northing (UTM), and a-c are fit parameters determined from a multiple linear regression of the 29 input points. Given the relatively consistent bedding planes and assumption of a dip-slope failure, a plane is the simplest first approximation of the failure plane, thus we avoid potentially anomalous subsurface variations introduced by more complex fits. We used this resulting best fit plane as a proxy for a dip-slope failure surface, and then compared this fitted failure surface to the one predicted by the refraction survey.

For Vaughn, we hand-augered a borehole near where the refraction survey predicted the shallowest landslide deposit (Figure 2b). We recorded the color, texture, and any potential failure planes we found while augering and compared those to the velocity transitions predicted by the inversion models.

4.3. Passive Array on Vaughn

We can infer an additional depth constraint from the peak frequencies recorded during a passive array seismic study performed on Vaughn as part of a different experiment (Cerovski-Darriau et al., 2014). The passive array consisted of 5 short-period, three-component seismometers (L-22) obtained from IRIS PASSCAL that were deployed

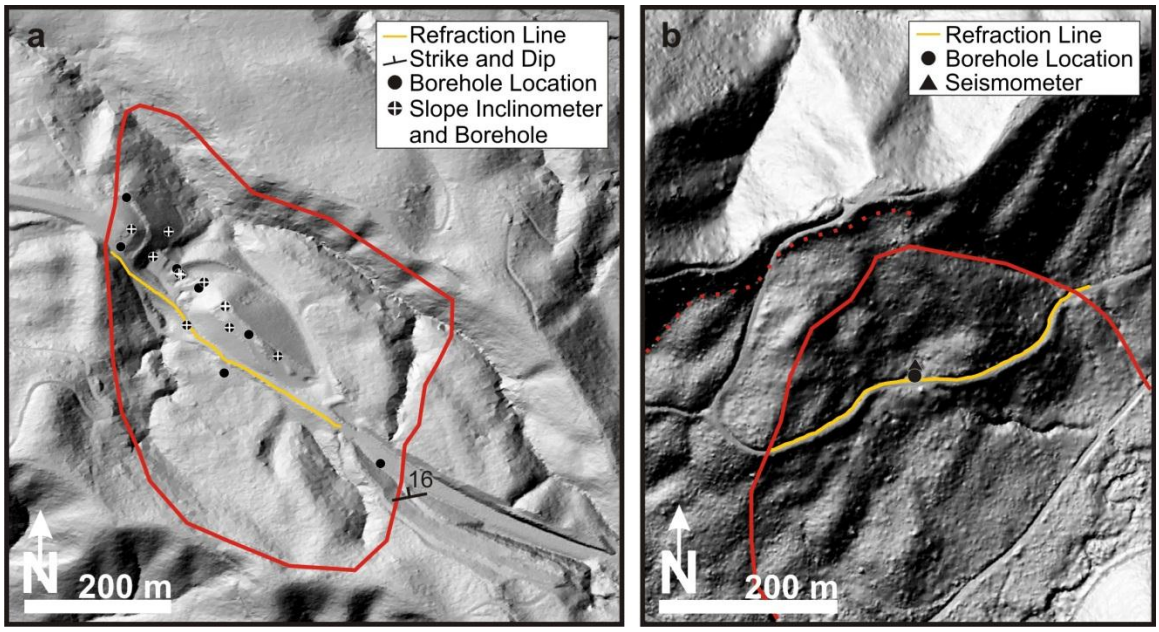

Figure 2. 1 m lidar hillshade of study sites with landslide deposit outlines in red and refraction survey location in yellow. (a) Cougar Creek landslide with the location of boreholes (black circle) and slope inclinometer (white cross) used to fit the failure surface. The strike-and-dip used for comparison is located near the eastern extent of the deposit. (b) Vaughn landslide with the location of the hand-augered borehole (black circle) and nearest seismometer (black triangle) along the refraction line. The Vaughn landslide is likely a more recent reactivation within an older landslide marked by the dashed red line.

to recorded ambient noise and microtremors for 2 months. The seismic data was converted using the miniSeed toolbox and processed in Matlab, then compared to weak ground motion events within 100 km obtained using irisFetch and stacked ambient noise. We high-pass filtered the data at 1 Hz and then smoothed using variable Gaussian weighted averages. One of the stations was located within a few meters of the hand-augered borehole (Figure 2b), allowing us to use the peak frequency recorded at that station to calculate the landslide thickness using the relationship:

$$f = V_s/4H \qquad (2)$$

where f is the peak frequency (Hz), V_s is the shear wave velocity (m/s), and H is the thickness (m) of the material (Bard, 1998; Jongmans and Garambois, 2007). The peak frequency was estimated using the single station method, or H/V technique. The H/V

technique compares horizontal to vertical ground motion to calculate the H/V spectral ratio, which relates to the resonance frequency (Nakamura, 1989). The peak frequency were calculated using varying smoothing values (σ=0.1 Hz and σ=0.25 Hz). Using the approximate shear wave velocity of landslide colluvium from previous studies, we can rearrange equation 2 and solve for the landslide thickness at that station.

5. Results

5.1. Cougar Creek

From the refraction survey time-term inversions, we chose the 2- and 3-layer models with the smallest combined model and ray tracing RMS error to compare with the fitted failure plane. The uppermost layer of the inversion models is the slowest velocity (0.8 km/s and 0.7 km/s), followed by an intermediate layer in the 3-layer model (1.8 km/s), and then the basal bedrock layer (2.9 km/s and 3.1 km/s) (Figure 3a-b). The refraction survey began on the ridge and extended to the landslide deposit, therefore results from the ridgeline (X_{dist} =0-47.5 m; grey box in 3a-b) are excluded from further calculations because they likely reflect the weathering profile of the ridge and not the actual landslide deposit. Using the depth of the slowest velocity layer from $X_{dist} \geq$50 m, the inversion models predict a landslide thickness of 14.2-26.5 m, or 20.0 ± 3.3 m (mean ± sd), for the 2-layer and 9.4-23.8 m, or 15.8 ± 3.5 m (mean ± sd), for the 3-layer inversion. The associated ray tracing RMSE is 3.31 ms and 3.67 ms respectively, and the model RMSE is 1.78 ms and 1.30 ms respectively (Table 1).

Table 1. Inversion root mean square errors (RMSE)

Location	**RMSE**	
Cougar Creek	*Model (ms)*	*Ray Tracing (ms)*
2-Layer	1.78	3.31
3-Layer	1.3	3.67
Vaughn	*Model (ms)*	*Ray Tracing (ms)*
2-Layer	2.79	4.1
3-Layer	2.41	7.48

The first-order polynomial fitted failure plane has an R^2 of 0.92, indicating a simple planar approximation accounts for most of the variation between the borehole and inclinometer data (Figure 3c), further validating our assumption that this is a dip-slope failure. The fitted plane is defined by the equation:

$$Z=9.48\text{x}10^5-0.04X-0.19Y \qquad (3)$$

The downslope gradient is dominated by the *Y* (northing) term (Table 2), and can therefore be approximated as 0.2 ± 0.02 (~10-13°). There is some variability within the plane (RMSE of 4.9 m), but we maintain a plane is a good approximation. The fit parameters and associated errors are included in Table 2.

Table 2. Data fit parameters and comparisons

Fit Parameters									
Cougar Creek	**n** (data)	**a**	***se***	**b**	***se***	**c**	***se***	$\mathbf{R^2}$	***RMSE*** *(m)*
2-Layer	172	$9.22\text{x}10^5$	$1.16\text{x}10^5$	-0.03	0.02	-0.18	0.02	0.96	3
3-Layer	172	$7.13\text{x}10^5$	$1.40\text{x}10^5$	0.01	0.03	-0.15	0.03	0.94	3.6
Subsurface Data	29	$9.45\text{x}10^5$	$1.29\text{x}10^5$	-0.04	0.03	-0.19	0.02	0.92	4.9

Comparison Between Inversion Models and Fitted Plane	
Cougar Creek	***RMSE*** *(m)*
2-Layer	4.9
3-Layer	3.7

To determine which inversion model best predicts the depth of the failure plane, we compared the failure plane depth (*Z*) predicted by equation 3 to the depth given by the 2- and 3-layer models at the base of the slowest (red) layer (Figure 3a-b). From these residuals—calculated as the difference between the predicted (black) and modeled depths (blue or yellow) in Figure 3d (Table D2)—we determined the RMSE for the two inversion models is 4.9 m and 3.7 m respectively (Table 2). Therefore, the upper boundary layer of the 3-layer model predicts the location of the failure plane within 3.7 m, which is ~30% better than the 2-layer model. The landslide thickness predicted by equation 3 is 10.3-26.2 m, or 16.2 ± 3.8 m (mean ± sd), which is not statistically different

from the 3-layer model (15.8 ± 3.5 m) (Table D2). Furthermore, we fit a line to the 2- and 3-layer line (dashed lines in Figure 3d) using multiple regression to simplify the comparison with the intersection line between the fitted failure plane and the refraction survey (black line in Figure 3d) (Table 2). The 3-layer regression line (dashed yellow) most closely matches the failure plane intersection (black line) (Figure 3d) (Table 2).

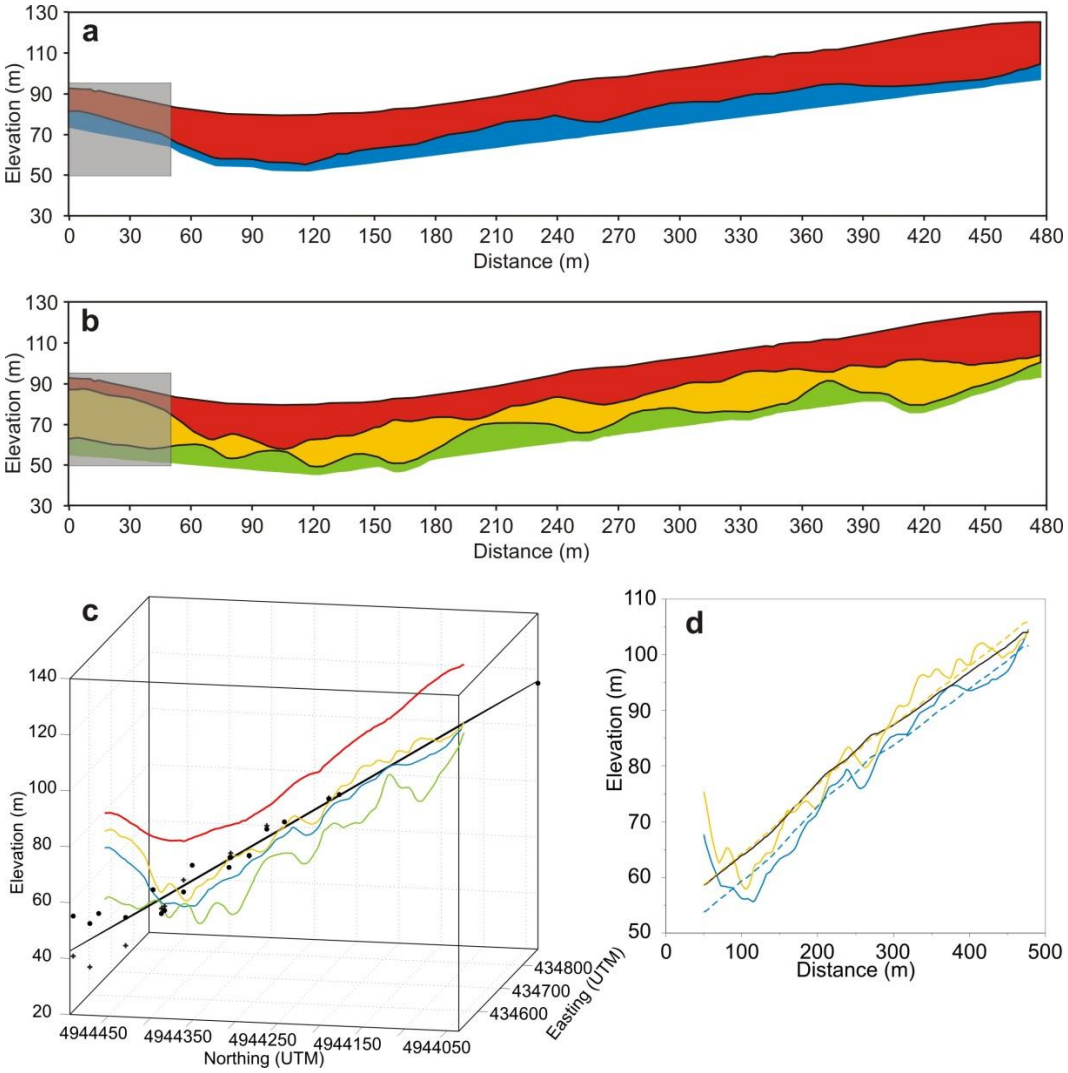

Figure 3. (a) 2-layer inversion model of Cougar Creek where slower, upper layer is 0.8 km/s (red) and faster, lower layer is 2.9 km/s. (b) 3-layer inversion model where slowest top layer is 0.7 km/s (red), middle layer is 1.8 km/s (yellow), and fastest bottom layer is 3.1 km/s. (c) Failure plane (black) fitted to borehole (circles) and inclinometer (crosses) data projected to the refraction survey line (red) and the inversion model interfaces from the 2-layer (blue) and 3-layer (yellow and green) in 3a-b. (d) Comparison of the fitted failure plane (black), 2-layer model (solid blue), 3-layer model (solid yellow), and linear fit of 2- (dashed blue) and 3-layer (dashed yellow) models. The refraction survey began on the ridge and extended to the landslide deposit, therefore results from the ridgeline (X_{dist}=0-47.5 m; grey box in 3a-b) are excluded in 3c-d.

In addition, we compared the fitted plane gradient and direction with strike-and-dip of the bedding planes. The strike of fitted failure plane is 78°NE, and the dip is 12°N. The average local orientation of the bedding planes, based on 6 strike-and-dips from within a kilometer of the landslide deposit (Snavely et al., 1976), is 54°NE, 12°N. We took one additional strike-and-dip (79°NE, 16°N) from a ridge along the eastern extent of the Cougar Creek watershed. The similarity between the strike-and-dip of the fitted plane and the bedding planes in the area corroborates our assumption that these are dip-slope failure planes than can be approximated by a first order polynomial surface.

5.2. Vaughn

For Vaughn, we also selected the 2- and 3-layer inversion models with the smallest combined RMSE. These two best time-term inversion models show the uppermost layer is 0.4 km/s, followed by an intermediate layer of 2.1 km/s (in the 3-layer model), and the basal bedrock layer is 3.3 km/s (Figure 4). Using the depth of the slowest velocity layer, the models predict a landslide thickness of 2.0-20.1 m, or 8.1 ± 3.9 m (mean ± sd), for the 2-layer and 1.4-14.0 m, or 5.7 ± 2.5 m (mean ± sd), for the 3-layer inversion (Table D3). The associated ray tracing RMSE is 4.10 ms and 7.48 ms respectively. The smallest model RMSE was 2.79 ms for the 2-layer and 2.41 ms for the 3-layer model (Table 1).

We hand-augered a borehole near where the model predicted the thinnest landslide deposit at X_{dist}=210 m (where X_{dist} is the distance from the start of the geophone line) through the shear zone until reaching intact rock. We augured through stiff, mottled clay with shear lines at 3.6 m and reached intact rock at the base of the borehole at 4.8 m. Thus, we estimate that the landslide deposit was 3.6 m thick at this location. At the corresponding X_{dist}, the 2- and 3-layer inversion models predict the landslide is 3.8 m and 2.2 m thick, confirming that the 2-layer inversion model is a better match with the failure plane (RMSE=0.2 m) (Figure 4) (Table D3).

The peak frequency at the seismometer closest to the hand-augered borehole, determined from the H/V spectral ratio, was calculated from 5 weak motion events (M_w 2.6-4.1) that spanned one month and 5-400 s sections of stacked ambient noise data. From this combination of weak motion and ambient noise, we found the peak frequency

(*f*) at this station varied between 5-7 Hz (Cerovski-Darriau et al., 2014). In order to determine the landslide thickness at this point, we re-arranged equation 2 to solve for *H*. Using a shear wave velocity (V_s) typical of landslides (120-140 m/s) (Allstadt et al., 2013) and our measured peak frequencies, we can estimate the landslide thickness at X_{dist} =210 m to verify our results. From equation 2, we find the landslide should be 5.5 ± 0.9 m (mean ± sd) thick at X_{dist} =210 m. This estimate most closely corresponds with the 2-layer model and is consistent with our auger log, adding further support to the validity of the 2-layer model.

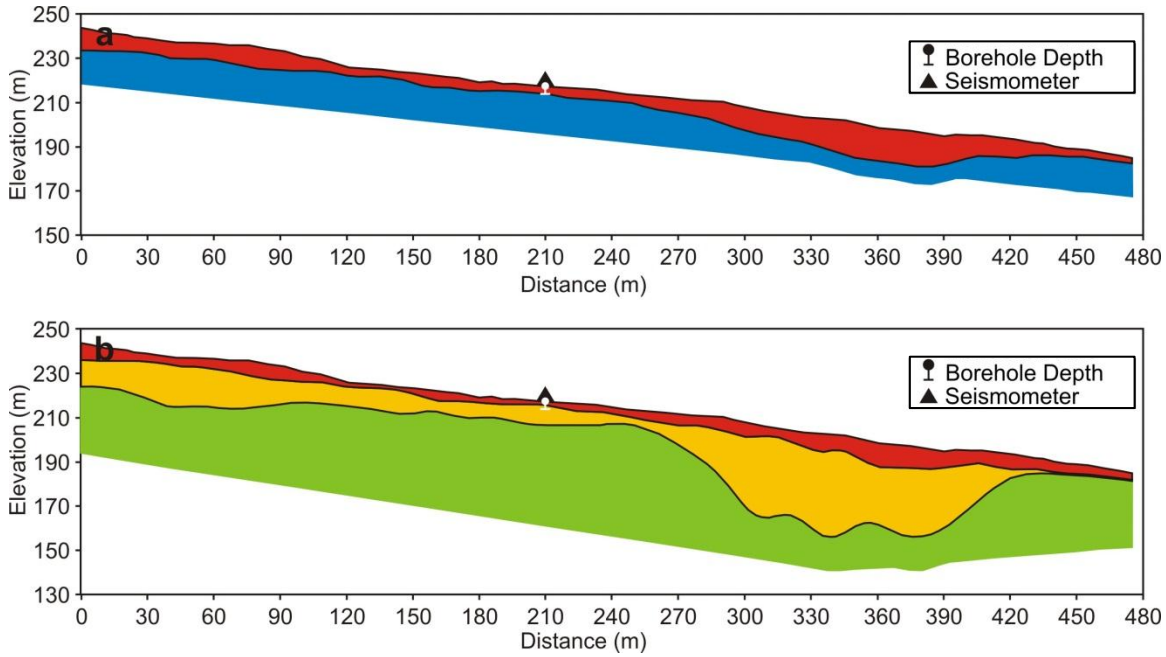

Figure 4. (a) 2-layer inversion model of Vaughn where slower, upper layer is 0.4 km/s (red) and faster, lower layer is 3.3 km/s. The seismometer (black triangle) and borehole (white circle) with depth to failure plane are located at X_{dist}=210 m. (b) 3-layer inversion model where slowest top layer is 0.4 km/s (red), middle layer is 2.1 km/s (yellow), and fastest bottom layer is 3.3 km/s. The depth to the failure plane determined from augering is 3.6 m (white).

6. Discussion

The large, deep-seated landslides in the OCR are composed of highly weathered colluvium that becomes stiffer and more clay-rich with proximity to the failure plane. Below the failure plane, fresh, intact siltstone and sandstone layers are preserved. Generally a single distinct failure plane was evident from the borehole data and could be located within 10s of centimeters—we only found a few instances of potentially multiple

slip surfaces. Therefore, because seismic waves travel more quickly through denser material, we expect to find the slowest velocity layer determined from the refraction data corresponded to the colluvium and for the velocity to sharply increase below the landslide deposit. Based on our comparison between the inversion models and the subsurface data, the slowest velocity layer from the refraction data indeed corresponds to the landslide deposit and produced velocities similar to other landslide refraction studies (e.g. Caris and Van Asch, 1991). A layered inversion model, as opposed to a more gradational inversion technique (e.g. tomographic), was appropriate due to the distinct boundary between the highly weathered colluvium of the landslide and the intact bedrock below. The base of this low velocity zone accurately predicts the location of the basal landslide shear surface—likely to within a meter.

For Cougar Creek the landslide failure plane approximated by 29 boreholes and slope inclinators best fit the 3-layer model, while a 2-layer model best correlated with our borehole data at Vaughn. However, in both cases, the model with the lowest combined model and ray tracing RMSE correlated best with our subsurface data. At Cougar Creek, error between the fitted failure plane and the base of the low velocity zone from the refraction survey was larger than a meter (RMSE=3.7 m). However, we posit some of this error is due to approximating the failure surface as a simple plane because, when fitting a line to the refraction boundary or the borehole data, the RMSE is similar (3.6 m for the low velocity boundary and 4.9 m for the failure plane) despite a R^2 of 0.92 and 0.94 respectively. Thus the RMSE is equivalent to the variability of the inversion model itself, and not the accuracy in predicting the location of the landslide failure plane. Additionally, the disparities mostly arise from lateral variations—not downslope variations. Regardless, for Cougar Creek, simplifying the surfaces as planes only generates a 20% error in determining the landslide thickness. In addition, the similarity of dips between the fitted plane, the local bedding planes, and the strike-and-dip taken near the edge of the deposit corroborate a predominately dip-slope failure along a sandstone-siltstone bedding plane.

The correlation between the hand-augered borehole and the refraction boundary at Vaughn more directly demonstrates the accuracy of the inversion models. Our borehole reached fresh rock at 4.8 m and likely crossed the failure plane at 3.6 m where the model

predicted the landslide deposit should be 3.8 m thick. Thus, we estimate a refraction survey can determine the location and thickness of a landslide deposit to within a meter, or within 10-20% of the actual landslide thickness.

Based on the above results, we confirmed that refraction surveys are a useful method of determining the location and thickness of landslide deposits in the OCR. We also seem to be imaging an intermediate weathering zone, at least on Cougar Creek, as evident from the thickening intermediate velocity layer near the ridgeline (X_{dist}=0-47.5 m) (Figure 3b). Therefore, besides just characterizing landslides, this could be a useful tool for geomorphologists trying to understanding the critical zone transition from bedrock to soil. However, we would first need to analyze core samples from this intermediate layer to verify this velocity change reflects a weathering transition. In addition, we verified that the Cougar Creek landslide was likely a dip-slope failure, and thus a relatively constant thickness from head to toe, because the plane fitted to the borehole data accurately predicted the downslope location of the landslide failure surface and correlated well with bedding plane strike-and-dips.

The velocity contrast between the landslide deposits and the underlying bedrock likely makes this method applicable across the OCR. Additionally, because these landslide deposits are thinner than we originally anticipated, a sledge hammer and striker plate can likely be used as the active source instead of a truck-mounted 'slingshot'. This removes the limitation of road access, allowing this method to be used for any landslide deposit <30 m thick (Schrott and Sass, 2008). Therefore, as long as the geophone line can span the requisite 4-5 times the landslide depth and a sledge hammer can penetrate to that depth; this method has widespread application for characterizing the depth and location of landslide failure planes.

This improved understanding of OCR deep-seated landslides will aid future landslide hazard models that require the depth to the failure plane and the style of failure to accurately determine hillslope stability and/or the likelihood of landslide reactivation (e.g. Olsen et al., 2015 and references therein). Currently, ODOT has a preliminary coseismic landslide hazard model for the Oregon Coast Range (Olsen et al., 2015). However the model does not differentiate between new failures and reactivations nor landslide type (e.g. shallow and deep-seated), and it relies mainly on empirical

parameters and probabilistic regression to predict the hazard. While we only characterized two landslides in this study, the method can be applied more widely to get better depth constraints regionally. Since these are dip-slope failures, we can assume the thickness remains relatively constant downslope, meaning a single refraction survey across the landslide provides a good approximation of the overall depth. Having the depth of these large landslide deposits will help in determining the likelihood they will reactivate—a potential coseismic hazard that is unaccounted for in the current ODOT report—as seismic shaking is amplified where the material is thicker and softer than the underlying bedrock (e.g. landslide deposits) (Field et al., 2001; Allstadt et al., 2013). In addition, the depth of these landslides provides constraints on landslide scaling relationship that can help characterize the frequency of landslides in the OCR and the volume of sediment eroded by large landslides to determine their contribution to landscape evolution.

7. Conclusion

Here we validated a method to characterize deep-seated landslides in the OCR that can be used in the future to improve our understanding of the hazard posed by these features. We have demonstrated that refraction surveys are a cheap and effective way to characterize the subsurface, and an efficient alternative method to drilling boreholes to determine the depth of these deep-seated landslides. Our unique multidisciplinary dataset—that includes seismic refraction surveys of two landslides, borehole data, hand auger samples, and lidar analysis—allowed us to verify that the low velocity layer imaged by a refraction survey accurately reflects the landslide deposit. Therefore the depth and location of this layer can be used to infer the depth of the deposit and the location of the failure plane. We determined there is good agreement between refraction survey and borehole data, likely within a meter, or 10-20% of landslide thickness. In addition, we confirmed the Cougar Creek landslide has a planar failure, which validates the assumption that OCR deep-seated landslides slip as dip-slope failures. This information can be used to inform slope stability models that are highly dependent on the failure style and landslide depth. We successfully demonstrated the utility of this method

at two sites in the OCR, and anticipated the technique is widely applicable across western Oregon and beyond.

CHAPTER V

SUMMARY

In this dissertation I explore the role of landslides in landscape evolution—both on climatic (10^4 yrs) and human (10^1 yrs) timescales—by applying a variety of traditional and novel geomorphic tools (e.g. high-resolution topographic analysis, soil profiles, and field surveys) as well as techniques from other fields (e.g. tephrochronology, electron microprobe analysis, seismic refraction) to this geomorphic problem.

In Chapter II, I date ridgelines in New Zealand in order to reconstruct the post-LGM paleolandscape through time. I use major oxide geochemistry and tephrochronology of volcanic glass collected in the field to constrain the ridgeline ages. Then, I use those ridgelines to construct a sequence of paleosurfaces, which allows me to calculate the catchment-averaged erosion rate through time. I determine the long-term, post-LGM (~18 kys) erosion rate for the study area is 1.6 mm/yr, but that the rate was close to the background uplift rate (~0.7 mm/yr) by the Whakatane eruption (5.5 ka)—indicating that hillslopes equilibrated in ~10-15 kys. Additionally, I found a sharp increase in erosion rates between 3.4 ka and today, which I hypothesize is due to recent human disturbance of the landscape.

In Chapter III, I show that human-driven land disturbances over a few decades can initiate a geomorphic response that persists on the landscape for a century or more. I determine that the historic erosion rate for this same New Zealand study area is an order of magnitude greater (~10 mm/yr) than the post-LGM (or longer) catchment-averaged erosion rate. To calculate the historic erosion rate, I use aerial photos and lidar to map landslides, then develop a technique to infer landslide velocity using spectral classification of the digitized aerial photographs, and lastly, combine the landslide map and velocities with depth measurements from the field to determine the sediment flux. In Chapter III, I again calculate a catchment-wide erosion rate, but using different techniques and over a different timescale.

In Chapter IV, instead of calculating a sediment flux, I verify a geophysical method for quantifying landslide depth by comparing geologic and geomorphic data to

seismic refraction results from two landslides in western Oregon (USA). These landslides are also potentially significant contributors to the regional sediment flux over geologic timescales as well as being potentially hazardous to humans over the shorter-term, earthquake cycles. Therefore, while I take a different approach in Chapter IV, I am still motivated by understanding the role of landslides in landscape evolution. In addition, by validating the utility of seismic refraction for investigating large landslides, I demonstrate an applied technique that can improve landslide characterization and, potentially, hazard maps in the future.

APPENDIX A

SUPPLEMENTARY PHOTOS

Figure A1. Oblique aerial view of the central Mangataikapua catchment from the southern edge of the study area (photo credit: Joshua J. Roering).

Figure A2. Photos of the Mangataikapua study area: (a) view towards the Mangataikapua outlet from the Waipaoa River, (b) view towards the Mangataikapua headwaters from near the woolshed in the middle of the study area, (c) view downstream from near the Mangataikapua headwaters, and (d) cobbles and boulders weathering in the stream channel (photo credit: Corina Cerovski-Darriau).

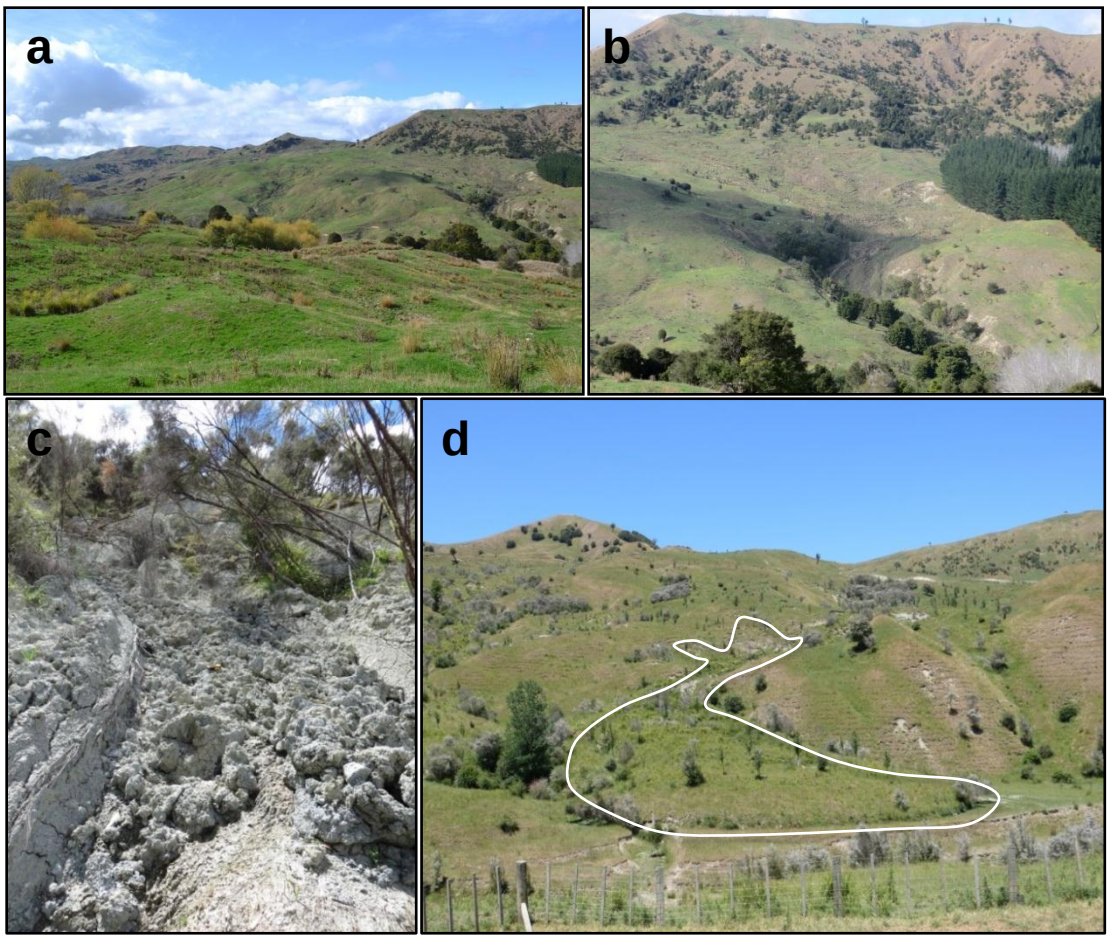

Figure A3. Photos of earthflows in the Mangataikapua study area: (a) view from an older landslide deposit (note the hummocky topography) across the channel towards southeast, (b) view of an active earthflow extending from the steep, sandstone ridge to the channel (located at the right edge of a), (c) recent, fast-moving earthflow with distinct lateral margins and slickensides, and (d) slow-moving or dormant earthflow grading to a low terrace above the Mangataikapua stream (the upright, young trees on the earthflow are evidence of no movement in the past year) (photo credit: Corina Cerovski-Darriau).

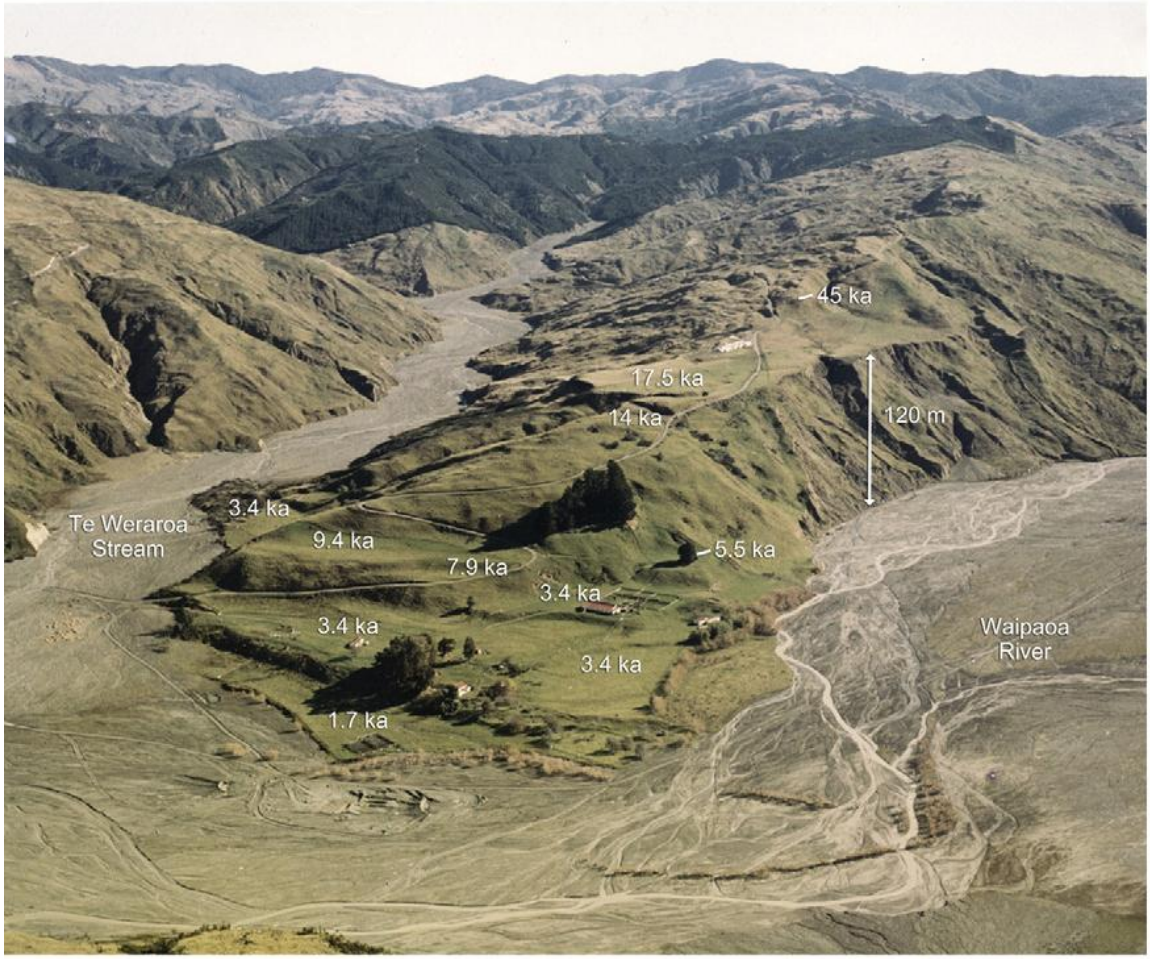

Figure A4. Oblique aerial photograph of terraces preserved in the upper Waipaoa River at ~60 km inland from the coastline. Terrace ages are in cal. ka from oldest to youngest: Rotoehu (~45 ka), Rerewhakaaitu (~17.5 cal. ka), Waiohau (~14.0 cal. ka BP), Rotoma (~9.4 cal. ka), Mamaku (~8 cal. ka), Whakatane (~5.5 cal. ka), Waimihia (~3.4 cal. ka), and Taupo (~1.7 cal. ka). Note the period of accelerated fluvial incision between ~14.0 and 9.4 cal. ka recorded by the greater relative spacing between these terraces (figure and caption from Marden et al., 2014).

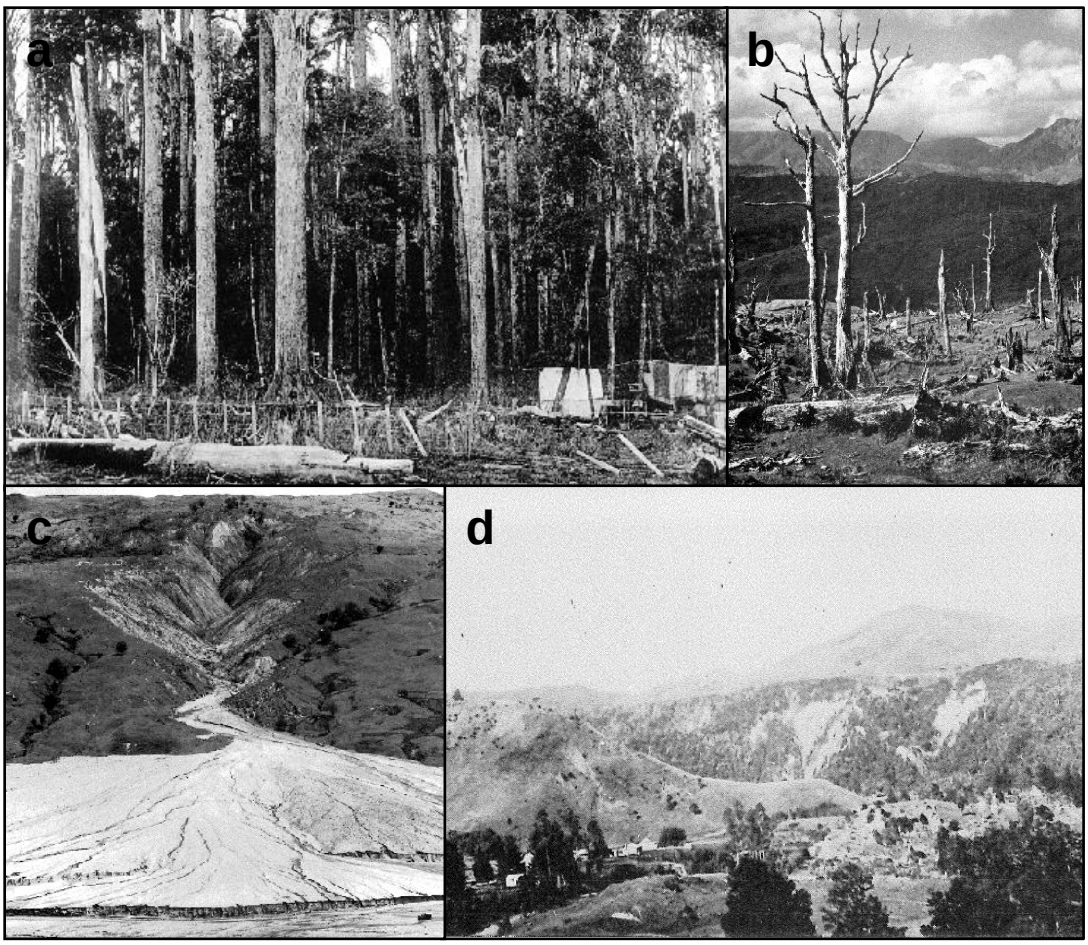

Figure A5. Photos of land-use change in the upper Waipaoa Basin: (a) view of the podocarp forest in 1897 (photo from Anderson, 2010), (b) view of podocarp forest post-burning (photo from Gage and Black, 1979), (c) view of gully and alluvial fan that developed in the decades following deforestation (photo from Allsop, 1973), and (d) view of Waipaoa station a few decades after deforestation began (note most dense canopy is gone and landslides are evident in the background) (photo from Gage and Black, 1979).

Appendix A References Cited

Allsop, F. (1973), The Story of the Mangatu, New Zeal. For. Serv. Inf. Ser., 62, 100.

Anderson, I. (2010), Pioneering in Kanakanaia-Te Karaka, Ian Anderson, Gisborne.

Gage, M., and R. D. Black (1979), Slope-stability and geological investigations at Mangatu State Forest, New Zeal. For. Serv. Tech. Pap., 66.

Marden, M., H. Betts, a. Palmer, R. Taylor, E. Bilderback, and N. Litchfield (2014), Post-Last Glacial Maximum fluvial incision and sediment generation in the unglaciated Waipaoa catchment, North Island, New Zealand, Geomorphology, 214, 283–306, doi:10.1016/j.geomorph.2014.02.012.

APPENDIX B

CHAPTER II SUPPLEMENTARY MATERIAL

Electron microprobe analysis

Tephra composition was determined from electron microprobe analysis (EMPA). For each tephra pit sample, 12 unique shards of tephra were probed (n=12). We ran 41 total samples (2 repeated samples) in batches A-G. Any low totals were discarded, making an average of 11 useable shards per sample tephra. Each useable shard was then correlated to a Taupo Volcanic Zone (TVZ) tephra using discriminant function analysis (DFA) and verified from binary plots of various diagnostic oxides. K_2O vs. CaO is the most widely used for identifying TVZ tephra (Figure 2a), but we found MgO, FeO, MnO, and TiO_2 aided in identifying tephra of similar composition (Figure B1). The oldest tephra (with n>1 shard) and the average composition of only those shards is reported in Table B1. If the oldest tephra had only one shard (e.g. 1, 15, 21, 24, or 33), or if we suspect it was misidentified (e.g. 5, 7, 10, 13, 30), the likely alternative tephra is listed. For repeated analyses, the reported composition (Figure 2a) is a combined average (i.e. 25a & 25b, and 37a & 37b).

Roughness calculations

The raw and smoothed calculated roughness for each point is shown in Table B1. The roughness determined from a 15 m buffer around each sample location ("Buffered (15m)") in Table B1) is used to develop the roughness-age relationship. The input roughness for each pit is plotted in Figure B2. The average for all pits of the same age (i.e. tephra) was fitted using a linear and power function. We found the linear function (Figure 2c) was most successful at predicting the correct tephra (Table B1), despite the power function having a greater R^2 value (Figure B3). Using the linear fit, we set the upper and lower limit for each roughness-age bin from the midpoint between the predicted roughness for point (Rotoma, Whakatane, Waimihia, Taupo, and no tephra).

Modified Hack's constant

The longitudinal profile of a stream reflects the underlying material as well as the tectonic and climatic environment. In order to determine the paleochannel profiles, we modified the Hack's constant to better fit the Mangataikapua catchment. Hack's Law [*Hack*, 1957] is an empirical relationship between stream length and the upstream drainage area (*A*), and is used to account for catchment shape. We use the form [*Whipple and Tucker*, 1999],

$$A=kx^{h} \quad (1)$$

where k is a dimensional constant, *x* is the Euclidean distance from the drainage divide, and *h* is Hack's constant—or the reciprocal of the Hack's Law exponent—typically between 1.67-1.92 [*Hack*, 1957; *Whipple and Tucker*, 1999]. We calculated our own range of values for the Mangataikapua because the catchment shape is more elongate than typical basins. We fit a line to a log-log plot of values for the Mangataikapua and found the *h*=1.4-1.6. This is close to the average value *Crosby and Whipple* [2006] found for the entire Waipaoa (*h*=1.55). We used *h*=1.6 for a best fit of our elevation data.

Reconstruction trials

We tested various fits for each paleosurface in order to quantify the variability in the resulting volume and to test the fit itself. The most trials were performed for the LGM paleosurface, which had the fewest points to constrain the morphology. We tested a cubic and linear interpolation, and found the cubic center interpolation gave the most realistic fit. We initially tried using a channel that follows the modern channel bed, but opted for a simplified valley profile to define the XY position of the channel to avoid forcing the surface to fit the modern sinuosity. We also tried two ways to define the break points, or the 'relict landforms', used in the fit. First we outlined all neighboring landforms of like roughness with a polygon, and used those polygons as the relict surfaces in the interpolation. However, we ultimately decided to use the existing ridge network and assign ridge segments a modal roughness age, in order to form a realistic ridge and valley topography (with the exception of the LGM because we did not have sufficient ridgelines

of LGM age, as described in the text). Lastly, we compared the modern boundary elevation with a spline fit of the modern elevation. As described in the text, the spline fit introduced less spurious ridges and valleys than using the raw modern boundary elevation profile.

Additionally, we created a surface only using the boundary elevations (spline and modern) and the paleochannel profile, which acts as an upper bound for surfaces younger than the LGM. We also did one trial for the Waimihia surface where we altered the concavity of the paleochannel to test the effects of a non-constant concavity. It did not change the volume substantially, so opted to use the Waimihia paleosurface with concavity equal to the other timesteps ($\frac{m}{n}$=0.4).

Error analysis

For the total volume calculated between each paleosurface and the modern DEM, the standard deviation is the variance between all trials for each respective time interval and the standard error accounts for the number of trials. For the volume difference between paleosurfaces, we tested various pairs of surfaces; the standard deviation is the variance between the resulting volumes, and the standard error accounts for the number of combinations. For the strict mathematical difference calculated by subtracting the total volumes (i.e. "Cumulative Subtraction" on Table 3), the standard deviation (or standard error) is the standard deviation (or standard error) previously calculated for each surface added in quadrature. The standard deviation for erosion rate is the resulting Gaussian error propagation of the standard deviation from each volume difference.

Appendix B References Cited

Crosby, B., and K. Whipple (2006), Knickpoint initiation and distribution within fluvial networks: 236 waterfalls in the Waipaoa River, North Island, New Zealand, Geomorphology, 82(1-2), 16–38, doi:10.1016/j.geomorph.2005.08.023.

Hack, J. T. (1957), Studies of longitudinal stream profiles in Virginia and Maryland, USGS Prof. Pap. 249, 97.

Whipple, K., and G. Tucker (1999), Dynamics of the stream-power river incision model: Implications for height limits of mountain ranges, landscape response timescales, and research needs, J. Geophys. Res. Solid Earth, 104, 661–674.

Table B1. EMPA Results, Roughness, and Predicted Tephra

Sample		Sample Info		Tephra					Roughness			Location		Oxide Composition (average wt %)									Standard Deviation (wt %)								
Pit #	Puck	Type	Sample Depth	EMPA Tephra	Alt	Predicted Fit	Age (ky)	n (shards)	Raw	Smoothed (15m)	Buffered (15m)	Latitude	Longitude	Na2O	SiO2	K2O	Al2O3	MgO	FeO	CaO	MnO	TiO2	*Na2O*	*SiO2*	*K2O*	*Al2O3*	*MgO*	*FeO*	*CaO*	*MnO*	*TiO2*
1	E4	Pit	0.06-0.13	Taupo	Wm	None	1.718	5	1.056	1.073	1.065	-38.365	177.843	5.150	74.464	2.857	13.374	0.282	2.018	1.518	0.087	0.249	*0.325*	*0.267*	*0.079*	*0.152*	*0.008*	*0.053*	*0.026*	*0.002*	*0.012*
2	E5	Pit	0.1-0.2	Taupo	--	None	1.718	9	1.048	1.068	1.061	-38.352	177.845	5.124	74.447	2.832	13.375	0.293	2.034	1.516	0.101	0.278	*0.259*	*0.544*	*0.058*	*0.254*	*0.064*	*0.137*	*0.056*	*0.051*	*0.023*
3	A6	Pit	0.13-0.2	Waimihia	--	Rotoma	3.401	2	1.006	1.013	1.012	-38.365	177.845	5.021	75.209	2.942	13.183	0.205	1.879	1.277	0.081	0.203	*0.144*	*0.262*	*0.022*	*0.047*	*0.038*	*0.070*	*0.067*	*0.003*	*0.055*
4	B6	Pit	0.25-0.29	Whakatane	--	Whakatane	5.526	7	1.017	1.036	1.034	-38.360	177.847	4.835	77.210	3.539	12.535	0.119	0.838	0.760	0.054	0.109	*0.305*	*0.243*	*0.254*	*0.127*	*0.016*	*0.050*	*0.083*	*0.012*	*0.021*
5	D5	Pit	0.95-1.0	Opepe	Tp	Rotoma	9.991	7	1.003	1.017	1.014	-38.370	177.848	4.658	75.475	2.946	13.131	0.215	1.782	1.532	0.061	0.200	*0.219*	*0.429*	*0.114*	*0.214*	*0.016*	*0.060*	*0.138*	*0.005*	*0.030*
6	F5	Pit	0.24-0.28	Whakatane	--	Rotoma	5.526	3	1.015	1.027	1.023	-38.354	177.850	4.922	76.839	3.893	12.506	0.106	0.906	0.670	0.049	0.110	*0.187*	*0.236*	*0.064*	*0.214*	*0.006*	*0.082*	*0.013*	*0.005*	*0.034*
7	B1	Pit	0.3-0.35	Rotoma	Wk	Rotoma	9.423	4	1.007	1.035	1.022	-38.366	177.857	4.973	77.195	3.418	12.513	0.110	0.819	0.796	0.058	0.118	*0.340*	*0.286*	*0.118*	*0.094*	*0.024*	*0.051*	*0.029*	*0.004*	*0.023*
8	D6	Pit	0.83	Whakatane	--	Rotoma	5.526	5	1.002	1.012	1.012	-38.354	177.858	4.378	77.602	3.849	12.461	0.096	0.824	0.646	0.055	0.089	*0.203*	*0.294*	*0.085*	*0.116*	*0.004*	*0.053*	*0.008*	*0.006*	*0.019*
9	B3	Pit	0.26-0.36	Waimihia	--	None	3.401	3	1.065	1.080	1.084	-38.361	177.860	5.253	74.820	2.887	13.212	0.247	1.874	1.368	0.085	0.253	*0.333*	*0.204*	*0.069*	*0.121*	*0.010*	*0.126*	*0.157*	*0.001*	*0.035*
10	B7	Pit	0.38-0.44	Opepe	Wm	Rotoma	9.991	6	1.005	1.016	1.013	-38.352	177.860	4.991	75.383	2.923	13.185	0.183	1.713	1.330	0.081	0.212	*0.533*	*0.453*	*0.039*	*0.167*	*0.012*	*0.033*	*0.030*	*0.004*	*0.039*
11	C5	Pit	0.4-0.45	Rotoma	--	Rotoma	9.423	10	1.004	1.010	1.009	-38.358	177.861	4.610	77.492	3.370	12.570	0.125	0.849	0.798	0.064	0.122	*0.274*	*0.338*	*0.043*	*0.119*	*0.004*	*0.053*	*0.013*	*0.033*	*0.016*
12	B2	Pit	0.3-0.35	Waimihia	--	None	3.401	3	1.073	1.088	1.085	-38.362	177.861	5.287	75.035	2.872	13.238	0.182	1.790	1.314	0.077	0.204	*0.189*	*0.069*	*0.108*	*0.046*	*0.007*	*0.038*	*0.022*	*0.004*	*0.018*
13	B4	Pit	0.36-0.4	Opepe	Wm	Rotoma	9.991	5	1.006	1.006	1.006	-38.361	177.862	5.016	75.374	2.931	13.133	0.191	1.718	1.363	0.067	0.207	*0.197*	*0.153*	*0.102*	*0.121*	*0.005*	*0.013*	*0.110*	*0.008*	*0.030*
14	A5	Pit	0.23-0.3	Taupo	--	Rotoma	1.718	8	1.007	1.021	1.018	-38.355	177.863	5.276	74.303	2.825	13.488	0.274	1.957	1.522	0.085	0.270	*0.263*	*0.081*	*0.037*	*0.163*	*0.005*	*0.105*	*0.029*	*0.009*	*0.022*
15	E1	Pit	0.08-0.11	Taupo	Wm	Rotoma	1.718	6	1.002	1.009	1.007	-38.353	177.866	5.253	74.376	2.828	13.515	0.281	1.868	1.535	0.081	0.263	*0.246*	*0.288*	*0.137*	*0.159*	*0.009*	*0.117*	*0.035*	*0.007*	*0.019*
16	C3	Auger	0.95-1	Rotoma	--	Rotoma	9.423	8	1.019	1.041	1.026	-38.364	177.868	4.789	77.431	3.327	12.387	0.133	0.909	0.836	0.054	0.133	*0.316*	*0.258*	*0.119*	*0.226*	*0.010*	*0.094*	*0.057*	*0.009*	*0.019*
17	C7	Pit	0.68-0.72	Rotoma	--	Rotoma	9.423	6	1.005	1.015	1.014	-38.336	177.868	4.725	77.430	3.361	12.451	0.130	0.914	0.820	0.056	0.113	*0.366*	*0.287*	*0.072*	*0.205*	*0.009*	*0.073*	*0.065*	*0.006*	*0.017*
18	C4	Pit	0.7-0.8	Whakatane	--	Taupo	5.526	3	1.006	1.052	1.05	-38.360	177.868	4.541	77.412	3.852	12.469	0.099	0.846	0.635	0.049	0.097	*0.234*	*0.242*	*0.139*	*0.151*	*0.008*	*0.068*	*0.084*	*0.002*	*0.005*
19	A4	Pit	0.22-0.27	Waimihia	--	Rotoma	3.401	2	1.013	1.019	1.017	-38.358	177.868	5.230	74.943	2.945	13.131	0.216	1.876	1.384	0.079	0.196	*0.404*	*0.328*	*0.029*	*0.316*	*0.036*	*0.018*	*0.080*	*0.006*	*0.072*
20	D1	Pit	0.8-0.85	LGM	Re	LGM	17.496	7	1.001	1.003	1.003	-38.364	177.868	4.230	77.261	4.098	12.493	0.089	0.887	0.785	0.055	0.101	*0.234*	*0.102*	*0.181*	*0.233*	*0.021*	*0.082*	*0.071*	*0.005*	*0.041*
21	F7	Pit	0.18-0.2	Taupo	Wm	None	1.718	10	1.049	1.073	1.071	-38.358	177.872	5.284	74.234	2.843	13.521	0.295	1.968	1.514	0.087	0.254	*0.472*	*0.472*	*0.102*	*0.326*	*0.031*	*0.095*	*0.034*	*0.005*	*0.024*
22	F6	Pit	0.3-0.34	Waimihia	--	None	3.401	5	1.018	1.069	1.067	-38.360	177.873	5.619	74.724	2.946	13.149	0.190	1.783	1.312	0.077	0.200	*0.262*	*0.138*	*0.051*	*0.162*	*0.006*	*0.057*	*0.009*	*0.005*	*0.022*
23	A2	Pit	0.2-0.25	Waimihia	--	Rotoma	3.401	2	1.007	1.022	1.019	-38.347	177.875	4.752	75.354	2.920	13.218	0.213	1.875	1.361	0.083	0.225	*0.313*	*0.323*	*0.075*	*0.056*	*0.046*	*0.038*	*0.066*	*0.015*	*0.051*
24	E3	Pit	0.03-0.07	Kaharoa	Tp	Rotoma	0.636	8	1.035	1.027	1.025	-38.353	177.876	4.334	77.183	4.174	12.614	0.070	0.918	0.574	0.060	0.073	*0.151*	*0.107*	*0.044*	*0.120*	*0.014*	*0.062*	*0.068*	*0.008*	*0.014*
25a	A3	Pit	0.12-0.18	Waimihia	--	Rotoma	3.401	2	1.009	1.018	1.016	-38.357	177.878	5.613	74.624	2.902	13.223	0.225	1.805	1.301	0.084	0.224	*0.142*	*0.209*	*0.007*	*0.113*	*0.043*	*0.110*	*0.033*	*0.004*	*0.056*
25b	F2	Pit	0.12-0.18	Waimihia	--	Rotoma	3.401	2	1.009	1.018	1.016	-38.357	177.878	5.261	74.914	2.968	13.143	0.216	1.845	1.350	0.076	0.228	*0.128*	*0.270*	*0.061*	*0.078*	*0.035*	*0.078*	*0.056*	*0.010*	*0.080*
26	G5	Pit	0	Taupo	--	Kaharoa	1.718	8	1.024	1.054	1.053	-38.353	177.878	5.362	73.742	2.922	13.879	0.287	1.951	1.518	0.086	0.253	*0.297*	*0.456*	*0.114*	*0.240*	*0.030*	*0.113*	*0.024*	*0.005*	*0.025*
27	D3	Auger	2.15	Waimihia	--	Rotoma	3.401	11	1.002	1.024	1.02	-38.359	177.879	4.969	75.563	2.885	13.006	0.187	1.786	1.334	0.077	0.193	*0.332*	*0.244*	*0.088*	*0.183*	*0.006*	*0.049*	*0.018*	*0.008*	*0.027*
28	E7	Pit	0.17-0.2	Taupo	--	None	1.718	10	1.052	1.066	1.064	-38.356	177.879	5.202	74.547	2.857	13.296	0.278	1.971	1.509	0.085	0.255	*0.255*	*0.306*	*0.076*	*0.116*	*0.013*	*0.059*	*0.027*	*0.004*	*0.025*
29	E6	Pit	0.1-0.14	Taupo	--	Taupo	1.718	7	1.015	1.047	1.048	-38.354	177.880	5.007	74.700	2.840	13.400	0.271	1.960	1.492	0.085	0.245	*0.376*	*0.355*	*0.120*	*0.190*	*0.019*	*0.065*	*0.042*	*0.011*	*0.021*
30	C2	Pit	0.7-0.72	Opepe	Tp	kaharoa	9.991	4	1.037	1.058	1.054	-38.359	177.880	5.364	74.757	2.874	13.177	0.250	1.778	1.486	0.084	0.229	*0.167*	*0.208*	*0.124*	*0.187*	*0.048*	*0.092*	*0.111*	*0.011*	*0.034*
31	B5	Pit	0.25-0.28	Whakatane	--	Waimihia	5.526	6	1.044	1.046	1.046	-38.359	177.880	4.561	77.355	3.614	12.534	0.115	0.871	0.786	0.056	0.109	*0.219*	*0.333*	*0.340*	*0.161*	*0.026*	*0.122*	*0.089*	*0.008*	*0.019*
32	D4	Auger	2.1	Rotoma	--	Taupo	9.423	8	1.035	1.053	1.049	-38.359	177.880	4.668	77.526	3.336	12.504	0.123	0.876	0.786	0.059	0.123	*0.315*	*0.430*	*0.083*	*0.157*	*0.009*	*0.081*	*0.049*	*0.005*	*0.019*
33	E2	Pit	0.1-0.2	Taupo	Wm	Rotoma	1.718	10	1.006	1.024	1.017	-38.352	177.881	5.124	74.400	2.880	13.427	0.275	2.021	1.523	0.088	0.263	*0.214*	*0.290*	*0.093*	*0.096*	*0.014*	*0.100*	*0.046*	*0.004*	*0.026*
34	A7	Pit	0.36-0.44	Waimihia	--	Rotoma	3.401	3	1.002	1.040	1.024	-38.339	177.882	5.001	75.300	3.005	13.172	0.180	1.761	1.300	0.079	0.201	*0.226*	*0.100*	*0.039*	*0.090*	*0.005*	*0.072*	*0.025*	*0.006*	*0.020*
35	C1	Auger	0.85-0.9	Rotoma	--	Rotoma	9.423	9	1.008	1.028	1.024	-38.358	177.883	4.614	77.525	3.355	12.434	0.129	0.922	0.842	0.057	0.122	*0.297*	*0.273*	*0.065*	*0.152*	*0.008*	*0.087*	*0.079*	*0.006*	*0.034*
36	F4	Pit	0.32-0.37	Rotoma	--	Waimihia	9.423	3	1.042	1.047	1.044	-38.349	177.889	4.861	77.004	3.421	12.630	0.132	0.951	0.830	0.056	0.116	*0.261*	*0.252*	*0.096*	*0.136*	*0.003*	*0.057*	*0.012*	*0.008*	*0.018*
37a	A1	Pit	0.15-0.2	Whakatane	--	Whakatane	5.526	3	1.028	1.032	1.033	-38.338	177.891	4.915	77.174	3.469	12.458	0.101	0.955	0.758	0.056	0.115	*0.452*	*0.312*	*0.331*	*0.080*	*0.041*	*0.006*	*0.050*	*0.016*	*0.011*
37b	F1	Pit	0.15-0.2	Whakatane	--	Whakatane	5.526	4	1.028	1.032	1.033	-38.338	177.891	4.662	77.387	3.427	12.452	0.135	0.916	0.823	0.053	0.143	*0.083*	*0.247*	*0.117*	*0.179*	*0.010*	*0.073*	*0.070*	*0.005*	*0.014*
38	C6	Pit	0.4-0.45	Rotoma	--	Rotoma	9.423	7	1.005	1.006	1.006	-38.349	177.892	4.912	77.378	3.360	12.426	0.125	0.832	0.784	0.057	0.126	*0.236*	*0.172*	*0.071*	*0.075*	*0.005*	*0.055*	*0.014*	*0.009*	*0.016*
39	G6	Pit	1.5-1.55	LGM	Om	Rotoma	32.755	12	1.002	1.007	1.007	-38.338	177.896	5.549	75.596	2.959	13.196	0.193	1.175	1.082	0.083	0.166	*0.293*	*0.270*	*0.122*	*0.112*	*0.007*	*0.094*	*0.019*	*0.009*	*0.028*

Table B2. Field identified tephra

Sample	Sample Info		Tephra			Location		Roughness	
Pit #	Type	Depth	Field Tephra	Predicted (Fit)	Age (ky)	Latitude	Longitude	Smoothed (15m)	Buffered (15m)
a	Pit	0.4	Waimihia	Whakatane	3.401	-38.36	177.8462	1.012	1.027
b	Auger	0.3	Waimihia	Whakatane	3.401	-38.366	177.8468	1.020	1.029
c	Pit	0.22	Waimihia	None	3.401	-38.359	177.8475	1.101	1.096
d	Cut	1.65	Waimihia	None	3.401	-38.361	177.8478	1.093	1.071
e	Pit	0.1	Taupo	None	1.718	-38.355	177.8498	1.119	1.139
f	Pit	0.4	Waimihia	Whakatane	3.401	-38.352	177.8506	1.019	1.033
g	Pit	<0.4	Waimihia	Waimihia	3.401	-38.354	177.8578	1.028	1.045
h	Pit	0.3	Waimihia	Waimihia	3.401	-38.35	177.8621	1.041	1.043
i	Auger	0.3	Waimihia	None	3.401	-38.355	177.8637	1.063	1.065
j	Pit	0.28	Waimihia	Rotoma	3.401	-38.344	177.8642	1.015	1.019
k	Pit	0.29	Waimihia	Taupo	3.401	-38.362	177.8679	1.037	1.046
l	Auger	>0.75	Waimihia	Taupo	3.401	-38.362	177.8679	1.057	1.046
m	Auger	0.32	Waimihia	Rotoma	3.401	-38.358	177.8679	1.009	1.015
n	Pit	0.4	Waimihia	Rotoma	3.401	-38.343	177.8683	1.010	1.012
o	Pit	0.1	None	None	0	-38.354	177.8692	1.092	1.095
p	Pit	0.31	Waimihia	Taupo	3.401	-38.355	177.8696	1.055	1.050
q	Pit	0.3	Waimihia	Waimihia	3.401	-38.354	177.8698	1.042	1.045
r	Pit	0.22	Waimihia	None	3.401	-38.357	177.8701	1.066	1.066
s	Pit	0.19	Taupo	Whakatane	1.718	-38.355	177.8702	1.033	1.034
t	Pit	0.11	Taupo	None	1.718	-38.355	177.8706	1.188	1.195
u	Pit	0.11	None	None	0	-38.357	177.8707	1.065	1.061
v	Pit	0.12	None	Kaharoa	0	-38.358	177.8708	1.056	1.054
w	Pit	0.25	Waimihia	Taupo	3.401	-38.36	177.871	1.054	1.050
x	Pit	0.1	None	None	0	-38.356	177.8711	1.074	1.072
y	Pit	0.13	None	None	0	-38.358	177.8712	1.073	1.069
z	Pit	0.13	Taupo	Taupo	1.718	-38.357	177.8715	1.042	1.048
aa	Pit	0.13	Taupo	None	1.718	-38.359	177.8717	1.070	1.071
bb	Pit	0.1	None	None	0	-38.357	177.8717	1.108	1.102
cc	Pit	0.19	Taupo	None	1.718	-38.359	177.8718	1.085	1.078
dd	Pit	0.3	Waimihia	None	3.401	-38.36	177.8721	1.071	1.074
ee	Pit	0.1	None	Waimihia	0	-38.358	177.8724	1.049	1.046
ff	Pit	0.45	Waimihia	Rotoma	3.401	-38.347	177.875	1.022	1.024
gg	Pit	0.1	Waimihia	Whakatane	3.401	-38.352	177.8751	1.021	1.027
hh	Pit	0.05	None	None	0	-38.351	177.8753	1.108	1.095
ii	Pit	0.33	Taupo	Whakatane	1.718	-38.353	177.8756	1.027	1.028
jj	Pit	0.1	None	None	0	-38.352	177.8758	1.053	1.055
kk	Pit	0.2	Waimihia	Waimihia	3.401	-38.354	177.876	1.035	1.041
ll	Pit	0.09	None	Kaharoa	0	-38.353	177.8762	1.054	1.052
mm	Pit	0.29	Waimihia	None	3.401	-38.351	177.8762	1.056	1.064
nn	Pit	0.05	None	Whakatane	0	-38.351	177.8767	1.033	1.038
oo	Pit	0.1	None	Whakatane	0	-38.355	177.8768	1.033	1.037
pp	Pit	0.15	None	Taupo	0	-38.353	177.8769	1.046	1.047
qq	Pit	0.1	None	None	0	-38.352	177.8773	1.084	1.075
rr	Pit	0.11	None	None	0	-38.354	177.8775	1.054	1.056
ss	Pit	<0.05	None	Whakatane	0	-38.351	177.8775	1.026	1.032
tt	Pit	0.15	None	Kaharoa	0	-38.356	177.8777	1.059	1.052
uu	Pit	0.26	Taupo	Whakatane	1.718	-38.352	177.8778	1.031	1.034
vv	Cut	0.55	None	None	0	-38.356	177.8779	1.063	1.066
ww	Pit	0.15	None	None	0	-38.357	177.8789	1.069	1.071
xx	Pit	0.15	Taupo	None	1.718	-38.357	177.8789	1.088	1.095
yy	Pit	0.55	Taupo	None	1.718	-38.347	177.8791	1.053	1.055
zz	Pit	0.15	Taupo	Whakatane	1.718	-38.352	177.8796	1.022	1.027
aaa	Pit	>0.2	None	None	0	-38.357	177.8798	1.076	1.076
bbb	Pit	>0.2	None	None	0	-38.357	177.8801	1.078	1.075
ccc	Pit	0.13	None	Waimihia	0	-38.355	177.8801	1.044	1.045
ddd	Pit	0.1	Taupo	None	1.718	-38.358	177.8801	1.070	1.078
eee	Pit	<0.05	None	None	0	-38.346	177.8803	1.065	1.062
fff	Pit/Auger	0.4	Waimihia	None	3.401	-38.354	177.8804	1.159	1.179
ggg	Pit	0.16	Waimihia	Rotoma	3.401	-38.342	177.8807	1.013	1.017
hhh	Pit	0.4	Taupo	Whakatane	1.718	-38.352	177.881	1.024	1.036
iii	Pit	<0.01	None	Waimihia	0	-38.346	177.8812	1.049	1.043
jjj	Pit	<0.01	None	None	0	-38.338	177.8817	1.093	1.119
kkk	Pit	0.18	Waimihia	None	3.401	-38.343	177.8818	1.077	1.082
lll	Pit	>0.1	None	Waimihia	0	-38.356	177.8819	1.035	1.044
mmm	Auger	0.4	Taupo	Whakatane	1.718	-38.354	177.882	1.031	1.032
nnn	Cut	<0.2	Waimihia	None	3.401	-38.348	177.8831	1.171	1.166
ooo	Auger	0.35	Waimihia	None	3.401	-38.355	177.8833	1.049	1.055
ppp	Pit	0.15	Waimihia	None	3.401	-38.348	177.8851	1.087	1.082
qqq	Cut	<0.2	Waimihia	None	3.401	-38.349	177.8873	1.073	1.069

Table B3. DFA Reference Dataset and Results

Sample Source[a]	Tephra	Source	DFA Predicted Source	Code	DFA Predicted Tephra	Incorrect Source?	Incorrect Tephra?
Puck 17-3	Kawakawa	Taupo	Taupo	Kw	Kw		
Puck 17-3	Kawakawa	Taupo	Taupo	Kw	Kw		
Puck 17-3	Kawakawa	Taupo	Taupo	Kw	Kw		
Puck 17-3	Kawakawa	Taupo	Taupo	Kw	Kw		
Puck 17-3	Kawakawa	Taupo	Okataina	Kw	Kw	yes	
Puck 17-3	Kawakawa	Taupo	Taupo	Kw	Kw		
Puck 17-3	Kawakawa	Taupo	Taupo	Kw	Kw		
Puck 17-3	Kawakawa	Taupo	Taupo	Kw	Kw		
Puck 17-3	Kawakawa	Taupo	Taupo	Kw	Kw		
Puck 17-3	Kawakawa (avg)	Taupo	Taupo	Kw	Kw		
Allan2008	Kawakawa AT331	Taupo	Okataina	Kw	Kw	yes	
Allan2008	Kawakawa Kk1	Taupo	Okataina	Kw	Kw	yes	
Bilderback2012	Kawakawa	Taupo	Taupo	Kw	Kw		
Bilderback2012	Kawakawa	Taupo	Taupo	Kw	Kw		
Bilderback2012	Kawakawa	Taupo	Okataina	Kw	Kw	yes	
Bilderback2012	Kawakawa	Taupo	Okataina	Kw	Kw	yes	
Bilderback2012	Kawakawa	Taupo	Taupo	Kw	Kw		
Bilderback2012	Kawakawa	Taupo	Okataina	Kw	Kw	yes	
Bilderback2012	Kawakawa	Taupo	Taupo	Kw	Kw		
Bilderback2012	Kawakawa	Taupo	Okataina	Kw	Kw	yes	
Bilderback2012	Kawakawa	Taupo	Taupo	Kw	Kw		
Bilderback2012	Kawakawa	Taupo	Okataina	Kw	Kw	yes	
Bilderback2012	Kawakawa	Taupo	Okataina	Kw	Kw	yes	
Bilderback2012	Kawakawa	Taupo	Taupo	Kw	Kw		
Bilderback2012	Kawakawa	Taupo	Taupo	Kw	Kw		
Bilderback2012	Kawakawa	Taupo	Taupo	Kw	Kw		
Bilderback2012	Kawakawa	Taupo	Okataina	Kw	Kw	yes	
Lowe2008	Kawakawa	Taupo	Okataina	Kw	Kw	yes	
Puck 19-2	Opepe	Taupo	Taupo	Op	Op		
Puck 19-2	Opepe	Taupo	Taupo	Op	Op		
Puck 19-2	Opepe	Taupo	Taupo	Op	Op		
Puck 19-2	Opepe	Taupo	Taupo	Op	Op		
Puck 19-2	Opepe	Taupo	Taupo	Op	Op		
Puck 19-2	Opepe	Taupo	Taupo	Op	Op		
Puck 19-2	Opepe	Taupo	Taupo	Op	P/K		yes
Puck 19-2	Opepe	Taupo	Taupo	Op	Op		
Puck 19-2	Opepe (avg)	Taupo	Taupo	Op	Op		
Bilderback2012	Opepe (avg)	Taupo	Taupo	Op	Op		
Bilderback2012	Opepe	Taupo	Taupo	Op	Op		
Bilderback2012	Opepe	Taupo	Taupo	Op	Op		
Bilderback2012	Opepe	Taupo	Taupo	Op	Op		
Bilderback2012	Opepe	Taupo	Taupo	Op	Op		
Bilderback2012	Opepe	Taupo	Taupo	Op	Op		

Table B3. (continued)

Sample Source[a]	Tephra	Source	DFA Predicted Source	Code	DFA Predicted Tephra	Incorrect Source?	Incorrect Tephra?
Bilderback2012	Opepe	Taupo	Taupo	Op	Op		
Bilderback2012	Opepe	Taupo	Taupo	Op	Op		
Bilderback2012	Opepe	Taupo	Taupo	Op	Op		
Bilderback2012	Opepe	Taupo	Taupo	Op	Op		
Bilderback2012	Opepe	Taupo	Taupo	Op	Op		
Bilderback2012	Opepe	Taupo	Taupo	Op	Op		
Bilderback2012	Opepe	Taupo	Taupo	Op	P/K		yes
Smith2005	Opepe	Taupo	Taupo	Op	Op		
Puck 19-3	Poronui	Taupo	Taupo	P/K	P/K		
Puck 19-3	Poronui	Taupo	Taupo	P/K	P/K		
Puck 19-3	Poronui	Taupo	Taupo	P/K	P/K		
Puck 19-3	Poronui	Taupo	Taupo	P/K	P/K		
Puck 19-3	Poronui	Taupo	Taupo	P/K	P/K		
Puck 19-3	Poronui	Taupo	Taupo	P/K	P/K		
Puck 19-3	Poronui	Taupo	Taupo	P/K	P/K		
Puck 19-3	Poronui (avg)	Taupo	Taupo	P/K	P/K		
Puck 19-4	Karapiti	Taupo	Taupo	P/K	Op		yes
Puck 19-4	Karapiti	Taupo	Taupo	P/K	P/K		
Puck 19-4	Karapiti	Taupo	Taupo	P/K	Wm		yes
Puck 19-4	Karapiti	Taupo	Taupo	P/K	P/K		
Puck 19-4	Karapiti	Taupo	Taupo	P/K	P/K		
Puck 19-4	Karapiti	Taupo	Taupo	P/K	Op		yes
Puck 19-4	Karapiti	Taupo	Taupo	P/K	P/K		
Puck 19-4	Karapiti (avg)	Taupo	Taupo	P/K	Op		yes
Bilderback2012	Poronui (avg)	Taupo	Taupo	P/K	P/K		
Bilderback2012	Karapiti (avg)	Taupo	Taupo	P/K	P/K		
Bilderback2012	Poronui	Taupo	Taupo	P/K	P/K		
Bilderback2012	Poronui	Taupo	Taupo	P/K	P/K		
Bilderback2012	Poronui	Taupo	Taupo	P/K	P/K		
Bilderback2012	Poronui	Taupo	Taupo	P/K	P/K		
Bilderback2012	Poronui	Taupo	Taupo	P/K	P/K		
Bilderback2012	Poronui	Taupo	Taupo	P/K	P/K		
Bilderback2012	Poronui	Taupo	Taupo	P/K	P/K		
Bilderback2012	Poronui	Taupo	Taupo	P/K	P/K		
Bilderback2012	Poronui	Taupo	Taupo	P/K	P/K		
Bilderback2012	Poronui	Taupo	Taupo	P/K	P/K		
Bilderback2012	Poronui	Taupo	Taupo	P/K	P/K		
Bilderback2012	Karapiti	Taupo	Taupo	P/K	P/K		
Bilderback2012	Karapiti	Taupo	Taupo	P/K	P/K		
Bilderback2012	Karapiti	Taupo	Taupo	P/K	P/K		
Bilderback2012	Karapiti	Taupo	Taupo	P/K	P/K		
Bilderback2012	Karapiti	Taupo	Taupo	P/K	P/K		
Bilderback2012	Karapiti	Taupo	Taupo	P/K	P/K		

Table B3. (continued)

Sample Source[a]	Tephra	Source	DFA Predicted Source	Code	DFA Predicted Tephra	Incorrect Source?	Incorrect Tephra?
Bilderback2012	Karapiti	Taupo	Taupo	P/K	P/K		
Bilderback2012	Karapiti	Taupo	Taupo	P/K	P/K		
Bilderback2012	Karapiti	Taupo	Taupo	P/K	Op		yes
Bilderback2012	Karapiti	Taupo	Taupo	P/K	P/K		
Bilderback2012	Karapiti	Taupo	Taupo	P/K	Op		yes
Bilderback2012	Karapiti	Taupo	Taupo	P/K	P/K		
Bilderback2012	Karapiti	Taupo	Taupo	P/K	P/K		
Bilderback2012	Karapiti	Taupo	Taupo	P/K	P/K		
Smith2005	Poronui	Taupo	Taupo	P/K	P/K		
Smith2005	Karapiti	Taupo	Taupo	P/K	P/K		
Bilderback2012	Taupo (avg)	Taupo	Taupo	Tp	Tp		
Bilderback2012	Taupo	Taupo	Taupo	Tp	Tp		
Bilderback2012	Taupo	Taupo	Taupo	Tp	Tp		
Bilderback2012	Taupo	Taupo	Taupo	Tp	Tp		
Lowe2008	Taupo	Taupo	Taupo	Tp	Tp		
Puck 19-1	Waimihia	Taupo	Taupo	Wm	Wm		
Puck 19-1	Waimihia	Taupo	Taupo	Wm	Wm		
Puck 19-1	Waimihia	Taupo	Taupo	Wm	Wm		
Puck 19-1	Waimihia	Taupo	Taupo	Wm	Wm		
Puck 19-1	Waimihia	Taupo	Taupo	Wm	Wm		
Puck 19-1	Waimihia	Taupo	Taupo	Wm	Wm		
Puck 19-1	Waimihia	Taupo	Taupo	Wm	Wm		
Puck 19-1	Waimihia	Taupo	Taupo	Wm	Wm		
Puck 19-1	Waimihia (avg)	Taupo	Taupo	Wm	Wm		
Bilderback2012	Waimihia (avg)	Taupo	Taupo	Wm	Wm		
Bilderback2012	Waimihia	Taupo	Taupo	Wm	Wm		
Bilderback2012	Waimihia	Taupo	Taupo	Wm	Wm		
Bilderback2012	Waimihia	Taupo	Taupo	Wm	Wm		
Bilderback2012	Waimihia	Taupo	Taupo	Wm	Wm		
Bilderback2012	Waimihia	Taupo	Taupo	Wm	Wm		
Bilderback2012	Waimihia	Taupo	Taupo	Wm	Wm		
Bilderback2012	Waimihia	Taupo	Taupo	Wm	Wm		
Bilderback2012	Waimihia	Taupo	Taupo	Wm	Wm		
Bilderback2012	Waimihia	Taupo	Taupo	Wm	Wm		
Bilderback2012	Waimihia	Taupo	Taupo	Wm	Wm		
Bilderback2012	Waimihia	Taupo	Taupo	Wm	Wm		
Bilderback2012	Waimihia	Taupo	Taupo	Wm	Wm		
Bilderback2012	Waimihia	Taupo	Taupo	Wm	Wm		
Bilderback2012	Waimihia	Taupo	Taupo	Wm	Wm		
Bilderback2012	Waimihia	Taupo	Taupo	Wm	Wm		
Bilderback2012	Waimihia	Taupo	Taupo	Wm	Wm		
Bilderback2012	Waimihia	Taupo	Taupo	Wm	Wm		
Bilderback2012	Waimihia	Taupo	Taupo	Wm	Wm		
Bilderback2012	Waimihia	Taupo	Taupo	Wm	Wm		
Bilderback2012	Waimihia	Taupo	Taupo	Wm	Wm		
Bilderback2012	Waimihia	Taupo	Taupo	Wm	Wm		
Bilderback2012	Waimihia	Taupo	Taupo	Wm	Wm		
Bilderback2012	Waimihia	Taupo	Taupo	Wm	Wm		
Bilderback2012	Waimihia	Taupo	Taupo	Wm	Wm		
Bilderback2012	Waimihia	Taupo	Taupo	Wm	Wm		
Bilderback2012	Waimihia	Taupo	Taupo	Wm	Wm		
Bilderback2012	Waimihia	Taupo	Taupo	Wm	Wm		
Smith2005	Waimihia	Taupo	Taupo	Wm	Wm		
Bilderback2012	Kaharoa bottom (avg)	Okataina	Okataina	Kh	Kh		
Bilderback2012	Kaharoa top (avg)	Okataina	Okataina	Kh	Kh		
Bilderback2012	Kaharoa bottom	Okataina	Okataina	Kh	Kh		

Table B3. (continued)

Sample Source[a]	Tephra	Source	DFA Predicted Source	Code	DFA Predicted Tephra	Incorrect Source?	Incorrect Tephra?
Bilderback2012	Kaharoa bottom	Okataina	Okataina	Kh	Kh		
Bilderback2012	Kaharoa bottom	Okataina	Okataina	Kh	Kh		
Bilderback2012	Kaharoa bottom	Okataina	Okataina	Kh	Kh		
Bilderback2012	Kaharoa bottom	Okataina	Okataina	Kh	Kh		
Bilderback2012	Kaharoa bottom	Okataina	Okataina	Kh	Kh		
Bilderback2012	Kaharoa bottom	Okataina	Okataina	Kh	Kh		
Bilderback2012	Kaharoa bottom	Okataina	Okataina	Kh	Kh		
Bilderback2012	Kaharoa bottom	Okataina	Okataina	Kh	Kh		
Bilderback2012	Kaharoa bottom	Okataina	Okataina	Kh	Kh		
Bilderback2012	Kaharoa bottom	Okataina	Okataina	Kh	Kh		
Bilderback2012	Kaharoa bottom	Okataina	Okataina	Kh	Kh		
Bilderback2012	Kaharoa top	Okataina	Okataina	Kh	Kh		
Bilderback2012	Kaharoa top	Okataina	Okataina	Kh	Kh		
Bilderback2012	Kaharoa top	Okataina	Okataina	Kh	Kh		
Bilderback2012	Kaharoa top	Okataina	Okataina	Kh	Kh		
Bilderback2012	Kaharoa top	Okataina	Okataina	Kh	Kh		
Bilderback2012	Kaharoa top	Okataina	Okataina	Kh	Kh		
Bilderback2012	Kaharoa top	Okataina	Okataina	Kh	Kh		
Bilderback2012	Kaharoa top	Okataina	Okataina	Kh	Kh		
Bilderback2012	Kaharoa top	Okataina	Okataina	Kh	Kh		
Bilderback2012	Kaharoa top	Okataina	Okataina	Kh	Kh		
Bilderback2012	Kaharoa top	Okataina	Okataina	Kh	Kh		
Smith2005	Kaharoa T2	Okataina	Okataina	Kh	Kh		
Smith2005	Kaharoa T1	Okataina	Okataina	Kh	Kh		
Bilderback2012	Mamaku (avg)	Okataina	Okataina	Ma	Kh		yes
Bilderback2012	Mamaku	Okataina	Okataina	Ma	Kh		yes
Bilderback2012	Mamaku	Okataina	Okataina	Ma	Kh		yes
Bilderback2012	Mamaku	Okataina	Okataina	Ma	Kh		yes
Bilderback2012	Mamaku	Okataina	Okataina	Ma	Kh		yes
Bilderback2012	Mamaku	Okataina	Okataina	Ma	Kh		yes
Bilderback2012	Mamaku	Okataina	Okataina	Ma	Rh		yes
Bilderback2012	Mamaku	Okataina	Okataina	Ma	Kh		yes
Bilderback2012	Mamaku	Okataina	Okataina	Ma	Kh		yes
Bilderback2012	Mamaku	Okataina	Okataina	Ma	Kh		yes
Bilderback2012	Mamaku	Okataina	Okataina	Ma	Kh		yes
Smith2006	Mamaku	Okataina	Okataina	Ma	Ma		
Smith2006	Mamaku	Okataina	Okataina	Ma	Ma		
Smith2006	Mamaku	Okataina	Okataina	Ma	Ma		
Smith2006	Mamaku	Okataina	Okataina	Ma	Ma		
Smith2006	Mamaku	Okataina	Okataina	Ma	Ma		
Smith2006	Mamaku	Okataina	Okataina	Ma	Ma		
Smith2006	Mamaku	Okataina	Okataina	Ma	Ma		
Smith2006	Mamaku	Okataina	Okataina	Ma	Ma		

Table B3. (continued)

Sample Source[a]	Tephra	Source	DFA Predicted Source	Code	DFA Predicted Tephra	Incorrect Source?	Incorrect Tephra?
Smith2006	Mamaku	Okataina	Okataina	Ma	Ma		
Smith2006	Mamaku	Okataina	Okataina	Ma	Ma		
Smith2006	Mamaku	Okataina	Okataina	Ma	Ma		
Smith2006	Mamaku	Okataina	Okataina	Ma	Ma		
Smith2006	Mamaku	Okataina	Okataina	Ma	Ma		
Smith2006	Mamaku	Okataina	Okataina	Ma	Ma		
Wright2000	Mamaku	Okataina	Okataina	Ma	Ma		
Bilderback2012	Mangaone (avg)	Okataina	Okataina	Mg	Mg		
Bilderback2012	Mangaone	Okataina	Okataina	Mg	Mg		
Bilderback2012	Mangaone	Okataina	Okataina	Mg	Mg		
Bilderback2012	Mangaone	Okataina	Okataina	Mg	Mg		
Bilderback2012	Mangaone	Okataina	Okataina	Mg	Mg		
Bilderback2012	Mangaone	Okataina	Okataina	Mg	Mg		
Bilderback2012	Mangaone	Okataina	Okataina	Mg	Mg		
Bilderback2012	Mangaone	Okataina	Okataina	Mg	Mg		
Bilderback2012	Mangaone	Okataina	Okataina	Mg	Mg		
Bilderback2012	Mangaone	Okataina	Okataina	Mg	Mg		
Bilderback2012	Mangaone	Okataina	Okataina	Mg	Mg		
Bilderback2012	Mangaone	Okataina	Okataina	Mg	Ru		yes
Bilderback2012	Mangaone	Okataina	Okataina	Mg	Mg		
Bilderback2012	Mangaone	Okataina	Okataina	Mg	Mg		
Puck 17-1	Okatainaareka (avg)	Okataina	Okataina	Okataina	Okataina		
Puck 17-2	Okatainaareka	Okataina	Okataina	Okataina	Okataina		
Puck 17-2	Okatainaareka	Okataina	Okataina	Okataina	Ta		yes
Puck 17-2	Okatainaareka	Okataina	Okataina	Okataina	Okataina		
Puck 17-2	Okatainaareka	Okataina	Okataina	Okataina	Ta		yes
Puck 17-2	Okatainaareka	Okataina	Okataina	Okataina	Okataina		
Puck 17-2	Okatainaareka	Okataina	Okataina	Okataina	Okataina		
Puck 17-2	Okatainaareka	Okataina	Okataina	Okataina	Om		yes
Puck 17-2	Okatainaareka	Okataina	Okataina	Okataina	Okataina		
Puck 17-2	Okatainaareka	Okataina	Okataina	Okataina	Okataina		
Bilderback2012	Okatainaareka (avg)	Okataina	Okataina	Okataina	Re		yes
Bilderback2012	Okatainaareka	Okataina	Okataina	Okataina	Re		yes
Bilderback2012	Okatainaareka	Okataina	Okataina	Okataina	Re		yes
Bilderback2012	Okatainaareka	Okataina	Okataina	Okataina	Re		yes
Bilderback2012	Okatainaareka	Okataina	Okataina	Okataina	Re		yes
Bilderback2012	Okatainaareka	Okataina	Okataina	Okataina	Re		yes
Bilderback2012	Okatainaareka	Okataina	Okataina	Okataina	Re		yes
Bilderback2012	Okatainaareka	Okataina	Okataina	Okataina	Re		yes
Bilderback2012	Okatainaareka	Okataina	Okataina	Okataina	Re		yes
Bilderback2012	Okatainaareka	Okataina	Okataina	Okataina	Okataina		
Smith2005	Okatainaareka T1	Okataina	Okataina	Okataina	Wk		yes
Smith2005	Okatainaareka T2	Okataina	Okataina	Okataina	Okataina		
Smith2005	Okatainaareka T3	Okataina	Okataina	Okataina	Okataina		

Table B3. (continued)

Sample Source[a]	Tephra	Source	DFA Predicted Source	Code	DFA Predicted Tephra	Incorrect Source?	Incorrect Tephra?
Allan2008	Omataroa AT332	Okataina	Okataina	Om	Om		
Allan2008	Omataroa AT376	Okataina	Okataina	Om	Om		
Allan2008	Omataroa A9	Okataina	Okataina	Om	Om		
Allan2008	Omataroa A10	Okataina	Okataina	Om	Om		
Smith2005	Omataroa	Okataina	Taupo	Om	Om	yes	
Puck 17-1	Rerewhakaaitu (avg)	Okataina	Okataina	Re	Okataina		yes
Puck 17-1	Rerewhakaaitu	Okataina	Okataina	Re	Okataina		yes
Puck 17-1	Rerewhakaaitu	Okataina	Okataina	Re	Okataina		yes
Puck 17-1	Rerewhakaaitu	Okataina	Okataina	Re	Okataina		yes
Puck 17-1	Rerewhakaaitu	Okataina	Okataina	Re	Okataina		yes
Puck 17-1	Rerewhakaaitu	Okataina	Okataina	Re	Okataina		yes
Puck 17-1	Rerewhakaaitu	Okataina	Okataina	Re	Okataina		yes
Puck 17-1	Rerewhakaaitu	Okataina	Okataina	Re	Okataina		yes
Puck 17-1	Rerewhakaaitu	Okataina	Okataina	Re	Okataina		yes
Puck 17-1	Rerewhakaaitu	Okataina	Okataina	Re	Ta		yes
Bilderback2012	Rerewhakaaitu bottom (avg)	Okataina	Okataina	Re	Re		
Bilderback2012	Rerewhakaaitu middle (avg)	Okataina	Okataina	Re	Re		
Bilderback2012	Rerewhakaaitu top (avg)	Okataina	Okataina	Re	Re		
Bilderback2012	Rerewhakaaitu bottom	Okataina	Okataina	Re	Wa		yes
Bilderback2012	Rerewhakaaitu bottom	Okataina	Okataina	Re	Re		
Bilderback2012	Rerewhakaaitu bottom	Okataina	Okataina	Re	Wa		yes
Bilderback2012	Rerewhakaaitu bottom	Okataina	Okataina	Re	Re		
Bilderback2012	Rerewhakaaitu bottom	Okataina	Okataina	Re	Ru		yes
Bilderback2012	Rerewhakaaitu bottom	Okataina	Okataina	Re	Re		
Bilderback2012	Rerewhakaaitu bottom	Okataina	Okataina	Re	Wa		yes
Bilderback2012	Rerewhakaaitu bottom	Okataina	Okataina	Re	Wa		yes
Bilderback2012	Rerewhakaaitu bottom	Okataina	Okataina	Re	Re		
Bilderback2012	Rerewhakaaitu bottom	Okataina	Okataina	Re	Wa		yes
Bilderback2012	Rerewhakaaitu middle	Okataina	Okataina	Re	Wa		yes
Bilderback2012	Rerewhakaaitu middle	Okataina	Okataina	Re	Wa		yes
Bilderback2012	Rerewhakaaitu middle	Okataina	Okataina	Re	Wa		yes
Bilderback2012	Rerewhakaaitu middle	Okataina	Okataina	Re	Wa		yes
Bilderback2012	Rerewhakaaitu middle	Okataina	Okataina	Re	Wa		yes
Bilderback2012	Rerewhakaaitu middle	Okataina	Okataina	Re	Re		
Bilderback2012	Rerewhakaaitu middle	Okataina	Okataina	Re	Re		
Bilderback2012	Rerewhakaaitu middle	Okataina	Okataina	Re	Wa		yes
Bilderback2012	Rerewhakaaitu middle	Okataina	Okataina	Re	Wa		yes
Bilderback2012	Rerewhakaaitu middle	Okataina	Okataina	Re	Ru		yes
Bilderback2012	Rerewhakaaitu middle	Okataina	Okataina	Re	Wa		yes
Bilderback2012	Rerewhakaaitu top	Okataina	Okataina	Re	Re		
Bilderback2012	Rerewhakaaitu top	Okataina	Okataina	Re	Wa		yes
Bilderback2012	Rerewhakaaitu top	Okataina	Okataina	Re	Wa		yes
Bilderback2012	Rerewhakaaitu top	Okataina	Okataina	Re	Ta		yes
Bilderback2012	Rerewhakaaitu top	Okataina	Okataina	Re	Wa		yes

Table B3. (continued)

Sample Source[a]	Tephra	Source	DFA Predicted Source	Code	DFA Predicted Tephra	Incorrect Source?	Incorrect Tephra?
Bilderback2012	Rerewhakaaitu top	Okataina	Okataina	Re	Ta		yes
Bilderback2012	Rerewhakaaitu top	Okataina	Okataina	Re	Ta		yes
Bilderback2012	Rerewhakaaitu top	Okataina	Okataina	Re	Re		
Bilderback2012	Rerewhakaaitu top	Okataina	Okataina	Re	Wa		yes
Bilderback2012	Rerewhakaaitu top	Okataina	Okataina	Re	Re		
Bilderback2012	Rerewhakaaitu top	Okataina	Okataina	Re	Ta		yes
Lowe2008	Rerewhakaaitu T1	Okataina	Okataina	Re	Ma		yes
Lowe2008	Rerewhakaaitu T2	Okataina	Okataina	Re	Okataina		yes
Lowe2008	Rerewhakaaitu T3	Okataina	Okataina	Re	Wa		yes
Bilderback2012	Rotoehu (avg)	Okataina	Okataina	Rh	Rh		
Bilderback2012	Rotoehu	Okataina	Okataina	Rh	Rh		
Bilderback2012	Rotoehu	Okataina	Okataina	Rh	Rh		
Bilderback2012	Rotoehu	Okataina	Okataina	Rh	Wa		yes
Bilderback2012	Rotoehu	Okataina	Okataina	Rh	Rh		
Bilderback2012	Rotoehu	Okataina	Okataina	Rh	Rh		
Bilderback2012	Rotoehu	Okataina	Okataina	Rh	Rh		
Bilderback2012	Rotoehu	Okataina	Okataina	Rh	Rh		
Bilderback2012	Rotoehu	Okataina	Okataina	Rh	Rh		
Bilderback2012	Rotoehu	Okataina	Okataina	Rh	Rh		
Bilderback2012	Rotoehu	Okataina	Okataina	Rh	Rh		
Bilderback2012	Rotoehu	Okataina	Okataina	Rh	Rh		
Bilderback2012	Rotoehu	Okataina	Okataina	Rh	Rh		
Bilderback2012	Rotoehu	Okataina	Okataina	Rh	Rh		
Bilderback2012	Rotoehu	Okataina	Okataina	Rh	Rh		
Bilderback2012	Rotoehu	Okataina	Okataina	Rh	Rh		
Bilderback2012	Rotoehu	Okataina	Okataina	Rh	Rh		
Bilderback2012	Rotoehu	Okataina	Okataina	Rh	Rh		
Bilderback2012	Rotoehu	Okataina	Okataina	Rh	Rh		
Bilderback2012	Rotoma bottom (avg)	Okataina	Okataina	Ro	Rh		yes
Bilderback2012	Rotoma top (avg)	Okataina	Okataina	Ro	Rh		yes
Bilderback2012	Rotoma T1	Okataina	Okataina	Ro	Rh		yes
Bilderback2012	Rotoma T1	Okataina	Okataina	Ro	Rh		yes
Bilderback2012	Rotoma T1	Okataina	Okataina	Ro	Rh		yes
Bilderback2012	Rotoma T1	Okataina	Okataina	Ro	Rh		yes
Bilderback2012	Rotoma T1	Okataina	Okataina	Ro	Rh		yes
Bilderback2012	Rotoma T1	Okataina	Okataina	Ro	Rh		yes
Bilderback2012	Rotoma T1	Okataina	Okataina	Ro	Ro		
Bilderback2012	Rotoma T1	Okataina	Okataina	Ro	Ro		
Bilderback2012	Rotoma T1	Okataina	Okataina	Ro	Rh		yes
Bilderback2012	Rotoma T1	Okataina	Okataina	Ro	Ro		
Bilderback2012	Rotoma T1	Okataina	Okataina	Ro	Rh		yes
Bilderback2012	Rotoma T2	Okataina	Okataina	Ro	Rh		yes
Bilderback2012	Rotoma T2	Okataina	Okataina	Ro	Ro		
Bilderback2012	Rotoma T2	Okataina	Okataina	Ro	Ro		

Table B3. (continued)

Sample Source[a]	Tephra	Source	DFA Predicted Source	Code	DFA Predicted Tephra	Incorrect Source?	Incorrect Tephra?
Bilderback2012	Rotoma T2	Okataina	Okataina	Ro	Rh		yes
Bilderback2012	Rotoma T2	Okataina	Okataina	Ro	Rh		yes
Bilderback2012	Rotoma T2	Okataina	Okataina	Ro	Rh		yes
Bilderback2012	Rotoma T2	Okataina	Okataina	Ro	Rh		yes
Bilderback2012	Rotoma T2	Okataina	Okataina	Ro	Ro		
Bilderback2012	Rotoma T2	Okataina	Okataina	Ro	Rh		yes
Bilderback2012	Rotoma T2	Okataina	Okataina	Ro	Ro		
Bilderback2012	Rotoma T2	Okataina	Okataina	Ro	Rh		yes
Bilderback2012	Rotoma T2	Okataina	Okataina	Ro	Rh		yes
Smith2005	Rotoma T1	Okataina	Okataina	Ro	Wk		yes
Smith2005	Rotoma T2	Okataina	Okataina	Ro	Wk		yes
Smith2005	Rotoma T3	Okataina	Okataina	Ro	Wk		yes
Smith2006	Rotoma T1	Okataina	Okataina	Ro	Ro		
Smith2006	Rotoma T3	Okataina	Okataina	Ro	Wk		yes
Smith2006	Rotoma T1	Okataina	Okataina	Ro	Ro		
Smith2006	Rotoma T2	Okataina	Okataina	Ro	Wk		yes
Smith2006	Rotoma T1	Okataina	Okataina	Ro	Wk		yes
Smith2006	Rotoma T1	Okataina	Okataina	Ro	Ro		
Smith2006	Rotoma T1	Okataina	Okataina	Ro	Wk		yes
Smith2006	Rotoma T1	Okataina	Okataina	Ro	Wk		yes
Smith2006	Rotoma T1	Okataina	Okataina	Ro	Wk		yes
Smith2006	Rotoma T1	Okataina	Okataina	Ro	Wk		yes
Smith2006	Rotoma T1	Okataina	Okataina	Ro	Wk		yes
Smith2006	Rotoma T2	Okataina	Okataina	Ro	Ro		
Smith2006	Rotoma T2	Okataina	Okataina	Ro	Wk		yes
Smith2006	Rotoma T3	Okataina	Okataina	Ro	Wk		yes
Smith2006	Rotoma T3	Okataina	Okataina	Ro	Wk		yes
Bilderback2012	Rotorua (avg)	Okataina	Okataina	Ru	Ru		
Bilderback2012	Rotorua	Okataina	Taupo	Ru	Ru	yes	
Bilderback2012	Rotorua	Okataina	Okataina	Ru	Re		yes
Bilderback2012	Rotorua	Okataina	Okataina	Ru	Re		yes
Bilderback2012	Rotorua	Okataina	Okataina	Ru	Ru		
Bilderback2012	Rotorua	Okataina	Okataina	Ru	Ru		
Bilderback2012	Rotorua	Okataina	Okataina	Ru	Ta		yes
Bilderback2012	Rotorua	Okataina	Okataina	Ru	Ta		yes
Bilderback2012	Rotorua	Okataina	Okataina	Ru	Ru		
Bilderback2012	Rotorua	Okataina	Okataina	Ru	Ta		yes
Bilderback2012	Rotorua	Okataina	Okataina	Ru	Mg		yes
Bilderback2012	Rotorua	Okataina	Okataina	Ru	Ru		
Bilderback2012	Rotorua	Okataina	Okataina	Ru	Re		yes
Bilderback2012	Rotorua	Okataina	Okataina	Ru	Re		yes
Lowe2008	Rotorua T2	Okataina	Okataina	Ru	Okataina		yes
Smith2005	Rotorua T1	Okataina	Okataina	Ru	Ru		
Puck 17-1	Tarawera (avg)	Okataina	Okataina	Ta	Ta		

Table B3. (continued)

Sample Source[a]	Tephra	Source	DFA Predicted Source	Code	DFA Predicted Tephra	Incorrect Source?	Incorrect Tephra?
Puck 17-4	Tarawera	Okataina	Okataina	Ta	Ro		yes
Puck 17-4	Tarawera	Okataina	Okataina	Ta	Ta		
Puck 17-4	Tarawera	Okataina	Okataina	Ta	Ta		
Puck 17-4	Tarawera	Okataina	Okataina	Ta	Rh		yes
Puck 17-4	Tarawera	Okataina	Okataina	Ta	Ta		
Puck 17-4	Tarawera	Okataina	Okataina	Ta	Ta		
Puck 17-4	Tarawera	Okataina	Okataina	Ta	Ta		
Puck 17-4	Tarawera	Okataina	Okataina	Ta	Ta		
Puck 17-4	Tarawera	Okataina	Okataina	Ta	Ru		yes
Bilderback2012	Tarawera (avg)	Okataina	Okataina	Ta	Re		yes
Bilderback2012	Tarawera	Okataina	Okataina	Ta	Re		yes
Bilderback2012	Tarawera	Okataina	Okataina	Ta	Kh		yes
Bilderback2012	Tarawera	Okataina	Okataina	Ta	Kh		yes
Bilderback2012	Tarawera	Okataina	Okataina	Ta	Kh		yes
Bilderback2012	Tarawera	Okataina	Okataina	Ta	Ta		
Bilderback2012	Tarawera	Okataina	Okataina	Ta	Re		yes
Bilderback2012	Tarawera	Okataina	Okataina	Ta	Kh		yes
Bilderback2012	Tarawera	Okataina	Okataina	Ta	Re		yes
Bilderback2012	Tarawera	Okataina	Okataina	Ta	Re		yes
Bilderback2012	TeRere (avg)	Okataina	Okataina	Te	Te		
Bilderback2012	TeRere	Okataina	Okataina	Te	Te		
Bilderback2012	TeRere	Okataina	Okataina	Te	Te		
Bilderback2012	TeRere	Okataina	Okataina	Te	Te		
Bilderback2012	TeRere	Okataina	Okataina	Te	Te		
Bilderback2012	TeRere	Okataina	Okataina	Te	Te		
Bilderback2012	TeRere	Okataina	Okataina	Te	Te		
Bilderback2012	TeRere	Okataina	Okataina	Te	Te		
Bilderback2012	TeRere	Okataina	Okataina	Te	Rh		yes
Bilderback2012	TeRere	Okataina	Okataina	Te	Te		
Bilderback2012	TeRere	Okataina	Okataina	Te	Te		
Bilderback2012	TeRere	Okataina	Okataina	Te	Te		
Bilderback2012	TeRere	Okataina	Okataina	Te	Te		
Bilderback2012	TeRere	Okataina	Okataina	Te	Te		
Bilderback2012	TeRere	Okataina	Okataina	Te	Te		
Smith2005	TeRere T1	Okataina	Okataina	Te	Te		
Smith2005	TeRere T2	Okataina	Okataina	Te	Okataina		yes
Smith2005	TeRere T3	Okataina	Okataina	Te	Te		
Bilderback2012	Waiohau bottom (avg)	Okataina	Okataina	Wa	Wa		
Bilderback2012	Waiohau middle (avg)	Okataina	Okataina	Wa	Wa		
Bilderback2012	Waiohau top (avg)	Okataina	Okataina	Wa	Wa		
Bilderback2012	Waiohau bottom	Okataina	Okataina	Wa	Wa		
Bilderback2012	Waiohau bottom	Okataina	Okataina	Wa	Wa		
Bilderback2012	Waiohau bottom	Okataina	Okataina	Wa	Wa		
Bilderback2012	Waiohau bottom	Okataina	Okataina	Wa	Wa		

Table B3. (continued)

Sample Source[a]	Tephra	Source	DFA Predicted Source	Code	DFA Predicted Tephra	Incorrect Source?	Incorrect Tephra?
Bilderback2012	Waiohau bottom	Okataina	Okataina	Wa	Wa		
Bilderback2012	Waiohau bottom	Okataina	Okataina	Wa	Wa		
Bilderback2012	Waiohau bottom	Okataina	Okataina	Wa	Wa		
Bilderback2012	Waiohau middle	Okataina	Okataina	Wa	Wa		
Bilderback2012	Waiohau middle	Okataina	Okataina	Wa	Rh		yes
Bilderback2012	Waiohau middle	Okataina	Okataina	Wa	Wa		
Bilderback2012	Waiohau middle	Okataina	Okataina	Wa	Wa		
Bilderback2012	Waiohau middle	Okataina	Okataina	Wa	Wa		
Bilderback2012	Waiohau middle	Okataina	Okataina	Wa	Wa		
Bilderback2012	Waiohau middle	Okataina	Okataina	Wa	Wa		
Bilderback2012	Waiohau middle	Okataina	Okataina	Wa	Wa		
Bilderback2012	Waiohau middle	Okataina	Okataina	Wa	Wa		
Bilderback2012	Waiohau top	Okataina	Okataina	Wa	Rh		yes
Bilderback2012	Waiohau top	Okataina	Okataina	Wa	Wa		
Bilderback2012	Waiohau top	Okataina	Okataina	Wa	Wa		
Bilderback2012	Waiohau top	Okataina	Okataina	Wa	Wa		
Bilderback2012	Waiohau top	Okataina	Okataina	Wa	Wa		
Bilderback2012	Waiohau top	Okataina	Okataina	Wa	Wa		
Bilderback2012	Waiohau top	Okataina	Okataina	Wa	Wa		
Bilderback2012	Waiohau top	Okataina	Okataina	Wa	Wa		
Bilderback2012	Waiohau top	Okataina	Okataina	Wa	Wa		
Bilderback2012	Waiohau top	Okataina	Okataina	Wa	Wa		
Smith2005	Waiohau	Okataina	Okataina	Wa	Ma		yes
Smith2005	Whakatane T1	Okataina	Okataina	Wk	Ma		yes
Smith2005	Whakatane T2	Okataina	Okataina	Wk	Wk		
Smith2005	Whakatane T3	Okataina	Okataina	Wk	Wk		
Smith2006	Whakatane MDF	Okataina	Okataina	Wk	Wk		
Smith2006	Whakatane MDF	Okataina	Okataina	Wk	Wk		
Smith2006	Whakatane T1	Okataina	Okataina	Wk	Wk		
Smith2006	Whakatane T3	Okataina	Okataina	Wk	Wk		
Smith2006	Whakatane T1	Okataina	Okataina	Wk	Wk		
Smith2006	Whakatane T1	Okataina	Okataina	Wk	Wk		
Smith2006	Whakatane T1	Okataina	Okataina	Wk	Wk		
Smith2006	Whakatane T3	Okataina	Okataina	Wk	Wk		
Smith2006	Whakatane T2	Okataina	Okataina	Wk	Wk		
Smith2006	Whakatane T2	Okataina	Okataina	Wk	Wk		
Smith2006	Whakatane T1	Okataina	Okataina	Wk	Wk		
Smith2006	Whakatane T1	Okataina	Okataina	Wk	Wk		
Smith2006	Whakatane T2	Okataina	Okataina	Wk	Wk		
Smith2006	Whakatane T2	Okataina	Okataina	Wk	Wk		

[a]References:

Allan, A. S. R., J. Baker, L. Carter, and R. J. Wysoczanksi (2008), Reconstructing the Quaternary evolution of the world's most active silicic volcanic system: insights from an ~1.65Ma deep ocean tephra record sourced from Taupo Volcanic Zone, New Zealand, Quat. Sci. Rev., 27(25-26), 2341–2360.

Bilderback, E. L. (2012), Hillslope response to climate-modulated river incision and the role of deep-seated landslides in post-glacial sediment flux: Waipaoa Sedimentary System, New Zealand, PhD Thesis, University of Canterbury. Geological Sciences.

Lowe, D. J., P. R. Shane, B. V. Alloway, and R. M. Newnham (2008), Fingerprints and age models for widespread New Zealand tephra marker beds erupted since 30,000 years ago: a framework for NZ-INTIMATE, Quat. Sci. Rev., 27(1-2), 95–126.

Puck XX-X are control samples from Bilderback (2012) re-run in this study

Smith, V., P. Shane, and I. Nairn, and C.M. Williams (2006), Geochemistry and magmatic properties of eruption episodes from Haroharo linear vent zone, Okataina Volcanic Centre, New Zealand during the last 10 kyr. Bulletin of Volcanology, 69(1), 57-88.

Smith, V., P. Shane, and I. Nairn (2005), Trends in rhyolite geochemistry, mineralogy, and magma storage during the last 50 kyr at Okataina and Taupo volcanic centres, Taupo Volcanic Zone, New Zealand, J. Volcanol. Geotherm. Res., 148, 372–406.

Wright CM (2000) Stratigraphy, volcanology, petrology and geochemistry of the 7.5 ka Mamaku eruptive episode, Okataina Volcanic Centre, North Island, New Zealand, MSc Thesis, The University of Auckland.

Table B4. Reconstruction trials[a]

LGM	17.5	ka					
Trial	*Channel*	*Interpolation*	*Break Points*	*Boundary*	*SSE*	*Vol (km^3)*	*Erosion (mm/yr)*
1	main	linear	polygons	modern	1.69E-19	0.32	1.12
2	main	cubic	polygons	modern	0	0.32	1.10
3	main	linear, centered	polygons	modern	1.6	0.31	1.09
4	main	cubic, centered	polygons	modern	0.1411	0.31	1.06
5	valley	linear, centered	polygons	modern	4.04E-08	0.31	1.08
6	valley	linear, centered	main ridges	modern	9.95E-23	0.41	1.41
7	valley	cubic, centered	polygons	modern	3.97E-08	0.30	1.04
8	valley	cubic, centered	none	modern	6.40E-17	0.39	1.34
9	valley	cubic, centered	none	spline	7.91E-20	0.37	1.28
10	valley	cubic, centered	all ridges (value=mode)	spline	3.47E-20	0.41	1.42
11	valley	cubic, centered	polygons	spline	1.89	0.44	1.52
12	valley	cubic, centered	polygons plus ghost poinst (18m)	spline	1.89	0.47	1.62
13	**valley**	**cubic, centered**	**polygons plus ghost pts (8m)**	**spline**	**1.89**	**0.46**	**1.59**
Rotoma	9.4	ka					
Trial	*Channel*	*Interpolation*	*Break Points*	*Boundary*	*SSE*	*Vol (km^3)*	*Erosion (mm/yr)*
1	valley	linear, centered	all ridges (value=mean)	modern	2.51E-22	0.16	1.01
2	valley	linear, centered	polygons	modern	4.97E-08	0.06	0.40
3	valley	linear, centered	main ridges	modern	1.58E-22	0.32	2.09
4	valley	cubic, centered	all ridges (value=mean)	modern	1.03E-20	0.15	0.98
5	valley	cubic, centered	none	modern	6.40E-17	0.26	1.66
6	valley	cubic, centered	none	spline	6.78E-20	0.24	1.56
7	**valley**	**cubic, centered**	**all ridges (value=mode)**	**spline**	**1.12E-19**	**0.20**	**1.28**
Whakatane	5.5	ka					
Trial	*Channel*	*Interpolation*	*Break Points*	*Boundary*	*SSE*	*Vol (km^3)*	*Erosion (mm/yr)*
1	valley	linear, centered	all ridges (value=mean)	modern	2.84E-15	0.12	1.33
2	valley	cubic, centered	all ridges (value=mean)	modern	2.34E-19	0.12	1.30
3	valley	cubic, centered	none	modern	6.40E-17	0.20	2.20
4	**valley**	**cubic, centered**	**all ridges (value=mode)**	**spline**	**1.30E-20**	**0.13**	**1.49**
Waimihia	3.4	ka					
Trial	*Channel*	*Interpolation*	*Break Points*	*Boundary*	*SSE*	*Vol (km^3)*	*Erosion (mm/yr)*
1	valley	linear, centered	all ridges (value=mean)	modern	8.57E-22	0.11	2.00
2	valley	cubic, centered	all ridges (value=mean)	modern	1.11E-18	0.11	1.95
3	valley	cubic, centered	none	modern	6.40E-17	0.18	3.24
4	**valley**	**cubic, centered**	**all ridges (value=mode)**	**spline**	**1.25E-21**	**0.12**	**2.16**
5	valley	cubic, centered	all ridges (value=mode), alt. concavity	spline	6.4E-20	0.11	1.98

[a]Bold type trial is paleosurface used for final calculations

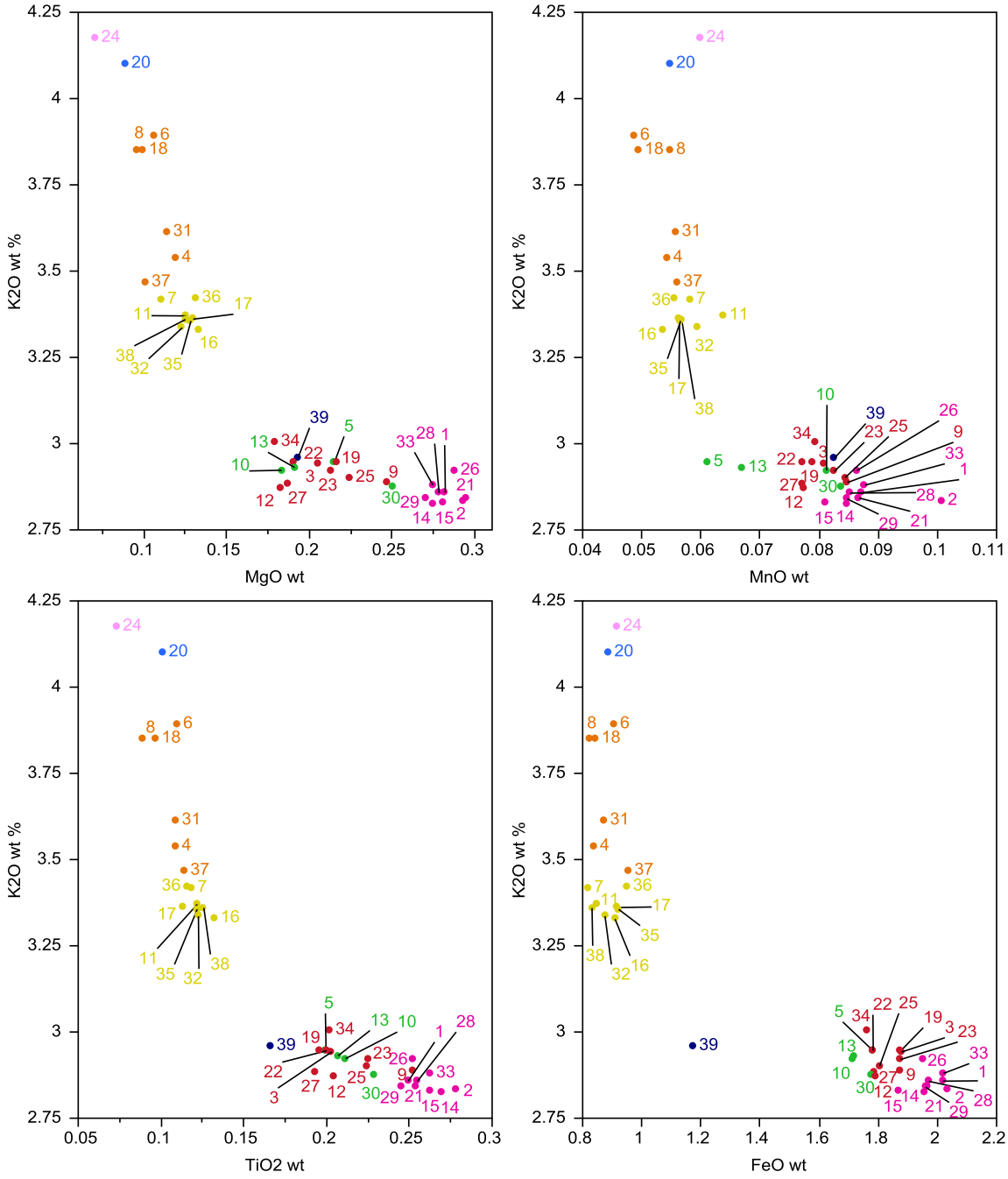

Figure B1. Binary plots of tephra composition comparing K2O to (a) MgO, (b) FeO, (c) MnO, and (d) TiO2 for all probed basal tephra samples. Circles represent resulting compositions from microprobe analysis completed for this study, and crosses represent control sample composition from Lowe et al. [2008] (Kh=Kaharoa, Op=Opepe, Om=Omataroa, Ro=Rotoma, Re=Rerewhakaaitu, Tp=Taupo, Wm=Waimihia, Wk=Whakatane). Sample numbers correspond to sample locations (Figure 1c). Full major oxide composition of all probed samples is included in the Table B1.

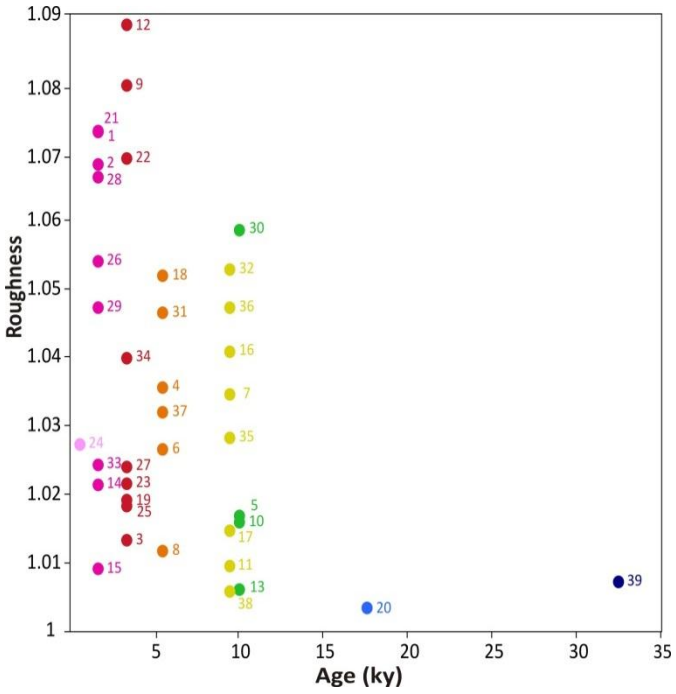

Figure B2. Roughness ratio for each sample pit location averaged over a 15 m window. These results were then binned by tephra (except Opepe) and averaged to determine the mean roughness used for each timestep in Figures 2c & A3. Sample numbers correspond to sample locations on Figure 1c.

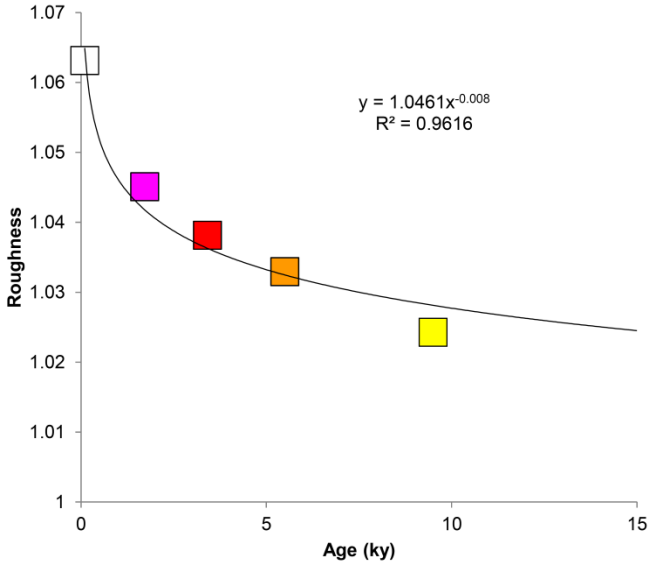

Figure B3. Power law regression fit of mean roughness for binned samples with 15 m smoothing of Rotoma (9.5 ka), Whakatane (5.5 ka), Waimihia (3.4 ka), Taupo (1.7 ka), and no tephra. Compared to linear regression fit in Figure 2c.

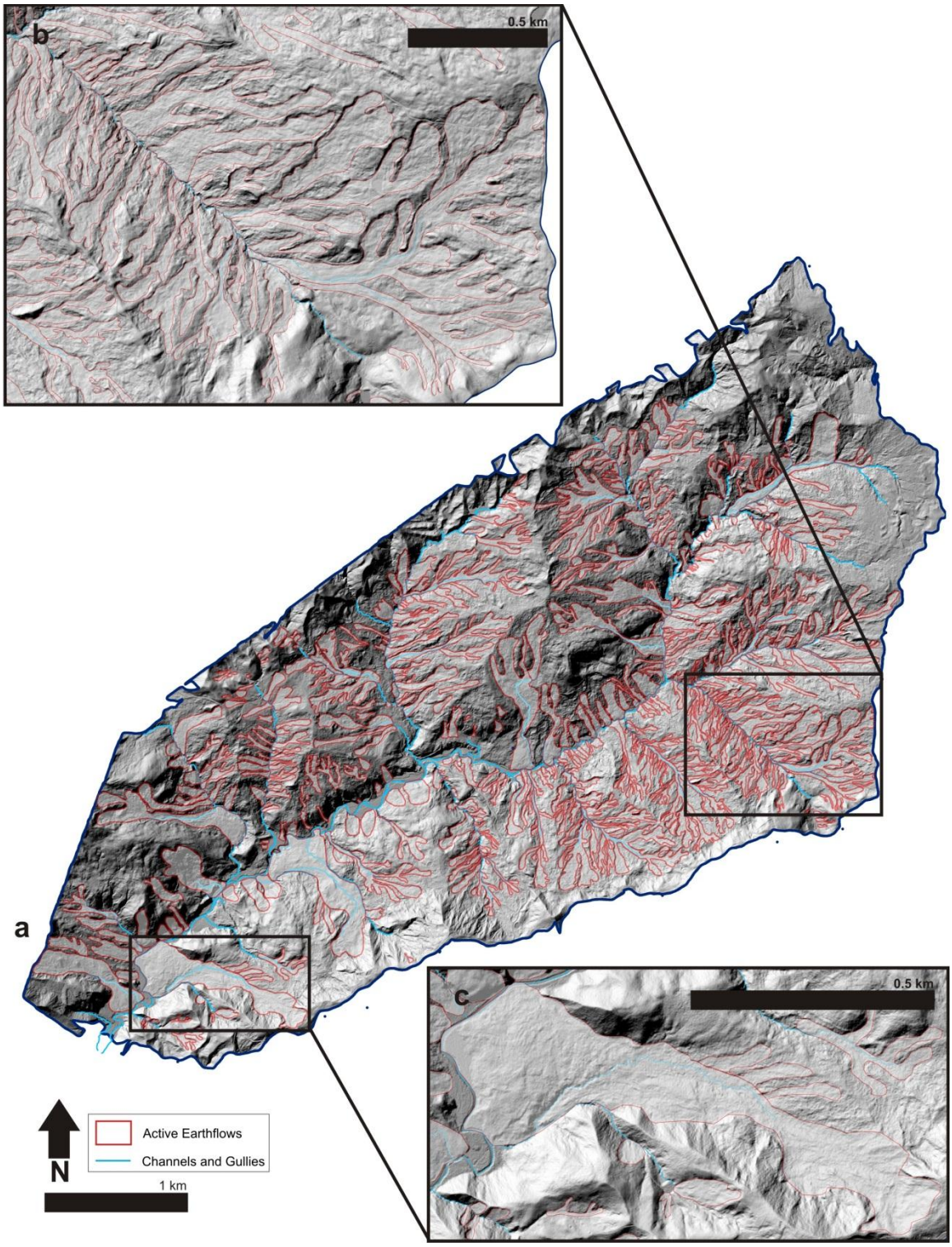

Figure B4. (a) Outlines of active earthflows in the Mangataikapua, mapped in ArcGIS from the 2010 lidar hillshade and corresponding orthophoto. (b) Earthflows in the upper watershed are predominantly narrower and do not intersect the Mangataikapua stream. (c) Earthflows in the lower watershed often encompass their entire source catchment and are directly coupled with the Mangataikapua stream, forming large toes that displace the channel.

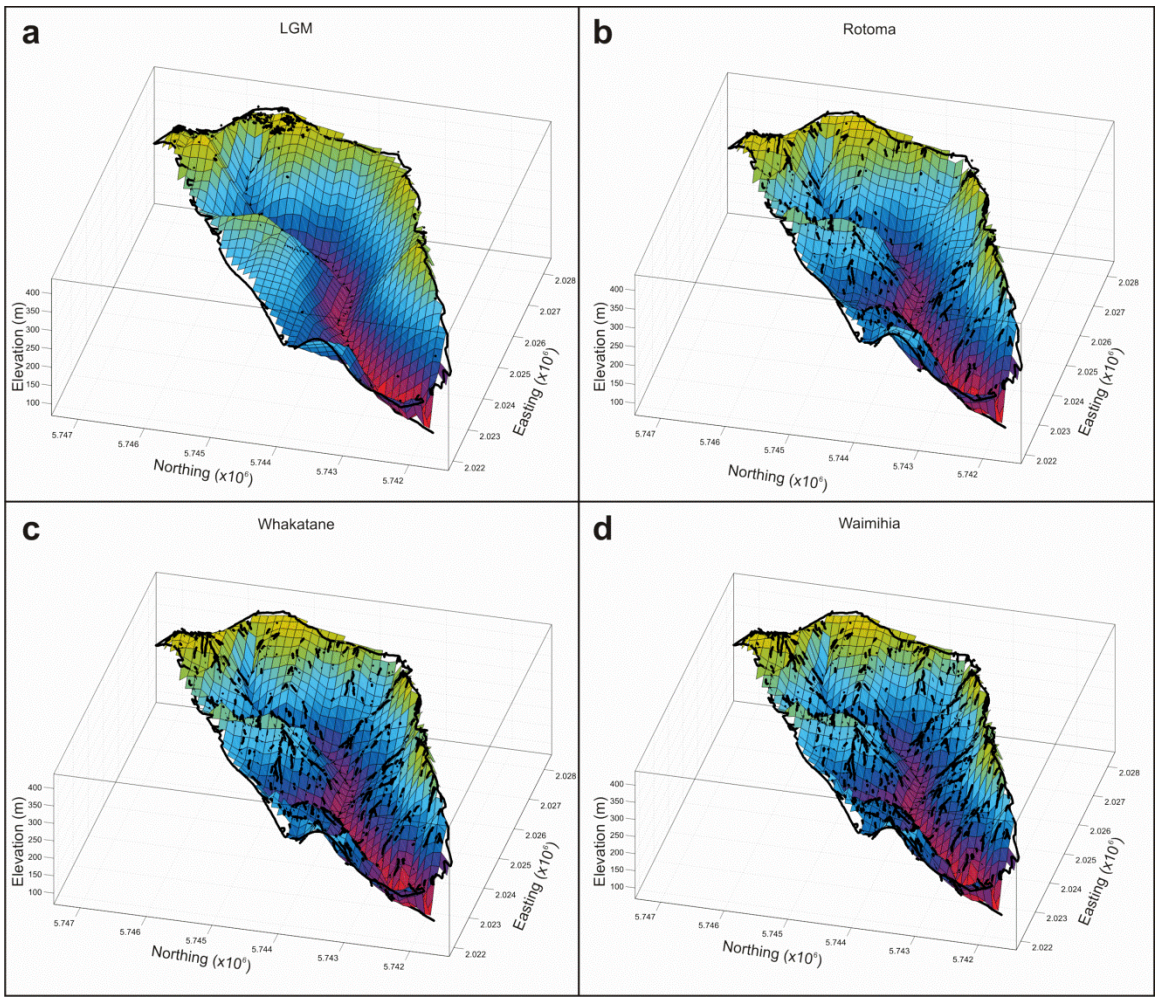

Figure B5. Resulting fit from MATLAB's cubic spline interpolation for each timestep: (a) LGM, (b) Rotoma, (c) Whaktane, and (d) Waimihia.

APPENDIX C

CHAPTER III SUPPLEMENTARY MATERIAL

Table C1. Turf index velocity measurements

Class 1 Velocity (m/y)	Class 2 Velocity (m/yr)	Class 3 Velocity (m/yr)
0.5	4.2	7
0.6	3.8	11
1.0	5.5	30
0.5	3.5	-
0.5	1.5	-
0.8	1.9	-
avg (m/yr) 0.6	**3.4**	**-**
sd (m/yr) 0.2	**1.5**	**-**

Table C2. Landslide toe depths measured in the field and calculated from the 2010 DEM

	Toe Width (m)	Field Depth (d) (m)	sd (m)	d1	d2	d3	d4	Curvature Depth (m)	sd (m)
1	3	-	-	-	-	-	-	11.9	-
2	6	-	-	-	-	-	-	9.3	-
3	13	-	-	-	-	-	-	6.6	-
4	5	5.2	-	5.2	-	-	-	7.4	3.1
5	27	3.2	0.6	3.6	2.7	-	-	3.3	1.6
6	7	-	-	-	-	-	-	2.7	-
7	23	5.0	1.8	5.7	6.3	2.9	-	5.1	1.6
8	19	4.4	1.6	5.5	3.2	-	-	4.7	1.1
9	5	-	-	-	-	-	-	2.9	-
10	12	-	-	-	-	-	-	7.2	-
11	14	4.9	-	4.9	-	-	-	4.0	1.3
12	23	3.4	0.1	3.3	3.5	-		4.3	1.0
13	22	2.6	-	2.6	-	-	-	4.6	1.8
14	13	6.0	-	6.0	-	-	-	5.7	0.4
15	37	5.0	1.4	3.7	4.8	6.5		4.5	1.2
16	17	-	-	-	-	-	-	6.1	1.3
17	10	-	-	-	-	-	-	7.1	-
18	30	4.8	-	4.8	-	-	-	5.3	0.6
19	23	3.5	-	3.5	-	-	-	5.3	2.6
20	53	5.5	0.3	5.3	5.7	-	-	4.7	1.3
21	17	5.2	-	5.2	-	-	-	5.5	2.1
22	5	5.0	1.6	6.1	3.9	-		4.1	2.1
23	7	3.8	-	3.8	-	-	-	10.4	9.3
24	9	-	-	-	-	-	-	2.7	-
25	14	-	-	-	-	-	-	2.6	2.0
26	9	-	-	-	-	-	-	7.7	4.7
27	10	-	-	-	-	-	-	3.6	-
28	35	-	-	-	-	-	-	2.3	1.6
29	18	2.9	-	2.9	-	-	-	2.9	-
30	4	7.9	-	7.9	-	-	-	7.9	-
31	9	-	-	-	-	-	-	9.5	4.6
32	30	4.7	0.9	4	5.3	-	-	3.5	2.0
33	6	5.2	-	5.2	-	-	-	6.1	1.3
34	7	3.0	2.3	4.6	1.3	-	-	3.0	2.3
35	5	4.0	1.6	5.1	2.8	-	-	4.0	1.6
36	3	5.2	-	-	-	-	-	5.2	-
37	7	5.0	1.8	3.7	6.3	-	-	4.1	2.1
38	11	-	-	-	-	-	-	5.5	-
39	3	6.6	-	6.6	-	-	-	6.7	0.1
40	11	-	-	-	-	-	-	5.4	-
41	8	2.8	-	2.8	-	-	-	2.8	-
42	7	3.9	-	3.9	-	-	-	3.9	-
43	13	3.1	-	3.1	-	-	-	3.1	-
44	31	6.5	-	6.5	-	-	-	4.1	2.4
45	8	4.5	-	4.5	-	-	-	3.5	1.4
46	5	-	-	-	-	-	-	3.3	-
47	7	3.1	-	3.1	-	-	-	2.9	0.3
48	6	3.8	-	3.8	-	-	-	3.8	-
49	4	-	-	-	-	-	-	4.4	-
50	15	3.4	0.4	3.1	3.7	-	-	4.0	1.1
51	6	-	-	-	-	-	-	3.6	-
52	6	4.7	-	4.7	-	-	-	4.9	0.3
53	9	-	-	-	-	-	-	8.9	-
54	6	-	-	-	-	-	-	6.0	-
55	6	4.2	-	4.2	-	-	-	3.6	0.9
56	20	3.4	0.9	3.7	4.1	2.3	-	3.2	0.7
57	10	-	-	-	-	-	-	2.8	-
58	134	6.7	2.4	6.5	4.8	10	5.3	6.4	2.5
59	169	1.3	-	1.3	-	-	-	3.0	1.1
	n	**37**						**59**	
	avg (m)	**4.4**						**5.0**	
	sd (m)	**1.3**						**2.1**	

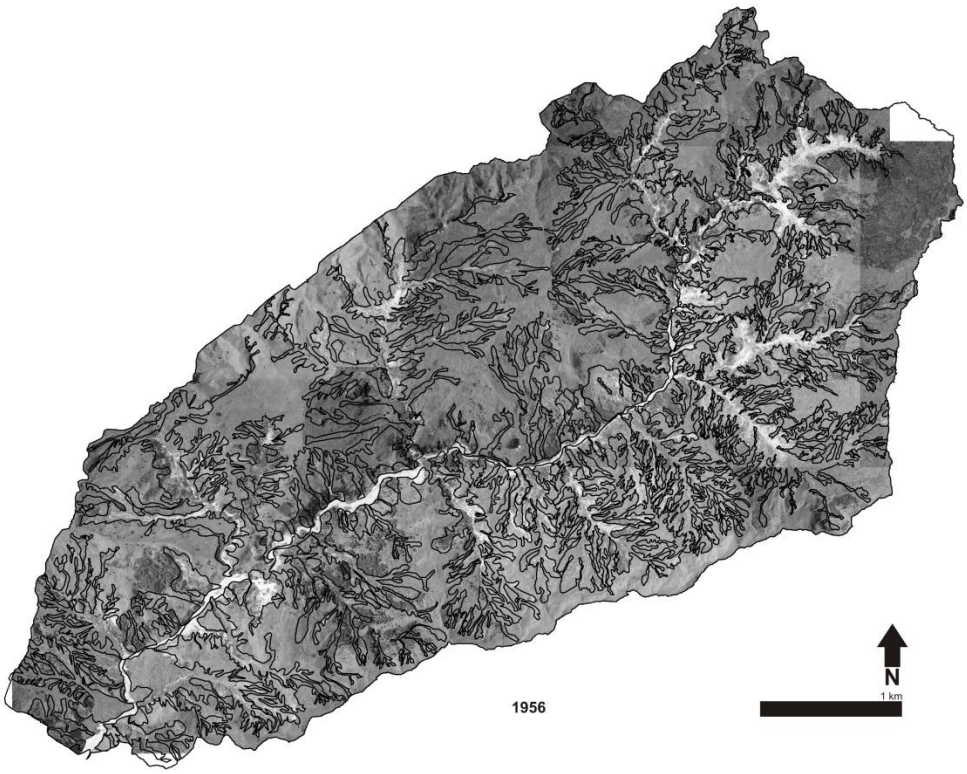

Figure C1. Active landslide outlines (black) on the orthorectified photos for 1956.

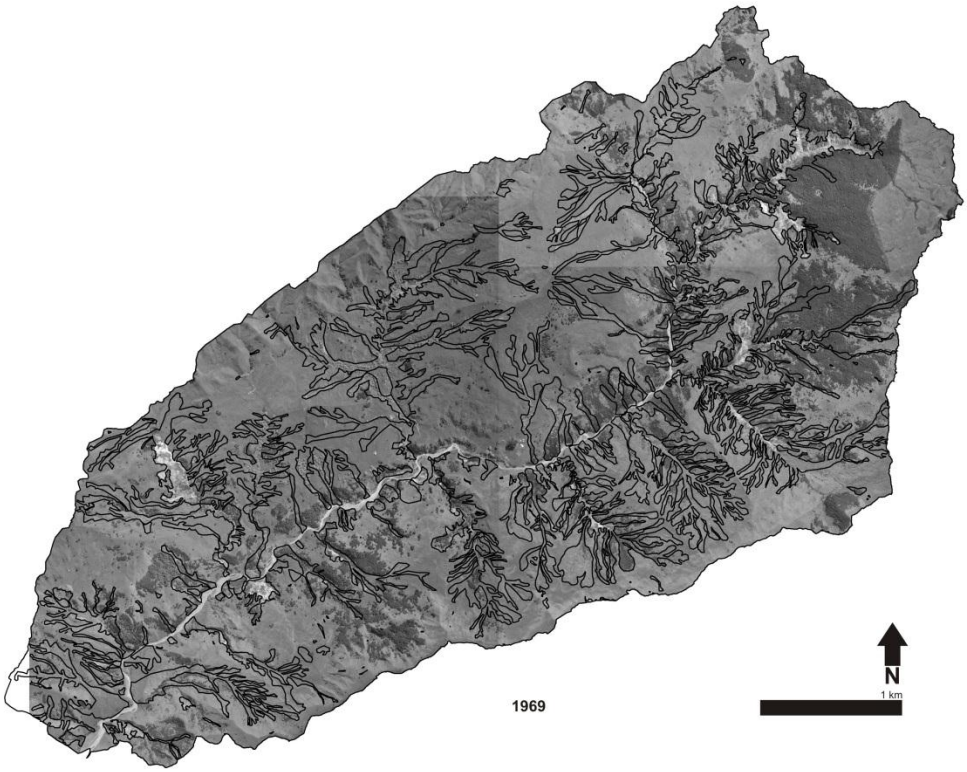

Figure C2. Active landslide outlines (black) on the orthorectified photos for 1969.

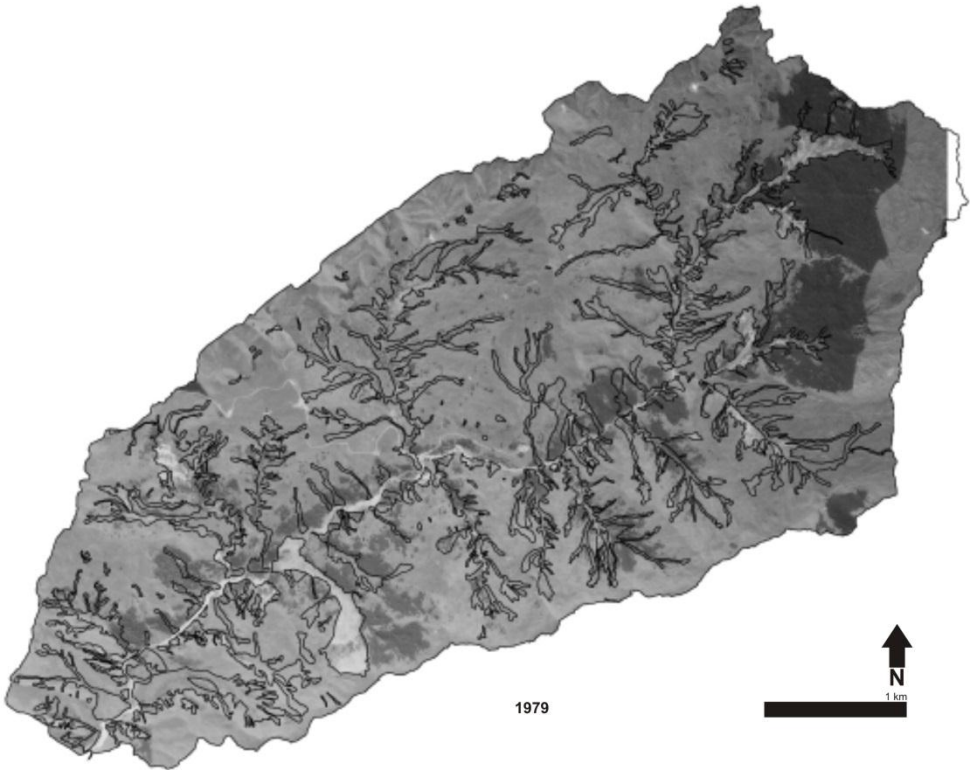

Figure C3. Active landslide outlines (black) on the orthorectified photo for 1979.

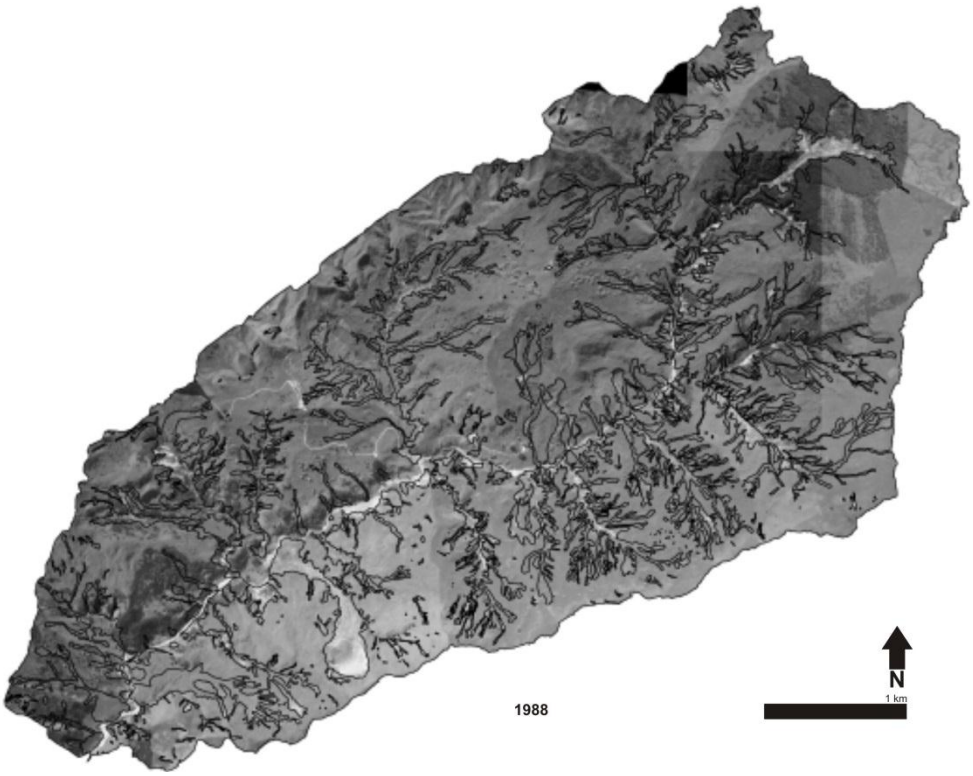

Figure C4. Active landslide outlines (black) on the orthorectified photos for 1988.

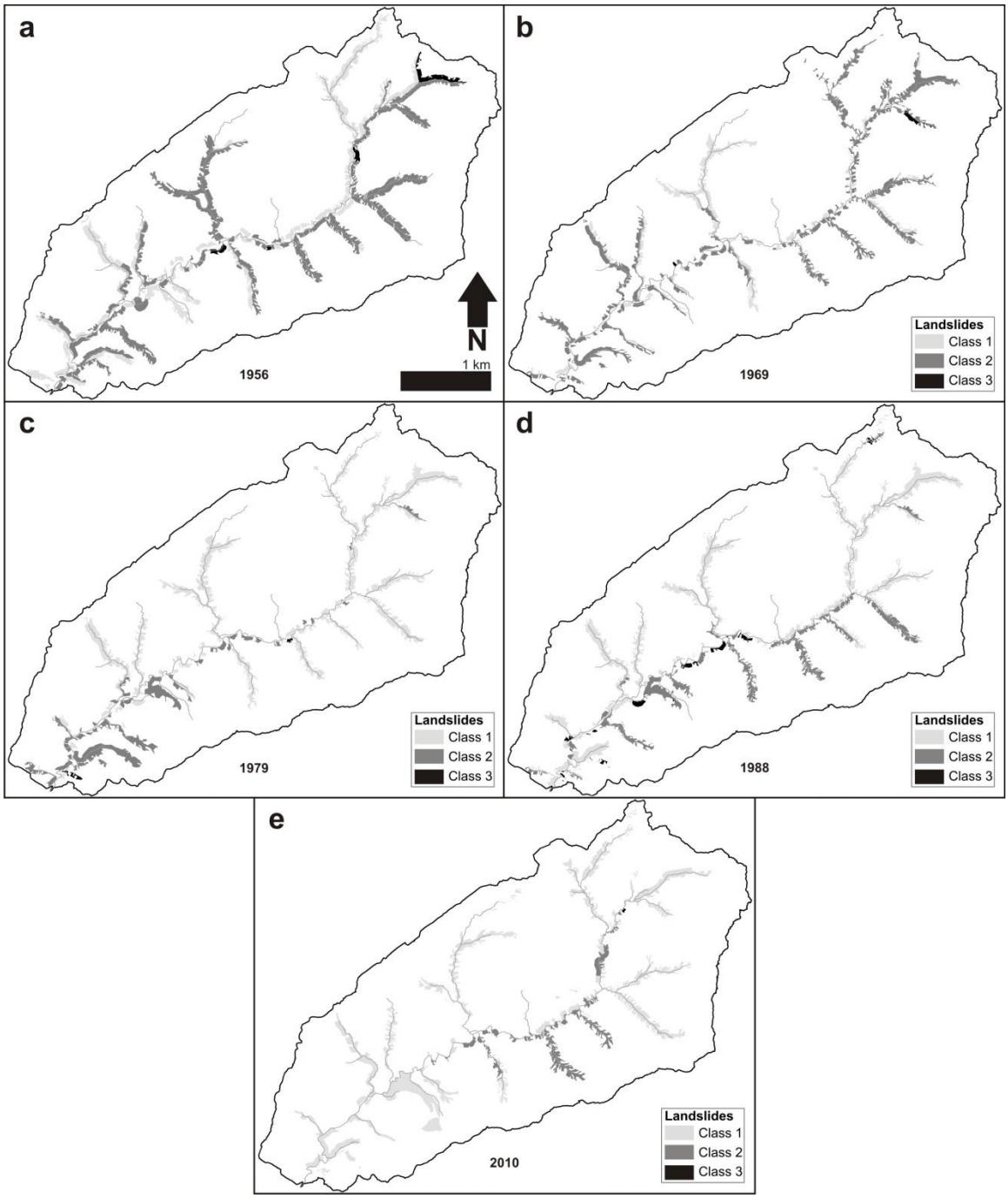

Figure C5. Buffered (50 m) landslide polygons shaded by the corresponding 'turf index' classification: slowest (Class 1, light grey) to fastest (Class 3, black).

APPENDIX D

CHAPTER IV SUPPLEMENTARY MATERIAL

Table D1. Borehole (BH) and slope inclinometer (SI) data and fit

Name	**Data Type**	**X** (Easting)	**Y** (Northing)	**Logged Failure Plane Depth** (m)	**Fitted Failure Plane Depth** (m)	**Residual** (m)
CCIN10-1	SI	434597	4944405	53.0	56.6	-3.5
CCIN10-3	SI	434659	4944344	66.4	65.7	0.7
CCIN12-2	SI	434629	4944391	59.9	58.0	1.9
CCIN12-3	SI	434658	4944343	67.7	65.9	1.8
F10-08	SI	434529	4944495	39.6	42.2	-2.5
F10-11	SI	434730	4944246	82.8	81.5	1.3
F10-13	SI	434559	4944441	41.6	51.2	-9.6
F10-14	SI	434594	4944408	52.4	56.1	-3.7
F10-16	SI	434604	4944307	71.6	74.8	-3.2
F10-19	SI	434664	4944302	77.6	73.4	4.2
F10-29	SI	434581	4944489	31.5	41.3	-9.8
C6BH05-1	BH	434870	4944036	115.0	115.8	-0.8
CCBH05-2	BH	434591	4944417	59.3	54.5	4.7
CCBH05-3	BH	434622	4944379	65.9	60.5	5.4
CCIN10-1	BH	434597	4944405	51.5	56.6	-5.1
CCIN10-3	BH	434659	4944344	66.1	65.7	0.4
CCIN10-3A	BH	434658	4944345	62.6	65.6	-2.9
CCIN12-2	BH	434629	4944391	55.7	58.0	-2.3
CCIN12-3	BH	434658	4944343	66.2	65.9	0.3
F10-05	BH	434655	4944214	90.6	90.4	0.2
F10-08	BH	434529	4944495	53.9	42.2	11.8
F10-11	BH	434730	4944246	82.5	81.5	1.0
F10-13	BH	434559	4944441	51.7	51.2	0.5
F10-14	BH	434594	4944408	50.6	56.1	-5.5
F10-16	BH	434604	4944307	71.9	74.8	-2.9
F10-17	BH	434514	4944461	56.5	49.1	7.4
F10-18	BH	434690	4944288	77.0	75.1	1.9
F10-19	BH	434664	4944302	76.4	73.4	2.9
F10-29	BH	434581	4944489	47.1	41.3	5.7

Table D2. Comparison between fitted plane and refraction data for Cougar Creek

Geophone Locations					Failure Depth[a]			Landslide Thickness[b]			Fit Residuals	
Geophone	**Distance (X_{dist})** (m)	***X*** (Easting)	***Y*** (Northing)	***Z*** (m)	Z_2 (m)	Z_3 (m)	Z_{fp} (m)	$Z-Z_2$ (m)	$Z-Z_3$ (m)	$Z-Z_{fp}$ (m)	$Z_{fp}-Z_2$ (m)	$Z_{fp}-Z_3$ (m)
20	50	434527	4944408	84.8	67.7	75.4	58.6	17.1	9.4	26.2	9.1	16.8
21	52.5	434529	4944407	84.4	66.1	73.7	58.8	18.3	10.7	25.6	7.3	14.9
22	55	434531	4944405	84.0	65.0	71.7	59.0	19.0	12.3	25.0	6.0	12.7
23	57.5	434532	4944403	83.5	63.9	69.7	59.3	19.6	13.8	24.2	4.6	10.4
24	60	434534	4944401	83.1	62.8	67.7	59.6	20.3	15.4	23.5	3.2	8.1
25	62.5	434536	4944400	82.8	61.9	66.1	59.9	20.9	16.7	22.9	2.0	6.2
26	65	434537	4944398	82.4	61.1	64.7	60.2	21.3	17.7	22.2	0.9	4.5
27	67.5	434539	4944396	82.1	60.2	63.4	60.4	21.9	18.7	21.7	-0.2	3.0
28	70	434541	4944394	81.8	59.3	62.6	60.7	22.5	19.2	21.1	-1.4	1.9
29	72.5	434543	4944392	81.5	58.5	63.1	61.0	23.0	18.4	20.5	-2.5	2.1
30	75	434544	4944391	81.3	58.4	63.8	61.2	22.9	17.5	20.1	-2.8	2.6
31	77.5	434546	4944389	81.0	58.4	64.6	61.5	22.6	16.4	19.6	-3.1	3.1
32	80	434548	4944387	80.8	58.3	65.3	61.7	22.5	15.5	19.1	-3.4	3.6
33	82.5	434549	4944385	80.6	58.2	65.2	62.1	22.4	15.4	18.5	-3.9	3.1
34	85	434551	4944384	80.4	58.2	64.6	62.3	22.2	15.8	18.1	-4.1	2.3
35	87.5	434553	4944382	80.4	58.1	63.8	62.5	22.3	16.6	17.9	-4.4	1.3
36	90	434555	4944380	80.3	57.8	62.9	62.9	22.5	17.4	17.4	-5.1	0.0
37	92.5	434556	4944378	80.2	57.4	62.0	63.1	22.8	18.2	17.1	-5.7	-1.1
38	95	434558	4944377	80.1	56.9	60.5	63.4	23.2	19.6	16.8	-6.5	-2.9
39	97.5	434559	4944374	79.9	56.5	59.5	63.7	23.4	20.4	16.1	-7.2	-4.2
40	100	434561	4944373	79.6	56.2	58.7	63.9	23.4	20.9	15.7	-7.7	-5.2
41	102.5	434563	4944372	79.6	56.1	58.2	64.1	23.5	21.4	15.5	-8.0	-5.9
42	105	434565	4944370	79.7	56.1	57.9	64.3	23.6	21.8	15.4	-8.2	-6.4
43	107.5	434567	4944369	79.9	56.2	58.1	64.6	23.7	21.8	15.4	-8.4	-6.5
44	110	434569	4944367	79.9	56.0	58.7	64.8	23.9	21.2	15.1	-8.8	-6.1
45	112.5	434571	4944365	80.1	55.8	59.8	65.1	24.3	20.3	15.0	-9.3	-5.3
46	115	434573	4944363	80.3	55.6	61.3	65.3	24.7	19.0	15.0	-9.7	-4.0
47	117.5	434574	4944361	80.4	55.9	62.3	65.7	24.5	18.1	14.7	-9.8	-3.4
48	120	434576	4944359	80.6	56.6	62.4	66.0	24.0	18.2	14.6	-9.4	-3.6
49	122.5	434577	4944358	80.7	57.3	62.6	66.2	23.4	18.1	14.4	-8.9	-3.6
50	125	434579	4944356	80.8	58.1	62.8	66.5	22.7	18.0	14.3	-8.4	-3.7
51	127.5	434581	4944354	81.0	58.8	63.5	66.8	22.2	17.5	14.2	-8.0	-3.3
52	130	434582	4944352	81.1	59.7	63.9	67.2	21.4	17.2	13.9	-7.5	-3.3
53	132.5	434584	4944350	81.3	60.6	64.3	67.3	20.7	17.0	14.0	-6.7	-3.0
54	135	434586	4944349	81.5	60.8	64.4	67.6	20.7	17.1	13.9	-6.8	-3.2
55	137.5	434587	4944346	81.8	61.0	64.4	68.0	20.8	17.4	13.8	-7.0	-3.6
56	140	434589	4944345	81.9	61.5	64.6	68.2	20.4	17.3	13.7	-6.7	-3.6
57	142.5	434590	4944342	82.1	62.1	65.4	68.6	20.0	16.7	13.5	-6.5	-3.2
58	145	434591	4944340	82.1	62.5	66.4	69.0	19.6	15.7	13.1	-6.5	-2.6
59	147.5	434593	4944338	82.2	62.9	67.4	69.3	19.3	14.8	12.9	-6.4	-1.9
60	150	434594	4944336	82.3	63.3	68.4	69.7	19.0	13.9	12.6	-6.4	-1.3
61	152.5	434595	4944334	82.6	63.5	68.8	70.1	19.1	13.8	12.6	-6.6	-1.3
62	155	434596	4944332	82.7	63.7	69.9	70.4	19.0	12.8	12.3	-6.7	-0.5
63	157.5	434597	4944329	82.8	63.9	71.4	70.8	18.9	11.4	12.0	-6.9	0.6

Table D2. (continued)

Geophone Locations					Failure Depth[a]			Landslide Thickness[b]			Fit Residuals	
Geophone	**Distance (X_{dist})** (m)	***X*** (Easting)	***Y*** (Northing)	***Z*** (m)	Z_2 (m)	Z_3 (m)	Z_{fp} (m)	$Z-Z_2$ (m)	$Z-Z_3$ (m)	$Z-Z_{fp}$ (m)	$Z_{fp}-Z_2$ (m)	$Z_{fp}-Z_3$ (m)
64	160	434598	4944327	82.9	64.0	72.0	71.2	18.9	10.9	11.7	-7.2	0.8
65	162.5	434599	4944325	83.1	64.2	71.9	71.6	18.9	11.2	11.5	-7.4	0.3
66	165	434600	4944323	83.3	64.5	71.7	72.0	18.8	11.6	11.3	-7.5	-0.3
67	167.5	434601	4944320	83.4	64.8	71.7	72.4	18.6	11.7	11.0	-7.6	-0.7
68	170	434601	4944318	83.6	65.2	71.8	72.8	18.4	11.8	10.8	-7.6	-1.0
69	172.5	434603	4944316	83.8	65.9	72.2	73.0	17.9	11.6	10.8	-7.1	-0.8
70	175	434605	4944315	84.1	66.8	72.6	73.3	17.3	11.5	10.8	-6.5	-0.7
71	177.5	434606	4944312	84.0	67.6	73.1	73.7	16.4	10.9	10.3	-6.1	-0.6
72	180	434605	4944310	84.4	68.3	73.4	74.1	16.1	11.0	10.3	-5.8	-0.7
73	182.5	434607	4944308	85.0	68.9	73.6	74.5	16.1	11.4	10.5	-5.6	-0.9
74	185	434608	4944306	85.3	69.5	73.7	74.8	15.8	11.6	10.5	-5.3	-1.1
75	187.5	434609	4944304	85.8	70.0	73.6	75.2	15.8	12.2	10.6	-5.2	-1.6
76	190	434611	4944302	86.2	70.2	73.2	75.5	16.0	13.0	10.7	-5.3	-2.3
77	192.5	434612	4944299	86.4	70.5	72.8	75.9	15.9	13.6	10.5	-5.4	-3.1
78	195	434613	4944297	86.9	70.8	72.5	76.3	16.1	14.4	10.6	-5.5	-3.8
79	197.5	434614	4944295	87.3	71.1	72.5	76.6	16.2	14.8	10.7	-5.5	-4.1
80	200	434615	4944293	87.7	71.8	72.7	77.0	15.9	15.0	10.7	-5.2	-4.3
81	202.5	434616	4944291	88.2	72.4	73.1	77.4	15.8	15.1	10.8	-5.0	-4.3
82	205	434617	4944288	88.6	73.1	73.8	77.8	15.5	14.8	10.8	-4.7	-4.0
83	207.5	434618	4944286	89.0	73.9	74.9	78.2	15.1	14.1	10.8	-4.3	-3.3
84	210	434620	4944284	89.4	74.7	76.0	78.5	14.7	13.4	10.9	-3.8	-2.5
85	212.5	434622	4944282	89.8	75.5	77.0	78.8	14.3	12.8	11.1	-3.3	-1.8
86	215	434623	4944280	90.4	76.2	78.1	79.0	14.2	12.3	11.3	-2.8	-0.9
87	217.5	434625	4944279	90.8	76.4	79.0	79.3	14.4	11.8	11.5	-2.9	-0.3
88	220	434627	4944277	91.3	76.6	79.4	79.5	14.7	11.9	11.8	-2.9	-0.1
89	222.5	434629	4944275	91.8	76.7	79.6	79.8	15.1	12.2	12.0	-3.1	-0.2
90	225	434631	4944274	92.2	76.9	79.9	80.0	15.3	12.3	12.2	-3.1	-0.1
91	227.5	434633	4944272	92.6	77.2	80.5	80.2	15.4	12.1	12.4	-3.0	0.3
92	230	434635	4944271	93.1	77.6	81.2	80.4	15.5	11.9	12.7	-2.8	0.8
93	232.5	434636	4944269	93.5	78.0	81.9	80.7	15.5	11.6	12.9	-2.7	1.2
94	235	434638	4944268	94.0	78.5	82.6	80.9	15.5	11.4	13.1	-2.4	1.7
95	237.5	434640	4944266	94.4	79.4	83.1	81.1	15.0	11.3	13.2	-1.7	2.0
96	240	434642	4944264	94.9	79.3	83.4	81.4	15.6	11.5	13.5	-2.1	2.0
97	242.5	434643	4944262	95.4	78.8	83.3	81.8	16.6	12.1	13.5	-3.0	1.5
98	245	434644	4944260	95.8	78.1	82.8	82.2	17.7	13.0	13.6	-4.1	0.6
99	247.5	434646	4944258	96.2	77.5	82.3	82.5	18.7	13.9	13.8	-5.0	-0.2
100	250	434647	4944256	96.5	76.9	81.7	82.8	19.6	14.8	13.7	-5.9	-1.1
101	252.5	434649	4944254	96.8	76.3	81.2	83.1	20.5	15.6	13.8	-6.8	-1.9
102	255	434650	4944252	97.1	76.0	80.7	83.4	21.1	16.4	13.7	-7.4	-2.7
103	257.5	434651	4944250	97.5	76.0	80.3	83.8	21.5	17.2	13.7	-7.8	-3.5
104	260	434653	4944248	97.7	76.2	79.9	84.2	21.5	17.8	13.6	-8.0	-4.3
105	262.5	434654	4944245	97.8	76.5	79.7	84.5	21.3	18.1	13.3	-8.0	-4.8
106	265	434655	4944243	98.0	77.1	79.9	84.9	20.9	18.1	13.1	-7.8	-5.0
107	267.5	434656	4944241	98.0	77.7	80.3	85.2	20.3	17.7	12.8	-7.5	-4.9
108	270	434658	4944239	98.2	78.5	80.8	85.5	19.7	17.4	12.6	-7.0	-4.7

Table D2. (continued)

Geophone Locations					Failure Depth[a]			Landslide Thickness[b]			Fit Residuals	
Geophone	**Distance (X_{dist})** (m)	***X*** (Easting)	***Y*** (Northing)	***Z*** (m)	Z_2 (m)	Z_3 (m)	Z_{fp} (m)	$Z-Z_2$ (m)	$Z-Z_3$ (m)	$Z-Z_{fp}$ (m)	$Z_{fp}-Z_2$ (m)	$Z_{fp}-Z_3$ (m)
109	272.5	434660	4944238	98.3	79.3	81.4	85.7	19.0	16.9	12.6	-6.4	-4.3
110	275	434662	4944237	98.8	80.2	81.9	85.8	18.6	16.9	13.0	-5.6	-3.9
111	277.5	434664	4944236	99.2	81.1	82.6	85.8	18.1	16.6	13.4	-4.7	-3.2
112	280	434667	4944235	99.6	81.9	83.7	85.9	17.7	15.9	13.6	-4.0	-2.2
113	282.5	434669	4944234	99.9	82.5	84.7	86.1	17.4	15.2	13.8	-3.6	-1.4
114	285	434671	4944232	100.2	83.2	85.4	86.3	17.0	14.8	13.9	-3.1	-0.9
115	287.5	434673	4944231	100.5	83.7	86.0	86.5	16.8	14.5	14.0	-2.8	-0.5
116	290	434675	4944230	100.9	84.2	86.6	86.6	16.7	14.3	14.3	-2.4	0.0
117	292.5	434677	4944228	101.3	84.6	87.1	86.8	16.7	14.2	14.4	-2.2	0.3
118	295	434679	4944227	101.7	85.1	87.7	87.0	16.6	14.0	14.6	-1.9	0.7
119	297.5	434681	4944226	102.0	85.3	88.4	87.2	16.7	13.6	14.8	-1.9	1.2
120	300	434683	4944224	102.3	85.4	89.2	87.4	16.9	13.1	14.9	-2.0	1.8
121	302.5	434685	4944222	102.7	85.6	90.1	87.7	17.1	12.6	15.0	-2.1	2.4
122	305	434687	4944221	103.1	85.7	90.6	87.9	17.4	12.5	15.2	-2.2	2.7
123	307.5	434689	4944219	103.6	85.7	90.9	88.1	17.9	12.7	15.5	-2.4	2.8
124	310	434691	4944218	103.9	85.7	90.8	88.3	18.2	13.1	15.6	-2.6	2.5
125	312.5	434693	4944216	104.4	85.7	90.7	88.6	18.7	13.7	15.9	-2.9	2.1
126	315	434695	4944215	104.6	85.7	90.8	88.8	18.9	13.8	15.8	-3.1	2.0
127	317.5	434697	4944213	104.9	85.7	90.9	89.0	19.2	14.0	15.9	-3.3	1.9
128	320	434699	4944212	105.3	86.2	91.2	89.2	19.1	14.1	16.1	-3.0	2.0
129	322.5	434700	4944210	105.8	86.8	92.1	89.5	19.0	13.7	16.3	-2.7	2.6
130	325	434702	4944208	106.1	87.3	93.1	89.7	18.8	13.0	16.4	-2.4	3.4
131	327.5	434704	4944207	106.4	88.0	94.2	89.9	18.4	12.2	16.5	-1.9	4.3
132	330	434706	4944205	106.8	88.6	95.1	90.2	18.2	11.7	16.7	-1.6	4.9
133	332.5	434708	4944203	107.1	89.2	95.9	90.4	17.9	11.2	16.7	-1.2	5.5
134	335	434710	4944202	107.5	89.6	96.2	90.7	17.9	11.3	16.8	-1.1	5.5
135	337.5	434711	4944200	107.8	89.8	96.4	90.9	18.0	11.4	16.9	-1.1	5.5
136	340	434713	4944198	108.2	90.0	96.4	91.2	18.2	11.8	17.0	-1.2	5.2
137	342.5	434715	4944196	108.6	90.2	96.2	91.4	18.4	12.4	17.1	-1.2	4.8
138	345	434717	4944195	108.5	90.4	96.0	91.7	18.1	12.5	16.8	-1.3	4.3
139	347.5	434719	4944193	108.9	90.6	96.1	91.9	18.3	12.8	16.9	-1.3	4.2
140	350	434720	4944191	109.4	90.8	96.4	92.2	18.6	13.0	17.2	-1.4	4.2
141	352.5	434722	4944189	109.7	90.9	97.0	92.5	18.8	12.7	17.2	-1.6	4.5
142	355	434724	4944188	109.8	91.4	97.4	92.8	18.4	12.4	17.1	-1.4	4.6
143	357.5	434726	4944186	110.1	92.0	97.4	93.0	18.1	12.7	17.1	-1.0	4.4
144	360	434727	4944184	110.3	92.6	97.2	93.3	17.7	13.1	17.0	-0.7	3.9
145	362.5	434729	4944183	110.4	93.0	96.8	93.5	17.4	13.6	16.9	-0.5	3.3
146	365	434731	4944181	110.6	93.3	96.4	93.6	17.3	14.2	16.9	-0.3	2.8
147	367.5	434734	4944180	110.8	93.6	96.2	93.8	17.2	14.6	17.0	-0.2	2.4
148	370	434736	4944179	111.5	94.0	96.0	94.0	17.5	15.5	17.4	0.0	2.0
149	372.5	434738	4944177	111.3	94.3	95.8	94.2	17.0	15.5	17.1	0.1	1.6
150	375	434740	4944176	111.6	94.4	95.9	94.4	17.2	15.7	17.1	0.0	1.5
151	377.5	434742	4944174	112.1	94.5	96.7	94.7	17.6	15.4	17.4	-0.2	2.0
152	380	434743	4944172	112.4	94.5	97.8	94.9	17.9	14.6	17.5	-0.4	2.9
153	382.5	434745	4944171	112.8	94.5	98.9	95.2	18.3	13.9	17.6	-0.7	3.7

Table D2. (continued)

Geophone Locations					Failure Depth[a]			Landslide Thickness[b]			Fit Residuals	
Geophone	**Distance (X_{dist})** (m)	***X*** (Easting)	***Y*** (Northing)	***Z*** (m)	Z_2 (m)	Z_3 (m)	Z_{fp} (m)	$Z-Z_2$ (m)	$Z-Z_3$ (m)	$Z-Z_{fp}$ (m)	$Z_{fp}-Z_2$ (m)	$Z_{fp}-Z_3$ (m)
154	385	434747	4944169	113.2	94.4	99.2	95.4	18.8	14.0	17.8	-1.0	3.8
155	387.5	434749	4944167	113.7	94.2	99.2	95.7	19.5	14.5	18.0	-1.5	3.5
156	390	434750	4944165	114.1	94.0	99.0	96.0	20.1	15.1	18.1	-2.0	3.0
157	392.5	434752	4944164	114.5	93.9	98.5	96.2	20.6	16.0	18.3	-2.3	2.3
158	395	434754	4944162	115.1	93.7	98.3	96.4	21.4	16.8	18.6	-2.7	1.9
159	397.5	434756	4944160	115.5	93.6	98.1	96.7	21.9	17.4	18.8	-3.1	1.4
160	400	434758	4944159	116.1	93.6	98.2	96.9	22.5	17.9	19.1	-3.3	1.3
161	402.5	434760	4944157	116.5	93.6	99.2	97.2	22.9	17.3	19.3	-3.6	2.0
162	405	434761	4944155	117.0	93.7	100.6	97.5	23.3	16.4	19.5	-3.8	3.1
163	407.5	434763	4944154	117.4	93.9	101.3	97.7	23.5	16.1	19.8	-3.8	3.6
164	410	434765	4944152	117.9	94.0	101.7	97.9	23.9	16.2	19.9	-3.9	3.8
165	412.5	434767	4944150	118.3	94.2	101.9	98.2	24.1	16.4	20.1	-4.0	3.7
166	415	434769	4944149	118.7	94.3	102.1	98.4	24.4	16.6	20.3	-4.1	3.7
167	417.5	434771	4944147	119.2	94.5	102.1	98.6	24.7	17.1	20.6	-4.1	3.5
168	420	434773	4944146	119.5	94.6	101.9	98.8	24.9	17.6	20.7	-4.2	3.1
169	422.5	434775	4944144	119.8	94.8	101.6	99.0	25.0	18.2	20.8	-4.2	2.6
170	425	434777	4944143	120.3	94.9	101.3	99.2	25.4	19.0	21.1	-4.3	2.1
171	427.5	434779	4944141	120.7	95.4	101.2	99.5	25.3	19.5	21.1	-4.1	1.7
172	430	434780	4944139	121.0	95.6	101.2	99.8	25.4	19.8	21.2	-4.2	1.4
173	432.5	434782	4944137	121.3	95.6	100.7	100.0	25.7	20.6	21.3	-4.4	0.7
174	435	434784	4944136	121.6	95.6	100.5	100.2	26.0	21.1	21.3	-4.6	0.3
175	437.5	434786	4944134	121.9	95.8	100.2	100.5	26.1	21.7	21.5	-4.7	-0.3
176	440	434788	4944133	122.2	96.1	99.8	100.7	26.1	22.4	21.5	-4.6	-0.9
177	442.5	434790	4944131	122.7	96.3	99.5	101.0	26.4	23.2	21.7	-4.7	-1.5
178	445	434792	4944130	123.0	96.5	99.5	101.1	26.5	23.5	21.9	-4.6	-1.6
179	447.5	434794	4944128	123.2	96.8	99.9	101.3	26.4	23.3	21.9	-4.5	-1.4
180	450	434795	4944126	123.6	97.1	100.2	101.7	26.5	23.4	21.9	-4.6	-1.5
181	452.5	434797	4944124	123.9	97.6	100.4	102.0	26.3	23.5	22.0	-4.4	-1.6
182	455	434799	4944122	124.2	98.2	100.4	102.2	26.0	23.8	22.0	-4.0	-1.8
183	457.5	434801	4944121	124.4	98.8	100.7	102.5	25.6	23.7	21.9	-3.7	-1.8
184	460	434802	4944119	124.5	99.6	101.1	102.7	24.9	23.4	21.8	-3.1	-1.6
185	462.5	434804	4944117	124.6	100.5	101.7	103.0	24.1	22.9	21.6	-2.5	-1.3
186	465	434805	4944115	124.8	101.2	102.4	103.4	23.6	22.4	21.4	-2.2	-1.0
187	467.5	434807	4944113	124.9	101.7	102.7	103.7	23.2	22.2	21.2	-2.0	-1.0
188	470	434808	4944111	125.0	102.2	102.8	104.0	22.8	22.2	21.0	-1.8	-1.2
189	472.5	434811	4944111	125.5	103.0	103.1	104.0	22.5	22.4	21.5	-1.0	-0.9
190	475	434813	4944110	125.1	103.8	103.8	104.0	21.3	21.3	21.1	-0.2	-0.2
191	477.5	434816	4944109	125.3	104.6	104.4	104.1	20.7	20.9	21.1	0.5	0.3

[a]Failure depth from 2-layer (Z_2) and 3-layer (Z_3) low velocity zone boundary and fitted plane (Z_{fp}) to the subsurface data

[b]Landslide thickness predicted by the 2-layer, 3-layer and fitted failure plane

Table D3. Comparison between borehole and refraction data for the Vaughn landslide

Geophone Locations					Failure Depth[a]		Landslide Thickness[b]	
Geophone	**Distance (X_{dist})** (m)	***X*** (Easting)	***Y*** (Northing)	***Z*** (m)	Z_2 (m)	Z_3 (m)	Z-Z_2 (m)	Z-Z_3 (m)
1	0	460861	4873505	243.1	233.4	235.8	9.7	7.3
2	5	460865	4873506	242.7	233.4	235.9	9.3	6.8
3	10	460870	4873508	241.3	233.3	235.5	8.0	5.8
4	15	460874	4873510	240.7	233.1	235.6	7.6	5.2
5	20	460879	4873513	240.3	232.9	235.4	7.4	4.9
6	25	460884	4873514	239.1	232.6	235.4	6.5	3.8
7	30	460888	4873516	238.9	232.1	234.9	6.7	3.9
8	35	460892	4873518	238.1	231.4	234.2	6.6	3.8
9	40	460897	4873521	240.5	230.4	233.7	10.1	6.7
10	45	460902	4873522	237.0	229.7	232.9	7.2	4.1
11	50	460906	4873525	236.8	229.7	232.6	7.1	4.2
12	55	460910	4873525	241.5	229.7	232.5	11.8	9.0
13	60	460916	4873528	239.6	229.4	231.7	10.2	7.8
14	65	460919	4873531	238.0	228.4	230.8	9.6	7.2
15	70	460924	4873534	235.7	227.3	230.0	8.4	5.7
16	75	460927	4873536	235.5	226.1	228.8	9.4	6.7
17	80	460933	4873540	237.0	225.0	227.9	12.0	9.1
18	85	460936	4873542	234.3	225.0	226.9	9.3	7.3
19	90	460939	4873545	233.4	224.8	226.7	8.6	6.8
20	95	460946	4873545	233.2	224.5	226.5	8.7	6.6
21	100	460949	4873550	230.8	224.3	226.0	6.5	4.7
22	105	460954	4873553	233.6	224.1	226.0	9.6	7.6
23	110	460958	4873558	229.0	223.9	225.6	5.1	3.4
24	115	460961	4873560	227.5	223.3	224.7	4.2	2.8
25	120	460961	4873566	226.2	222.2	223.8	4.0	2.5
26	125	460966	4873569	228.0	221.7	223.6	6.3	4.4
27	130	460967	4873573	227.6	221.7	223.4	5.9	4.2
28	135	460971	4873575	228.3	221.7	223.2	6.6	5.1
29	140	460975	4873581	228.0	221.1	222.9	6.8	5.1
30	145	460978	4873583	223.4	220.5	222.0	2.9	1.4
31	150	460982	4873585	227.0	218.7	220.4	8.3	6.6
32	155	460986	4873586	227.3	217.4	218.9	9.9	8.5
33	160	460992	4873589	225.0	216.8	217.8	8.2	7.2
34	165	461001	4873590	223.8	216.8	217.2	7.0	6.6
35	170	461002	4873593	223.9	216.4	216.8	7.6	7.1
36	175	461005	4873593	220.2	215.6	217.1	4.6	3.2

Table D3. (continued)

Geophone Locations					Failure Depth[a]		Landslide Thickness[b]	
Geophone	**Distance (X_{dist})** (m)	***X*** (Easting)	***Y*** (Northing)	***Z*** (m)	Z_2 (m)	Z_3 (m)	Z-Z_2 (m)	Z-Z_3 (m)
37	180	461037	4873596	219.2	215.5	216.7	3.8	2.5
38	185	461016	4873595	219.5	215.5	216.4	4.0	3.0
39	190	461020	4873596	218.5	215.3	216.1	3.2	2.4
40	195	461025	4873596	218.4	215.1	215.8	3.3	2.6
41	200	461030	4873597	217.8	214.8	215.9	3.0	2.0
42	205	461035	4873598	217.5	214.3	215.9	3.2	1.5
[c]43	**210**	**461041**	**4873598**	**217.5**	**213.7**	**215.3**	**3.8**	**2.2**
44	215	461045	4873598	217.7	212.9	214.2	4.7	3.4
45	220	461050	4873598	216.4	212.0	213.2	4.4	3.3
46	225	461055	4873599	216.0	211.6	212.6	4.5	3.5
47	230	461060	4873599	216.0	211.4	212.6	4.6	3.4
48	235	461065	4873600	215.4	211.4	212.3	4.0	3.1
49	240	461070	4873600	214.5	211.0	211.8	3.6	2.8
50	245	461075	4873600	213.8	210.4	210.7	3.4	3.0
51	250	461080	4873600	213.2	209.7	209.5	3.5	3.7
52	255	461085	4873599	215.6	208.0	208.2	7.6	7.4
53	260	461090	4873600	215.5	206.8	207.7	8.7	7.8
54	265	461095	4873600	215.4	206.0	207.1	9.4	8.2
55	270	461100	4873600	211.3	205.4	206.6	5.9	4.7
56	275	461104	4873603	210.9	204.6	206.3	6.2	4.6
57	280	461109	4873603	213.1	203.8	205.9	9.3	7.2
58	285	461114	4873605	210.5	202.4	205.0	8.1	5.5
59	290	461118	4873607	210.3	200.6	204.0	9.6	6.3
60	295	461122	4873609	208.8	198.8	202.2	9.9	6.5
61	300	461127	4873611	207.6	197.3	201.4	10.4	6.3
62	305	461132	4873614	207.8	196.3	201.6	11.6	6.2
63	310	461136	4873616	205.9	195.1	201.6	10.8	4.2
64	315	461140	4873618	206.4	194.1	200.6	12.3	5.7
65	320	461144	4873621	204.2	193.2	199.1	11.1	5.1
66	325	461148	4873623	203.3	192.6	197.3	10.7	6.0
67	330	461153	4873625	203.2	191.1	195.4	12.1	7.7
68	335	461157	4873629	200.6	189.6	194.9	11.0	5.7
69	340	461162	4873631	202.2	187.9	195.4	14.3	6.8
70	345	461167	4873632	201.9	186.3	194.4	15.6	7.5
71	350	461172	4873635	202.9	185.2	192.0	17.7	10.9
72	355	461174	4873638	199.8	184.4	189.6	15.4	10.2
73	360	461179	4873640	198.7	183.9	188.0	14.8	10.7

Table D3. (continued)

Geophone Locations					Failure Depth[a]		Landslide Thickness[b]	
Geophone	**Distance (X_{dist})** (m)	***X*** (Easting)	***Y*** (Northing)	***Z*** (m)	Z_2 (m)	Z_3 (m)	Z-Z_2 (m)	Z-Z_3 (m)
74	365	461183	4873643	198.2	183.3	187.5	14.9	10.7
75	370	461187	4873646	197.7	182.5	187.6	15.2	10.1
76	375	461192	4873651	201.7	181.5	187.6	20.1	14.0
77	380	461192	4873653	195.1	181.2	187.5	13.9	7.5
78	385	461196	4873658	196.4	181.2	186.9	15.2	9.4
79	390	461198	4873661	194.8	182.2	187.6	12.6	7.2
80	395	461201	4873667	195.5	183.4	188.2	12.1	7.3
81	400	461203	4873672	195.2	184.6	188.9	10.5	6.3
82	405	461202	4873676	196.9	185.6	189.2	11.3	7.7
83	410	461204	4873682	195.0	185.7	188.7	9.3	6.3
84	415	461206	4873685	192.6	185.5	187.3	7.1	5.3
85	420	461209	4873691	196.3	185.3	186.7	11.0	9.6
86	425	461209	4873693	191.0	185.4	186.7	5.6	4.3
87	430	461215	4873700	195.5	186.1	186.8	9.4	8.7
88	435	461216	4873702	191.6	186.5	185.9	5.1	5.7
89	440	461221	4873704	188.7	186.2	185.4	2.6	3.3
90	445	461225	4873707	189.0	185.8	185.1	3.2	4.0
91	450	461232	4873709	194.9	185.8	184.8	9.1	10.0
92	455	461233	4873712	188.9	185.7	184.8	3.2	4.0
93	460	461237	4873716	187.2	185.1	184.3	2.0	2.8
94	465	461241	4873717	186.7	184.3	183.8	2.4	2.9
95	470	461246	4873719	186.8	183.5	183.2	3.3	3.6
96	475	461251	4873721	185.0	182.7	183.0	2.4	2.0

[a]Failure depth from 2-layer (Z_2) and 3-layer (Z_3) low velocity zone
[b]Landslide thickness predicted by the 2-layer and 3-layer inversion
[c]Nearest geophone to auger and seismometer location

REFERENCES CITED

Chapter I

Dietrich, W. E., D. G. Bellugi, L. S. Sklar, J. D. Stock, A. M. Heimsath, and J. J. Roering (2003), Geomorphic transport laws for predicting landscape form and dynamics, in Predictions in Geomorphology, vol. 135, pp. 103–132, AGU Geophysical Monograph Series.

Hooke, R. (1994), On the efficacy of humans as geomorphic agents, GSA Today, 4(9), 3.

Korup, O., A. L. Densmore, and F. Schlunegger (2010), The role of landslides in mountain range evolution, Geomorphology, 120(1-2), 77–90, doi:10.1016/j.geomorph.2009.09.017.

Lavé, J., and D. W. Burbank (2004), Denudation processes and rates in the Transverse Ranges, southern California: Erosional response of a transitional landscape to external and anthropogenic forcing, J. Geophys. Res. Earth Surf., 109(F1), 1–31, doi:10.1029/2003JF000023.

Montgomery, D. R. (2007), Soil erosion and agricultural sustainability., Proc. Natl. Acad. Sci. U. S. A., 104(33), 13268–72, doi:10.1073/pnas.0611508104.

Roering, J. J., J. W. Kirchner, and W. E. Dietrich (2005), Characterizing structural and lithologic controls on deep-seated landsliding: Implications for topographic relief and landscape evolution in the Oregon Coast Range, USA, Geol. Soc. Am. Bull., 117(5), 654, doi:10.1130/B25567.1.

Whipple, K., and G. Tucker (1999), Dynamics of the stream power river incision model: Implications for height limits of mountain ranges, landscape response timescales, and research needs, J. Geophys. Res. Solid Earth, 104, 661–674.

Chapter II

Avouac, J.-P. (1993), Analysis of scarp profiles: Evaluation of errors in morphologic dating, J. Geophys. Res., 98(B4), 6745, doi:10.1029/92JB01962.

Berryman, K., M. Marden, D. Eden, C. Mazengarb, Y. Ota, and I. Moriya (2000), Tectonic and paleoclimatic significance of Quaternary river terraces of the Waipaoa River, east coast, North Island, New Zealand, New Zeal. J. Geol. Geophys., 43(2), 229–245.

Berryman, K., M. Marden, A. Palmer, K. Wilson, C. Mazengarb, and N. Litchfield (2010), The post-glacial downcutting history in the Waihuka tributary of Waipaoa River, Gisborne district: Implications for tectonics and landscape evolution in the Hikurangi subduction margin, New Zealand, Mar. Geol., 270(1-4), 55–71, doi:10.1016/j.margeo.2009.10.001.

Bilderback, E. L. (2012), Hillslope response to climate-modulated river incision and the role of deep-seated landslides in post-glacial sediment flux: Waipaoa Sedimentary System, New Zealand, PhD Thesis, University of Canterbury. Geological Sciences. http://ir.canterbury.ac.nz/handle/10092/7439

Bilderback, E. L., J. Pettinga, N. J. Litchfield, M. Quigley, M. Marden, J. J. Roering, and A. S. Palmer (2014), Hillslope response to climate-modulated river incision in the Waipaoa Catchment, East Coast North Island, New Zealand, Geol. Soc. Am. Bull.

Black, R. (1980), Upper Cretaceous and Tertiary geology of Mangatu State Forest, Raukumara Peninsula, New Zealand, New Zeal. J. Geol. Geophys., 23(1958), 293–312.

Booth, A. M., J. J. Roering, and A. W. Rempel (2013), Topographic signatures and a general transport law for deep-seated landslides in a landscape evolution model, J. Geophys. Res. Earth Surf., 118(2), 603–624, doi:10.1002/jgrf.20051.

Brown, L. (1995), Holocene shoreline depositional processes at Poverty Bay, a tectonically active area, northeastern North Island, New Zealand, Quat. Int., 26(94), 21–33.

Bull, W. B. (1991), Geomorphic responses to climatic change, Oxford University Press.

Clark, M. K., L. H. Royden, K. X. Whipple, B. C. Burchfiel, X. Zhang, and W. Tang (2006), Use of a regional, relict landscape to measure vertical deformation of the eastern Tibetan Plateau, J. Geophys. Res., 111(F3), 23, doi:10.1029/2005JF000294.

Crosby, B., and K. Whipple (2006), Knickpoint initiation and distribution within fluvial networks: 236 waterfalls in the Waipaoa River, North Island, New Zealand, Geomorphology, 82(1-2), 16–38, doi:10.1016/j.geomorph.2005.08.023.

Crosby, B. T., K. X. Whipple, N. M. Gasparini, and C. W. Wobus (2007), Formation of fluvial hanging valleys: Theory and simulation, J. Geophys. Res., 112(F3), 1–20, doi:10.1029/2006JF000566.

DeMets, C., R. G. Gordon, D. F. Argus, and S. Stein (1994), Effect of recent revisions to the geomagnetic reversal time scale on estimates of current plate motions, Geophys. Res. Lett., 21(20), 2191–2194, doi:10.1029/94GL02118.

Eden, D. N., A. S. Palmer, S. J. Cronin, M. Marden, and K. R. Berryman (2001), Dating the culmination of river aggradation at the end of the last glaciation using distal tephra compositions, eastern North Island, New Zealand, Geomorphology, 38(1-2), 133–151, doi:10.1016/S0169-555X(00)00077-5.

Finnegan, N. J., R. Schumer, and S. Finnegan (2014), A signature of transience in bedrock river incision rates over timescales of 10(4)-10(7) years., Nature, 505(7483), 391–4, doi:10.1038/nature12913.

Foster, G., and L. Carter (1997), Mud sedimentation on the continental shelf at an accretionary margin—Poverty Bay, New Zealand, New Zeal. J. Geol. Geophys., 40(2).

Frankel, K. L., and J. F. Dolan (2007), Characterizing arid region alluvial fan surface roughness with airborne laser swath mapping digital topographic data, J. Geophys. Res., 112(F2), F02025, doi:10.1029/2006JF000644.

Froggatt, P., and D. Lowe (1990), A review of late Quaternary silicic and some other tephra formations from New Zealand: their stratigraphy, nomenclature, distribution, volume, and age, New Zeal. J. Geol. Geophys., 37–41.

Gage, M., and R. D. Black (1979), Slope-stability and geological investigations at Mangatu State Forest, New Zeal. For. Serv. Tech. Pap., 66.

Gallen, S. F., K. W. Wegmann, K. L. Frankel, S. Hughes, R. Q. Lewis, N. Lyons, P. Paris, K. Ross, J. B. Bauer, and A. C. Witt (2011), Hillslope response to knickpoint migration in the Southern Appalachians: implications for the evolution of post-orogenic landscapes, Earth Surf. Process. Landforms, 36(9), 1254–1267, doi:10.1002/esp.2150.

Gasparini, N. M., K. X. Whipple, and R. L. Bras (2007), Predictions of steady state and transient landscape morphology using sediment-flux-dependent river incision models, J. Geophys. Res., 112(F3), 1–20, doi:10.1029/2006JF000567.

Gerber, T. P., L. F. Pratson, S. Kuehl, J. P. Walsh, C. Alexander, and A. Palmer (2010), The influence of sea level and tectonics on Late Pleistocene through Holocene sediment storage along the high-sediment supply Waipaoa continental shelf, Mar. Geol., 270(1-4), 139–159, doi:10.1016/j.margeo.2009.10.002.

Gomez, B., and D. M. Livingston (2012), The river it goes right on: Post-glacial landscape evolution in the upper Waipaoa River basin, eastern North Island, New Zealand, Geomorphology, 159-160, 73–83, doi:10.1016/j.geomorph.2012.03.006.

Gomez, B., L. Carter, N. a. Trustrum, A. S. Palmer, and A. P. Roberts (2004), El Niño–Southern Oscillation signal associated with middle Holocene climate change in intercorrelated terrestrial and marine sediment cores, North Island, New Zealand, Geology, 32(8), 653, doi:10.1130/G20720.1.

Guzzetti, F., A. Mondini, M. Cardinali, F. Fiorucci, M. Santangelo, and K.-T. Chang (2012), Landslide inventory maps: New tools for an old problem, Earth-Science Rev., doi:10.1016/j.earscirev.2012.02.001.

Hicks, D. M., B. Gomez, and N. A. Trustrum (2000), Erosion thresholds and suspended sediment yields, Waipaoa River Basin, New Zealand, Water Resour. Res., 36(4), 1129–1142.

Hovius, N., C. Stark, and P. Allen (1997), Sediment flux from a mountain belt derived by landslide mapping, Geology, 25, 231–234, doi:10.1130/0091-7613(1997)025<0231.

Hurst, M. D., S. M. Mudd, M. Attal, and G. Hilley (2013), Hillslopes record the growth and decay of landscapes., Science (80-.)., 341(6148), 868–871, doi:10.1126/science.1241791.

Jenness, J. (2004), Calculating landscape surface area from digital elevation models, Wildl. Soc. Bull., 32(1986), 829–839.

Kirchner, J., R. Finkel, and C. Riebe (2001), Mountain erosion over 10 yr, 10 ky, and 10 my time scales, Geology, 29, 591–594, doi:10.1130/0091-7613(2001)029<0591.

Korup, O., A. L. Densmore, and F. Schlunegger (2010), The role of landslides in mountain range evolution, Geomorphology, 120(1-2), 77–90, doi:10.1016/j.geomorph.2009.09.017.

Lang, A., J. Moya, J. Corominas, L. Schrott, and R. Dikau (1999), Classic and new dating methods for assessing the temporal occurrence of mass movements, Geomorphology, 30(1-2), 33–52, doi:10.1016/S0169-555X(99)00043-4.

Larsen, I. J., and D. R. Montgomery (2012), Landslide erosion coupled to tectonics and river incision, Nat. Geosci., 5(7), 468–473, doi:10.1038/ngeo1479.

Larsen, I. J., D. R. Montgomery, and H. M. Greenberg (2014), The contribution of mountains to global denudation, Geology, 42(6), 527–530, doi:10.1130/G35136.1.

Lavé, J., and D. W. Burbank (2004), Denudation processes and rates in the Transverse Ranges, southern California: Erosional response of a transitional landscape to external and anthropogenic forcing, J. Geophys. Res. Earth Surf., 109(F1), 1–31, doi:10.1029/2003JF000023.

Leithold, E. L., N. E. Blair, L. B. Childress, B. R. Brulet, M. Marden, A. R. Orpin, S. a. Kuehl, and C. R. Alexander (2013), Signals of watershed change preserved in organic carbon buried on the continental margin seaward of the Waipaoa River, New Zealand, Mar. Geol., 346, 355–365, doi:10.1016/j.margeo.2013.10.007.

Litchfield, N., and K. Berryman (2006), Relations between postglacial fluvial incision rates and uplift rates in the North Island, New Zealand, J. Geophys. Res., 111(F2), F02007, doi:10.1029/2005JF000374.

Litchfield, N. J., and K. R. Berryman (2005), Correlation of fluvial terraces within the Hikurangi Margin, New Zealand: implications for climate and baselevel controls, Geomorphology, 68(3-4), 291–313, doi:10.1016/j.geomorph.2004.12.001.

Lowe, D., M. Blaauw, A. G. Hogg, and R. M. Newnham (2013), Ages of 24 widespread tephras erupted since 30,000 years ago in New Zealand, with re-evaluation of the timing and palaeoclimatic implications of the Lateglacial cool, Quat. Sci. Rev., 74, 170–194, doi:10.1016/j.quascirev.2012.11.022.

Lowe, D. J. (2011), Tephrochronology and its application: A review, Quat. Geochronol., 6(2), 107–153, doi:10.1016/j.quageo.2010.08.003.

Lowe, D. J., P. a. R. Shane, B. V. Alloway, and R. M. Newnham (2008), Fingerprints and age models for widespread New Zealand tephra marker beds erupted since 30,000 years ago: a framework for NZ-INTIMATE, Quat. Sci. Rev., 27(1-2), 95–126, doi:10.1016/j.quascirev.2007.01.013.

Marden, M., G. Arnold, B. Gomez, and D. Rowan (2005), Pre- and post-reforestation gully development in Mangatu Forest, East Coast, North Island, New Zealand, River Res. Appl., 21(7), 757–771.

Marden, M., C. Mazengarb, A. Palmer, K. Berryman, and D. Rowan (2008), Last glacial aggradation and postglacial sediment production from the non-glacial Waipaoa and Waimata catchments, Hikurangi Margin, North Island, New Zealand, Geomorphology, 99(1-4), 404–419, doi:10.1016/j.geomorph.2007.12.003.

Marden, M., H. Betts, a. Palmer, R. Taylor, E. Bilderback, and N. Litchfield (2014), Post-Last Glacial Maximum fluvial incision and sediment generation in the unglaciated Waipaoa catchment, North Island, New Zealand, Geomorphology, 214, 283–306, doi:10.1016/j.geomorph.2014.02.012.

Marsaglia, K. M., A. M. DeVaughn, D. E. James, and M. Marden (2010), Provenance of fluvial terrace sediments within the Waipaoa sedimentary system and their importance to New Zealand source-to-sink studies, Mar. Geol., 270(1-4), 84–93, doi:10.1016/j.margeo.2009.10.017.

Mazengarb, C., and I. Speden (2000), Geology of the Raukumara Area, Institute of Geological & Nuclear Sciences, Lower Hutt.

McGlone, M. (2001), A late Quaternary pollen record from marine core P69, southeastern North Island, New Zealand, New Zeal. J. Geol. Geophys., 44, 69–77.

McKean, J., and J. Roering (2004), Objective landslide detection and surface morphology mapping using high-resolution airborne laser altimetry, Geomorphology, 57(3), 331–351.

Merritts, D., and K. Vincent (1989), Geomorphic response of coastal streams to low, intermediate, and high rates of uplift, Medocino triple junction region, northern California, Geol. Soc. Am. Bull., 101(11), 1373–1388, doi:10.1130/0016-7606(1989)101<1373.

Milliman, J. D., and J. P. M. Syvitski (1992), Geomorphic/tectonic control of sediment discharge to the ocean: the importance of small mountainous rivers, J. Geol., 100(5), 525–544.

Montgomery, D. R., and M. T. Brandon (2002), Topographic controls on erosion rates in tectonically active mountain ranges, Earth Planet. Sci. Lett., 201(3-4), 481–489, doi:10.1016/S0012-821X(02)00725-2.

Orpin, A. R., C. Alexander, L. Carter, S. Kuehl, and J. P. Walsh (2006), Temporal and spatial complexity in post-glacial sedimentation on the tectonically active, Poverty Bay continental margin of New Zealand, Cont. Shelf Res., 26(17-18), 2205–2224, doi:10.1016/j.csr.2006.07.029.

Ouimet, W. B., K. X. Whipple, L. H. Royden, Z. Sun, and Z. Chen (2007), The influence of large landslides on river incision in a transient landscape: Eastern margin of the Tibetan Plateau (Sichuan, China), Geol. Soc. Am. Bull., 119(11-12), 1462–1476, doi:10.1130/B26136.1.

Page, M., and B. Lukovic (2011), An inventory of deep-seated landslides in the Waipaoa and Waimata catchments, Lower Hutt.

Pazzaglia, F., and M. Brandon (2001), A fluvial record of long-term steady-state uplift and erosion across the Cascadia forearc high, western Washington State, Am. J. Sci., 301, 385–431.

Phillips, J. D., M. Marden, and B. Gomez (2007), Residence time of alluvium in an aggrading fluvial system, Earth Surf. Process. Landforms, 32(2), 307–316, doi:10.1002/esp.1385.

Preston, N., and M. Crozier (1999), Resistance to shallow landslide failure through root-derived cohesion in east coast hill country soils, North Island, New Zealand, Earth Surf. Process. Landforms, 675, 665–675.

Reid, L. M., and M. J. Page (2002), Magnitude and frequency of landsliding in a large New Zealand catchment, Geomorphology, 49, 71–88.

Sadler, P. M., and D. J. Jerolmack (2014), Scaling laws for aggradation, denudation and progradation rates: the case for time-scale invariance at sediment sources and sinks, Geol. Soc. London, Spec. Publ., 404, doi:10.1144/SP404.7.

Schmidt, K. M., and D. R. Montgomery (1995), Limits to Relief, Science (80-.)., 270(5236), 617–620, doi:10.1126/science.270.5236.617.

Schumm, S. (1993), River response to baselevel change: implications for sequence stratigraphy, J. Geol., 101(2), 279–294.

Shane, P., V. Smith, D. Lowe, and I. Nairn (2003), Re-identification of c. 15 700 cal yr BP tephra bed at Kaipo Bog, eastern North Island: Implications for dispersal of Rotorua and Puketarata tephra beds, New Zeal. J. Geol. Geophys., 46, 591–596.

Smith, V., P. Shane, and I. Nairn (2005), Trends in rhyolite geochemistry, mineralogy, and magma storage during the last 50 kyr at Okataina and Taupo volcanic centres, Taupo Volcanic Zone, New Zealand, J. Volcanol. Geotherm. Res., 148, 372–406, doi:10.1016/j.volgeores.2005.05.005.

Wallace, L. M. (2004), Subduction zone coupling and tectonic block rotations in the North Island, New Zealand, J. Geophys. Res., 109(B12), B12406, doi:10.1029/2004JB003241.

Warrick, J. a., J. D. Milliman, D. E. Walling, R. J. Wasson, J. P. M. Syvitski, and R. E. Aalto (2013), Earth is (mostly) flat: Apportionment of the flux of continental sediment over millennial time scales: COMMENT, Geology, 42(1), e316–e316, doi:10.1130/G34846C.1.

Wegmann, K. W., and F. J. Pazzaglia (2002), Holocene strath terraces, climate change, and active tectonics: The Clearwater River basin, Olympic Peninsula, Washington State, Geol. Soc. Am. Bull., 114(6), 731–744, doi:10.1130/0016-7606(2002)114.

Whipple, K., and G. Tucker (1999), Dynamics of the stream-power river incision model: Implications for height limits of mountain ranges, landscape response timescales, and research needs, J. Geophys. Res. Solid Earth, 104, 661–674.

Whipple, K. X., and G. E. Tucker (2002), Implications of sediment-flux-dependent river incision models for landscape evolution, J. Geophys. Res., 107(B2), 2039, doi:10.1029/2000JB000044.

Whipple, K. X., E. Kirby, and S. H. Brocklehurst (1999), Geomorphic limits to climate-induced increases in topographic relief, Nature, 401, 39–43.

Williams, P., H. Nei, and J. Zhao (2010), Age frequency distribution and revised stable isotope curves for New Zealand speleothems: palaeoclimatic implications, Int. J. Speleol., 39, 99–112.

Williams, P. W., D. N. T. King, J.-X. Zhao, and K. D. Collerson (2005), Late Pleistocene to Holocene composite speleothem 18O and 13C chronologies from South Island, New Zealand—did a global Younger Dryas really exist?, Earth Planet. Sci. Lett., 230(3-4), 301–317, doi:10.1016/j.epsl.2004.10.024.

Wilmshurst, J. M., D. N. Eden, and P. C. Froggatt (1999), Late Holocene forest disturbance in Gisborne, New Zealand: a comparison of terrestrial and marine pollen records, New Zeal. J. Bot., 37(3), 523–540.

Wilmshurst, J. M., T. L. Hunt, C. P. Lipo, and A. J. Anderson (2011), High-precision radiocarbon dating shows recent and rapid initial human colonization of East Polynesia., Proc. Natl. Acad. Sci. U. S. A., 108(5), 1815–20, doi:10.1073/pnas.1015876108.

Wright, I., M. McGlone, C. Nelson, and B. Pillans (1995), An integrated latest Quaternary (stage 3 to present) paleoclimatic and paleoceanographic record from offshore northern New Zealand, Quat. Res., 44, 283–293.

Chapter III

Allsop, F. (1973), The Story of the Mangatu, New Zeal. For. Serv. Inf. Ser., 62, 100.

Anderson, I. (2010), Pioneering in Kanakanaia-Te Karaka, Ian Anderson, Gisborne.

Benda, L., and T. Dunne (1997), Stochastic forcing of sediment routing and storage in channel networks, Water Resour. Res., 33(12), 2865, doi:10.1029/97WR02387.

Berryman, K., M. Marden, D. Eden, C. Mazengarb, Y. Ota, and I. Moriya (2000), Tectonic and paleoclimatic significance of Quaternary river terraces of the Waipaoa River, east coast, North Island, New Zealand, New Zeal. J. Geol. Geophys., 43(2), 229–245.

Beschta, R. L. (1978), Long-term patterns of sediment production following road construction and logging in the Oregon Coast Range, Water Resour. Res., 14(6), 1011, doi:10.1029/WR014i006p01011.

Beven, K., and P. F. Germann (1982), Macropores and water flows in soils, Wat. Resour. Res., 18(5), 1311–1325, doi:10.1029/WR018i005p01311.

Bilderback, E. L., J. R. Pettinga, N. J. Litchfield, M. Quigley, M. Marden, J. J. Roering, and A. S. Palmer (2015), Hillslope response to climate-modulated river incision in the Waipaoa catchment, East Coast North Island, New Zealand, Geol. Soc. Am. Bull., 127(1-2), 131–148, doi:10.1130/B31015.1.

Campbell, D. A. (1946), Down to the Sea in Slips, Soil Conservation and Rivers Control Council, Wellington.

Cerovski-Darriau, C., J. J. Roering, M. Marden, A. S. Palmer, and E. L. Bilderback (2014), Quantifying temporal variations in landslide-driven sediment production by reconstructing paleolandscapes using tephrochronology and lidar: Waipaoa River, New Zealand, Geochemistry, Geophys. Geosystems, 15(11), 4117–4136, doi:10.1002/2014GC005467.

Crozier, M. J., and B. J. Pillans (1991), Geomorphic events and landform response in south-eastern Taranaki, New Zealand, CATENA, 18(5), 471–487, doi:10.1016/0341-8162(91)90050-8.

DeRose, R., and B. Gomez (1998), Gully erosion in Mangatu Forest, New Zealand, estimated from digital elevation models, Earth Surf. …, 1053, 1045–1053.

Dietrich, W. E., D. G. Bellugi, L. S. Sklar, J. D. Stock, A. M. Heimsath, and J. J. Roering (2003), Geomorphic transport laws for predicting landscape form and dynamics, in Predictions in Geomorphology, vol. 135, pp. 103–132, AGU Geophysical Monograph Series.

Fuller, I. C., M. G. Macklin, and J. M. Richardson (2015), The Geography of the Anthropocene in New Zealand: Differential River Catchment Response to Human Impact, Geogr. Res., 53(3), 255–269, doi:10.1111/1745-5871.12121.

Gage, M., and R. D. Black (1979), Slope-stability and geological investigations at Mangatu State Forest, New Zeal. For. Serv. Tech. Pap., 66.

Glade, T. (2003), Landslide occurrence as a response to land use change: a review of evidence from New Zealand, CATENA, 51(3-4), 297–314, doi:10.1016/S0341-8162(02)00170-4.

Gomez, B., K. Banbury, M. Marden, N. A. Trustrum, D. H. Peacock, and P. J. Hoskin (2003), Gully erosion and sediment production: Te Weraroa Stream, New Zealand, Water Resour. Res., 39(7), n/a–n/a, doi:10.1029/2002WR001342.

Gomez, B., L. Carter, N. A. Trustrum, A. S. Palmer, and A. P. Roberts (2004), El Niño–Southern Oscillation signal associated with middle Holocene climate change in intercorrelated terrestrial and marine sediment cores, North Island, New Zealand, Geology, 32(8), 653, doi:10.1130/G20720.1.

Gray, D. H., and R. B. Sotir (1996), Biotechnical and Soil Bioengineering Slope Stabilization: A Practical Guide for Erosion Control, John Wiley & Sons, New York.

Greenway, D. R. (1987), Vegetation and Slope Stability, in Slope Stability: Geotechnical Engineering and Geomorphology, edited by M. F. Anderson and K. S. Richards, pp. 187–230, John Wiley & Sons, New York.

Hamza, M. A., and W. K. Anderson (2005), Soil compaction in cropping systems, Soil Tillage Res., 82(2), 121–145, doi:10.1016/j.still.2004.08.009.

Handwerger, A. L., J. J. Roering, and D. A. Schmidt (2013), Controls on the seasonal deformation of slow-moving landslides, Earth Planet. Sci. Lett., 377-378, 239–247, doi:10.1016/j.epsl.2013.06.047.

Henderson, J., and M. Ongley (1920), The Geology of the Gisborne and Whatatutu Subdivisions, Raukumara Division, New Zeal. Geol. Surv. Bull., 21, 88.

Hewawasam, T., F. von Blanckenburg, M. Schaller, and P. Kubik (2003), Increase of human over natural erosion rates in tropical highlands constrained by cosmogenic nuclides, Geology, 31(7), 597–600, doi:10.1130/0091-7613(2003)031<0597:IOHONE>2.0.CO;2.

Hicks, D., U. Shankar, A. McKerchar, L. Basher, I. Lynn, M. Page, and M. Jessen (2011), Suspended sediment yields from New Zealand rivers, J. Hydrol., 50(1), 81–142.

Hicks, D. M., B. Gomez, and N. A. Trustrum (2000), Erosion thresholds and suspended sediment yields, Waipaoa River Basin, New Zealand, Water Resour. Res., 36(4), 1129–1142.

Hooke, R. (1994), On the efficacy of humans as geomorphic agents, GSA Today, 4(9), 3.

Hooke, R. L. (2000), On the history of human as geomorphic agent, Geology, 28(9), 843–846, doi:10.1130/0091-7613(2000)28<843.

Horton, R. E. (1945), Erosional development of streams and their drainage basins; hydrophysical approach to quantitative morphology, Geol. Soc. Am. Bull., 56(3), 275–370, doi:10.1130/0016-7606(1945)56[275:EDOSAT]2.0.CO;2.

Howard, A. D. (1994), A detachment-limited model of drainage basin evolution, Water Resour. Res., 30(7), 2261–2285, doi:10.1029/94WR00757.

Howard, G. (1976), Erosion at Mangatu, Government Print, Wellington.

Hurst, M. D., S. M. Mudd, R. Walcott, M. Attal, and K. Yoo (2012), Using hilltop curvature to derive the spatial distribution of erosion rates, J. Geophys. Res., 117(F2), doi:10.1029/2011JF002057.

Istanbulluoglu, E., and R. L. Bras (2006), On the dynamics of soil moisture, vegetation, and erosion: Implications of climate variability and change, Water Resour. Res., 42(6), W06418, doi:10.1029/2005WR004113.

Iverson, R. M., and J. J. Major (1987), Rainfall , ground-water flow , and seasonal movement at Minor Creek landslide , northwestern California: Physical interpretation of empirical relations, Geol. Soc. Am. Bull., 99(4), 579–594, doi:10.1130/0016-7606(1987)99.

Johnston, D. M., B. F. Houghton, V. E. Neall, K. R. Ronan, and D. Paton (2000), Impacts of the 1945 and 1995-1996 Ruapehu eruptions, New Zealand: An example of increasing societal vulnerability, Geol. Soc. Am. Bull., 112(5), 720–726, doi:10.1130/0016-7606(2000)112<720:IOTARE>2.0.CO;2.

Kelliher, F. M., M. Marden, A. J. Watson, and I. M. Arulchelvam (1995), Estimating the risk of landsliding using historical extreme river flood data, J. Hydrol. (New Zealand), 33(2), 123–129.

Kelsey, H. M. (1978), Earthflows in Franciscan melange, Van Duzen River basin, California, Geology, 6(6), 361–364, doi:10.1130/0091-7613(1978)6<361:EIFMVD>2.0.CO;2.

Kettner, A. J., B. Gomez, and J. P. M. Syvitski (2007), Modeling suspended sediment discharge from the Waipaoa River system, New Zealand: The last 3000 years, Water Resour. Res., 43(7), 1–15, doi:10.1029/2006WR005570.

Litchfield, N., and K. Berryman (2006), Relations between postglacial fluvial incision rates and uplift rates in the North Island, New Zealand, J. Geophys. Res., 111(F2), F02007, doi:10.1029/2005JF000374.

Mackey, B. H., J. J. Roering, and J. a. McKean (2009), Long-term kinematics and sediment flux of an active earthflow, Eel River, California, Geology, 37(9), 803–806, doi:10.1130/G30136A.1.

Marden, M. (2012), Effectiveness of reforestation in erosion mitigation and implications for future sediment yields, East Coast catchments, New Zealand: A review, N. Z. Geog., 68(1), 24–35, doi:10.1111/j.1745-7939.2012.01218.x.

Marden, M., G. Arnold, B. Gomez, and D. Rowan (2005), Pre- and post-reforestation gully development in Mangatu Forest, East Coast, North Island, New Zealand, River Res. Appl., 21(7), 757–771.

Marden, M., H. Betts, and G. Arnold (2008), Gully erosion and sediment load: Waipaoa, Waiapu and Uawa rivers, eastern North Island, New Zealand, IAHS-AISH Publ. Proc. Christchurch Symp., 325, 339–350.

Marden, M., A. Herzig, and L. Basher (2014), Erosion process contribution to sediment yield before and after the establishment of exotic forest: Waipaoa catchment, New Zealand, Geomorphology, 226, 162–174, doi:10.1016/j.geomorph.2014.08.007.

Massa, C., V. Bichet, É. Gauthier, B. B. Perren, O. Mathieu, C. Petit, F. Monna, J. Giraudeau, R. Losno, and H. Richard (2012), A 2500 year record of natural and anthropogenic soil erosion in South Greenland, Quat. Sci. Rev., 32, 119–130, doi:10.1016/j.quascirev.2011.11.014.

Mazengarb, C., and I. Speden (2000), Geology of the Raukumara Area, Institute of Geological & Nuclear Sciences, Lower Hutt.

Molnar, P., and P. England (1990), Late Cenozoic uplift of mountain ranges and global climate change: chicken or egg?, Nature, 346, 29–34.

Montgomery, D. R. (2007), Soil erosion and agricultural sustainability., Proc. Natl. Acad. Sci. U. S. A., 104(33), 13268–72, doi:10.1073/pnas.0611508104.

Montgomery, D. R., and M. T. Brandon (2002), Topographic controls on erosion rates in tectonically active mountain ranges, Earth Planet. Sci. Lett., 201(3-4), 481–489, doi:10.1016/S0012-821X(02)00725-2.

Page, M., and B. Lukovic (2011), An inventory of deep-seated landslides in the Waipaoa and Waimata catchments, Lower Hutt.

Pearce, A. J., C. . O'Loughlin, R. J. Jackson, and X. B. Zhang (1987), Reforestion: on-site effects on hydrology and erosion, eastern Raukumara Range, New Zealand, IAHS-AISH Publ. Proc. hte Vancouver Symp., 167, 489–497.

Pelletier, J. D. et al. (2015), Forecasting the response of Earth's surface to future climatic and land use changes: A review of methods and research needs, Earth's Futur., 3(7), 220–251, doi:10.1002/2014EF000290.

Preston, N., and M. Crozier (1999), Resistance to shallow landslide failure through root derived cohesion in east coast hill country soils, North Island, New Zealand, Earth Surf. Process. Landforms, 675, 665–675.

Reid, L. M., and M. J. Page (2002), Magnitude and frequency of landsliding in a large New Zealand catchment, Geomorphology, 49, 71–88.

Reusser, L., P. Bierman, and D. Rood (2015), Quantifying human impacts on rates of erosion and sediment transport at a landscape scale, Geology, 43(2), 171–174, doi:10.1130/G36272.1.

Roering, J. J., J. W. Kirchner, and W. E. Dietrich (2001), Hillslope evolution by nonlinear, slope-dependent transport: Steady-state morphology and equilibrium adjustment timescales, J. Geophys. Res., 106(B8), 16499–16513.

Roering, J. J., K. M. Schmidt, J. D. Stock, W. E. Dietrich, and D. R. Montgomery (2003), Shallow landsliding, root reinforcement, and the spatial distribution of trees in the Oregon Coast Range, Can. Geotech. J., 40, 237–253, doi:10.1139/t02-113.

Schlesinger, W. H., and J. A. Andrews (2000), Soil respiration and the global carbon cycle, Biogeochemistry, (1977), 7–20.

Schmidt, K. M., J. J. Roering, J. D. Stock, W. E. Dietrich, D. R. Montgomery, and T. Schaub (2001), The variability of root cohesion as an influence on shallow landslide susceptibility in the Oregon Coast Range, Can. Geotech. J., 38(5), 995–1024, doi:10.1139/cgj-38-5-995.

Shakesby, R. A., and S. H. Doerr (2006), Wildfire as a hydrological and geomorphological agent, Earth-Science Rev., 74(3-4), 269–307, doi:10.1016/j.earscirev.2005.10.006.

Sidle, R. C. (1991), A conceptual model of changes in root cohesion in response to vegetation management, J. Environ. Qual., 20(1), 43–52.

Walter, R. C., and D. J. Merritts (2008), Natural streams and the legacy of water-powered mills., Science, 319(5861), 299–304, doi:10.1126/science.1151716.

Whipple, K. X. (2009), The influence of climate on the tectonic evolution of mountain belts, Nat. Geosci., 2(10), 730–730, doi:10.1038/ngeo638.

Wilkinson, B. H., and B. J. McElroy (2007), The impact of humans on continental erosion and sedimentation, Bull. Geol. Soc. Am., 119(1-2), 140–156, doi:10.1130/B25899.1.

Willatt, S. T., and D. M. Pullar (1985), Changes in soil physical properties under grazed pastures, Aust. J. Soil Res., 22, 343–348.

Wilmshurst, J. M., D. N. Eden, and P. C. Froggatt (1999), Late Holocene forest disturbance in Gisborne, New Zealand: a comparison of terrestrial and marine pollen records, New Zeal. J. Bot., 37(3), 523–540.

Zhang, L., W. R. Dawes, and G. R. Walker (2001), Response of mean annual evapotranspiration to vegetation changes at catchment scale, Water Resour. Res., 37(3), 701–708, doi:10.1029/2000WR900325.

Zhang, X., C. Phillips, and M. Marden (1993), A comparison of earthflow movement mechanisms on forested and grassed slopes, Raukumara Peninsula, North Island, New Zealand, Geomorphology, 6(2), 175–187, doi:10.1016/0169-555X(93)90045-4.

Chapter IV

Allstadt, K., J. E. Vidale, and a. D. Frankel (2013), A Scenario Study of Seismically Induced Landsliding in Seattle Using Broadband Synthetic Seismograms, Bull. Seismol. Soc. Am., 103(6), 2971–2992, doi:10.1785/0120130051.

Baldwin, E. (1958), Landslide lakes in the Coast Range of Oregon: Geological Newsletter, Geol. Soc. Oregon Ctry.

Bard, P.-Y. (1998), Microtremor measurements: a tool for site effect estimation?, in Proceeding of the Second International Symposium on the Effects of Surface Geology on Seismic Motion, pp. 1251–1279, Yokohama, Japan.

Benda, L., and T. Dunne (1997), Stochastic forcing of sediment routing and storage in channel networks, Water Resour. Res., 33(12), 2865, doi:10.1029/97WR02387.

Booth, A. M., J. J. Roering, and A. W. Rempel (2013), Topographic signatures and a general transport law for deep-seated landslides in a landscape evolution model, J. Geophys. Res. Earth Surf., 118(2), 603–624, doi:10.1002/jgrf.20051.

Caris, J. P. T., and T. W. J. Van Asch (1991), Geophysical, geotechnical and hydrological investigations of a small landslide in the French Alps, Eng. Geol., 31(3-4), 249–276, doi:10.1016/0013-7952(91)90011-9.

Cerovski-Darriau, C., M. Bodmer, J. J. Roering, and D. R. Toomey (2014), Influence of Seismic Site Response on Landslide Reactivation During the Next Cascadia Earthquake, GSA Annu. Meet. Progr. with Abstr., 46(6), 465.

St. Clair, J., S. Moon, W. S. Holbrook, J. T. Perron, C. S. Riebe, S. J. Martel, B. Carr, C. Harman, and K. Singha (2015), Geophysical imaging reveals topographic stress control of bedrock weathering, Science (80-.)., 350(6260), 534–539, doi:10.1126/science.aab2210.

Dietrich, W. E., D. G. Bellugi, L. S. Sklar, J. D. Stock, A. M. Heimsath, and J. J. Roering (2003), Geomorphic transport laws for predicting landscape form and dynamics, in Predictions in Geomorphology, vol. 135, pp. 103–132, AGU Geophysical Monograph Series.

Field, N., L. Jones, T. Jordan, M. Benthien, and L. Wald (2001), Earthquake Shaking — Finding the " Hotspots ," USGS Factsheet, 001(1).

Goldfinger, C., C. H. Nelson, and J. E. Johnson (2003), Holocene Earthquake Records From the Cascadia Subduction Zone and Northern San Andreas Fault Based on Precise Dating of Offshore Turbidites, Annu. Rev. Earth Planet. Sci., 31(1), 555–577, doi:10.1146/annurev.earth.31.100901.141246.

Hammond, C. M., D. Meier, and D. Beckstand (2009), Paleo-landslides in the Tyee Formation and highway construction, central Oregon Coast Range, in Volcanoes to Vineyards: Geologic Field Trips Through the Dynamic Landscape of the Pacific Northwest, edited by J. E. O'Connor, R. J. Dorsey, and I. Madin, pp. 481–494, Geological Society of America Field Guides.

Harp, E., and R. Jibson (1996), Landslides triggered by the 1994 Northridge, California, earthquake, Bull. Seismol. Soc. Am., 86(1B), 319–322.

Haugerud, R. A. (2014), Preliminary interpretation of pre-2014 landslide deposits in the vicinity of Oso, Washington, Reston, VA.

Heller, P. L., and W. R. Dickinson (1985), Submarine ramp facies model for delta-fed, sand-rich turbidite systems, Am. Assoc. Pet. Geol. Bull., 69(6), 960–976.

Huang, R., and X. Fan (2013), The landslide story, Nat. Geosci., 6(5), 325–326, doi:10.1038/ngeo1806.

Jongmans, D., and S. Garambois (2007), Geophysical investigation of landslides: a review, Bull. la Société géologique Fr., 178(2), 101–112.

Kargel, J. S. et al. (2015), Geomorphic and geologic controls of geohazards induced by Nepals 2015 Gorkha earthquake, Science (80-.)., (June), 1–18, doi:10.1126/science.aac8353.

Kearey, P., M. Brooks, and I. Hill (2002), An Introduction to Geophysical Exploration, 3rd ed., Wiley-Blackwell.

Korup, O. (2006), Effects of large deep-seated landslides on hillslope morphology, western Southern Alps, New Zealand, J. Geophys. Res., 111(F1), 1–18, doi:10.1029/2004JF000242.

Lane, J. (1987), Relations between geology and mass movement features in a part of the East Fork Coquille River Watershed, South. Coast Range, Oregon [MS thesis] Corvallis,.

Larsen, I. J., D. R. Montgomery, and O. Korup (2010), Landslide erosion controlled by hillslope material, Nat. Geosci., 3(4), 247–251, doi:10.1038/ngeo776.

Mathabane, N., C. Cerovski-Darriau, K. E. Sweeney, and J. J. Roering (2013), Assessing the chronology of bedrock landslides in the Oregon Coastal Range using visible near-infrared spectroscopy, AGU Fall Meet., EP53A(761).

Morey, A. E., C. Goldfinger, C. E. Briles, D. G. Gavin, D. Colombaroli, J. E. Kusler, and L. Washington (2011), Potential Lacustrine Records of Cascadia Great Earthquakes, AGU Fall Meet., T51B(2334).

Nakamura, Y. (1989), A method for dynamic characteristics estimation of subsurface using microtremor on the ground surface, Railw. Tech. Res. Institute, Q. Reports, 30(1), 25–33.

Olsen, M. J., S. A. Ashford, R. Mahlingam, M. Sharifi-Mood, M. O'Banion, and D. T. Gillins (2015), Impacts Of Potential Seismic Landslides On Lifeline Cooridors, Salem, Oregon.

Petersen, M. D., C. H. Cramer, and A. D. Frankel (2002), Simulations of Seismic Hazard for the Pacific Northwest of the United States from Earthquakes Associated with the Cascadia Subduction Zone, Pure Appl. Geophys., 159(9), 2147–2168, doi:10.1007/s00024-002-8728-5.

Reneau, S., and W. Dietrich (1991), Erosion rates in the southern Oregon Coast Range: Evidence for an equilibrium between hillslope erosion and sediment yield, Earth Surf. Process. …, 16, 307–322.

Roering, J. J., J. W. Kirchner, and W. E. Dietrich (2001), Hillslope evolution by nonlinear, slope-dependent transport: Steady-state morphology and equilibrium adjustment timescales, J. Geophys. Res., 106(B8), 16499–16513.

Roering, J. J., J. W. Kirchner, and W. E. Dietrich (2005), Characterizing structural and lithologic controls on deep-seated landsliding: Implications for topographic relief and landscape evolution in the Oregon Coast Range, USA, Geol. Soc. Am. Bull., 117(5), 654, doi:10.1130/B25567.1.

Rumpf, M., U. Boniger, and J. Tronicke (2012), Refraction seismics to investigate a creeping hillslope in the Austrian Alps, Eng. Geol., 151, 37–46.

Schrott, L., and O. Sass (2008), Application of field geophysics in geomorphology: Advances and limitations exemplified by case studies, Geomorphology, 93(1-2), 55–73, doi:10.1016/j.geomorph.2006.12.024.

Schulz, W. H., S. L. Galloway, and J. D. Higgins (2012), Evidence for earthquake triggering of large landslides in coastal Oregon, USA, Geomorphology, 141-142, 88–98, doi:10.1016/j.geomorph.2011.12.026.

Snavely, P. D., H. C. Wagner, and N. S. MacLeod (1964), Rhythmic-bedded eugeosynclinal deposits of the Tyee formation, Oregon Coast Range, Kansas Geol. Surv. Bull., 169, 461–480.

Snavely, P. D., N. S. MacLeod, H. C. Wagner, and W. W. Rau (1976), Geologic Map of the Yaquina and Toledo Quadrangles, Lincoln County, Oregon, Map I-867., U.S. Geological Survey, Reston, VA.

Stock, J., and W. E. Dietrich (2003), Valley incision by debris flows: Evidence of a topographic signature, Water Resour. Res., 39(4), doi:10.1029/2001WR001057.

Sweeney, K. E., J. J. Roering, P. Almond, and T. Reckling (2012), How steady are steady-state landscapes? Using visible--near-infrared soil spectroscopy to quantify erosional variability., Geology, 40(9), 807–810, doi:10.1130/G33167.1.

Wartman, J., L. Dunham, B. Tiwari, and D. Pradel (2013), Landslides in Eastern Honshu Induced by the 2011 Tohoku Earthquake, Bull. Seismol. Soc. Am., 103(2B), 1503–1521, doi:10.1785/0120120128.

West, N., E. Kirby, A. Nyblade, S. Brantley, and B. Clarke (2015), Microclimate controls on weathering: Insights into deep critical zone evolution from seismic refraction surveys in the Susquehanna Shale Hills Critical Zone Observatory, AGU Fall Meet., EP41C(941).

Witter, R. C., H. M. Kelsey, and E. Hemphill-Haley (2003), Great Cascadia earthquakes and tsunamis of the past 6700 years, Coquille River estuary, southern coastal Oregon, Geol. Soc. Am. Bull., 115(10), 1289–1306, doi:10.1130/B25189.1.